ARMY RESEARCH LABORATORY

# Response of the Wayne State Thorax Model With Fabric Vest to a 9-mm Bullet

by Martin N. Raftenberg

ARL-TR-2897 January 2003

## NOTICES

### Disclaimers

The findings in this report are not to be construed as an official Department of the Army position unless so designated by other authorized documents.

Citation of manufacturer's or trade names does not constitute an official endorsement or approval of the use thereof.

Destroy this report when it is no longer needed. Do not return it to the originator.

**Army Research Laboratory**
Aberdeen Proving Ground, MD 21005-5066

ARL-TR-2897 January 2003

# Response of the Wayne State Thorax Model With Fabric Vest to a 9-mm Bullet

Martin N. Raftenberg
Weapons and Materials Research Directorate, ARL

# Abstract

The 1999 version of the Wayne State Thorax Model, WSTM99, was applied to the finite element (FE) simulation of a 9-mm Remington bullet striking a multi-ply Kevlar (DuPont) vest worn by a human thorax. The bullet impact speed was 425.5 m/s, and the hit location was the vest material covering the center of the sternum. FE models for the vest and bullet were developed. The computations were performed with the LS-DYNA FE code. Computational results for axial (along the path of the bullet) acceleration were compared with accelerometer measurements from three tests performed at the Armed Forces Institute of Pathology on human thoracic tissue. At the posterior sternum, the computed peak axial acceleration was 5.6 times larger than the measured value in the direction of the bullet's lateral path and 11% smaller than the measured value in the opposite (recoil) direction. At the ligamentum arteriosum, the computed peak axial acceleration exceeded the measured value by factors of 7.9 and 18.1 in the directions along and opposite to the bullet's initial path, respectively. Possible explanations for the discrepancies are offered in terms of features of WSTM99 and of the gauges used in the tests.

## Acknowledgments

The author thanks CAPT Marlene De Maio, MC USNR, of the Armed Forces Institute of Pathology (AFIP); CDR Steven A. Parks, USN, of AFIP; James F. Mackiewicz of the U.S. Army Natick Research, Development, and Engineering Center; and Walter C. Blethen of the U.S. Army Aberdeen Test Center for generously providing thoracic-tissue test data prior to their published release and for responding to his many questions. Professor King H. Yang of the Bioengineering Research Center at Wayne State University and Dr. Kevin H.-C. Wang of General Motors Corporation answered numerous questions regarding their thorax model. Professor Yang also provided a helpful technical review of this document, as did Dr. David Hopkins of the U.S. Army Research Laboratory Weapons and Materials Research Directorate (ARL-WMRD). Thomas Moynihan of D.S.I. Corporation and Thomas J. Mulkern of ARL-WMRD provided useful information on terminal ballistics of fabric armor. H. Halverson of Olin Corporation supplied the drawing of the 9-mm bullet.

INTENTIONALLY LEFT BLANK.

# Contents

## List of Figures

## List of Tables

# 1. Introduction

A finite-element (FE)-based methodology offers the promise for fundamental improvements in body armor design over those produced by the current laboratory testing procedure. FE simulations are generally less costly in time and money and therefore allow for more design iterations. Furthermore, output from an FE simulation includes quantities that would be practically impossible to measure. This is particularly true in problems involving impact to the human body.

The automotive industry has made progress in this area of simulating impact to the body. The Wayne State Thorax Model was originally developed by Kevin H.-C. Wang (then a graduate student) and King H. Yang (a professor) for lateral impact simulations (Wang 1995) (Figure 1). The Wayne State Thorax Model is a three-dimensional (3-D), structural FE model of the thorax of a 50th percentile male seated in the driving position. It consists of an FE mesh and associated material properties. The model was developed to run on the LS-DYNA FE code (Livermore Software Technology Corp. 1999).

The U.S. Army Research Laboratory (ARL) acquired a license to access WSTM99, the 1999 version of the Wayne State Thorax Model, with the intention of using it for body armor analysis. The 1999 version included a single significant revision to the model used in Wang (1995), namely, the 1999 version utilized throughout the model the then-new "automatic single surface" contact algorithm (Livermore Software Technology Corp. 1999). In acquiring access to WSTM99, our plan was to add FE models for various body armor designs and to replace the pendulum in Figure 1 with FE models for various bullet and fragment threats. The immediate output from the LS-DYNA code consists of stresses and displacements throughout the thorax (Figure 2). The usefulness of these stress and displacement results for design purposes would be greatly enhanced if they could be mapped into quantitative injury predictions. This field of mapping is in its infancy.

As a first application of WSTM99 to body armor, three tests recently performed at the Armed Forces Institute of Pathology (AFIP) on human thoracic tissue (Mackiewicz et al., to be published) were simulated. The tests were a joint effort by the U.S. Army Natick Soldier Center, AFIP, and the U.S. Army Aberdeen Test Center (ATC). In each of these tests, the same multi-ply Kevlar (DuPont) vest was placed on human thoracic tissue, and a 9-mm Remington bullet was fired at the center of the sternum. The impact speed was 425–448 m/s. Accelerometers were surgically implanted at four locations: the posterior sternum, the carina of

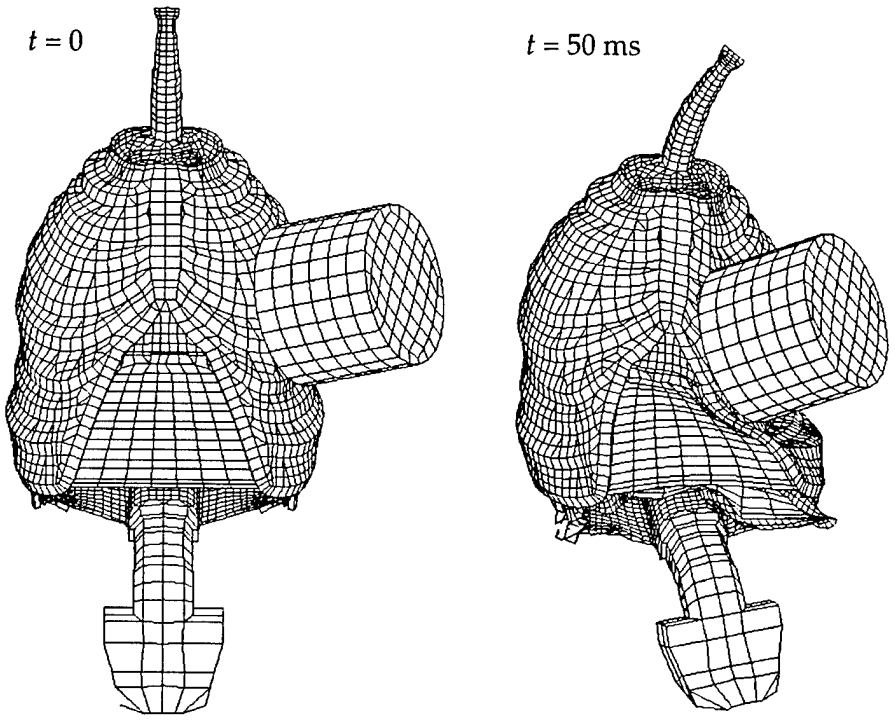


Figure 1. WSTM99 impacted by a ballistic pendulum (after Wang [1995].)

the trachea, the ligamentum arteriosum, and spinous process of the T7 vertebra. FE acceleration results were compared with these measurements.

WSTM99 is described in section 2 and critiqued with regard to this body armor application in section 3. An FE model for the multi-ply Kevlar vest is developed and added to WSTM99 in section 4. An FE model for the 9-mm bullet is developed in section 5. Section 6 considers the instrumentation employed in the Natick-AFIP-ATC tests. Computational results are presented in sections 7 and 8. In section 7 axial velocity contours throughout the skeletal system are shown; in section 8 computational axial accelerations are compared with accelerometer signals from the four locations. Results are summarized, and future plans are described, in section 9.

## 2. Description of WSTM99

### 2.1 Overview

WSTM99 consists of 37 distinct LS-DYNA "parts," which is an LS-DYNA term denoting a component defined by a single material. Each part comprises a self-contained mesh of finite elements. Three types of elements are employed: 8-node hexagonal solid elements (H), 4-node quadrilateral shell elements (S), and

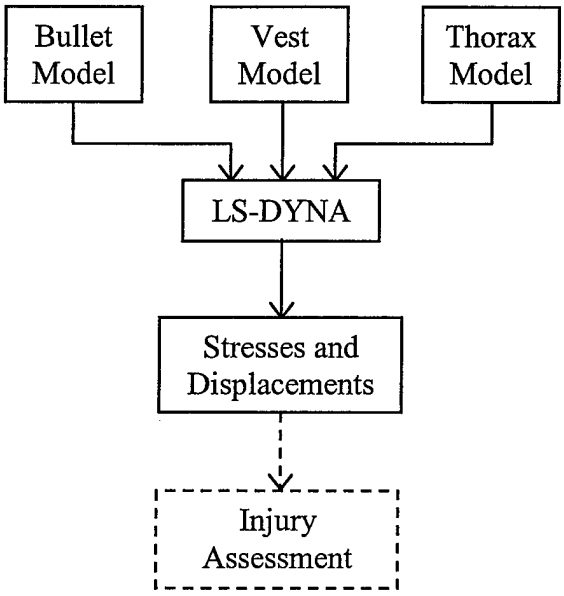


Figure 2. The computational scheme. The direct output from LS-DYNA is stresses and displacements throughout the thorax; the ability to map these to quantitative injury assessments is needed for the development of a body-armor design methodology.

2-node beam elements (B). The entire model contains 15,671 nodes—4,333 8-node solid elements, 11,075 shell elements, and 45 beam elements. The particular LS-DYNA contact algorithm used is specified by the command: *CONTACT_AUTOMATIC_SINGLE_SURFACE.

WSTM99, shown in Figure 1, explicitly represents the ribcage and its contents, plus the cervical and lumbar regions of the spine and the pelvis. Heart and lung tissue are represented as isotropic and nonlinear in compression, with stiffness increasing with increasing strain. LS-DYNA Material Model 57 ("Low-Density Foam") is used. This model also allows for an offset between the loading and unloading curves (hysteresis). For heart and lung tissue, quasi-static stresses were multiplied by 10 to account for rate hardening, and a hysteresis factor of 0.95 was employed.

All other tissues are modeled as isotropic linearly elastic. LS-DYNA Material Model 1 ("Elastic") is used. Each such material is described by a Young's modulus, $E$, a Poisson's ratio, $\nu$, and an initial density, $\rho_0$. Upon impact, two types of waves can appear within an isotropic linearly elastic material. These are longitudinal, or irrotational, waves, with velocity $c_L$ given by

$$c_L = \sqrt{\frac{(1-\nu)E}{(1+\nu)(1-2\nu)\rho}}, \tag{1}$$

and transverse, or equivoluminal, waves, with the smaller velocity $c_T$ given by

$$c_T = \sqrt{\frac{E}{2(1+\nu)\rho}} \tag{2}$$

(Kolsky 1963, pp. 4–15). Here, $\rho$ is the instantaneous density.

## 2.2 Skeletal Parts

The skeleton is represented in WSTM99 by 13 parts (Figure 3 and Table 1). All parts are meshed with 8-node hexagonal solid elements. All materials are modeled with isotropic linear elasticity.

## 2.3 Muscle Parts

Muscle parts in WSTM99 are described in Figure 4 and Table 2. All muscle parts are meshed with shell elements and assigned a uniform 10-mm thickness. Isotropic linear elasticity is applied to all materials.

## 2.4 Cardiovascular Parts

Cardiovascular parts are described in Figure 5 and Table 3. Heart is composed of hexagonal solid elements. It has two chambers. LS-DYNA Material Model 57 ("Low Density Foam") is applied to Heart.

Thoracic Aorta, Vena Cava, Pulmonary Vein, and Pulmonary Trunk are large blood vessels meshed with shell elements. Each is assigned a uniform thickness of 3.0 mm. Isotropic linear elasticity is applied to each.

Ligamentum Arteriosum is a ligament that joins two large arteries: the aorta and the pulmonary trunk. It is meshed with four shell elements and assigned a uniform thickness of 10.0 mm. Isotropic linear elasticity is applied.

Arteries is the only WSTM99 part meshed with beam elements. It represents arteries that branch off from the aorta. Isotropic linear elasticity is applied.

## 2.5 Respiratory Parts

Respiratory parts are described in Figure 6 and Table 4.

Left Lung and Right Lung are meshed with hexagonal solid elements. Internal cavities are not explicitly represented, but the small density of 0.6 g/cm$^3$ accounts for the internal presence of air. LS-DYNA Material Model 57 ("Low Density Foam") is again applied.

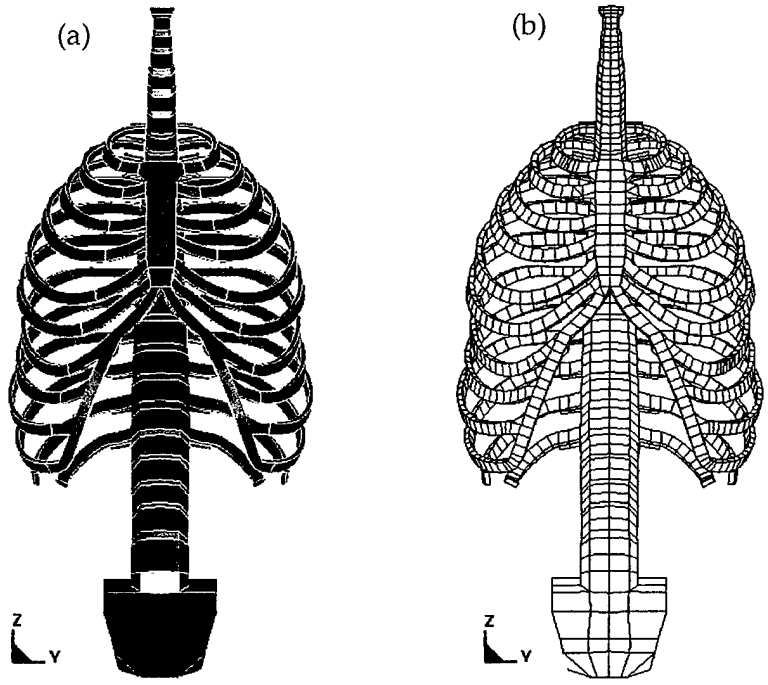


Figure 3. Anterior view of the WSTM99 skeletal parts: (a) the parts and (b) their meshes.

Table 1. Element type and material properties for the WSTM99 skeletal parts.

| Part and Material Name[a] | Element Type | $\rho_o$ (g/cm$^3$) | Part Mass (g) | $E$ (GPa) | $\nu$ | $c_L$ (m/s) | $c_T$ (m/s) |
|---|---|---|---|---|---|---|---|
| Lower Ribs | H | 2.0 | 585.6 | 11.51 | 0.30 | 2,783 | 1,488 |
| Upper Ribs | H | 158.02 | 7,581 | 11.51 | 0.30 | 313 | 167 |
| Sternum | H | 2.0 | 89.83 | 11.51 | 0.30 | 2,783 | 1,488 |
| Thoracic Vertebrae | H | 2.0 | 802.2 | 0.355 | 0.30 | 489 | 261 |
| Abdominal Vertebrae | H | 5.774 | 1,808 | 0.355 | 0.30 | 288 | 154 |
| Cervical Vertebrae | H | 22.302 | 635.1 | 0.355 | 0.30 | 146 | 78 |
| Top Vertebra | H | 1,474.1 | 3,168 | 0.355 | 0.30 | 18 | 10 |
| Pelvis | H | 109.5 | 37,780 | 0.355 | 0.30 | 66 | 35 |
| Costal Cartilages | H | 1.5 | 115.5 | 0.0245 | 0.40 | 187 | 76 |
| Thoracic Intervertebral Discs | H | 1.0 | 114.4 | 0.039 | 0.40 | 289 | 118 |
| Abdominal Intervertebral Discs | H | 5.7774 | 556.9 | 0.039 | 0.40 | 120 | 49 |
| Cervical Intervertebral Discs | H | 22.302 | 201.4 | 0.039 | 0.40 | 61 | 25 |
| Top Intervertebral Disc | H | 1,474.1 | 968.4 | 0.039 | 0.40 | 8 | 3 |

[a] Color coded to Figure 3.

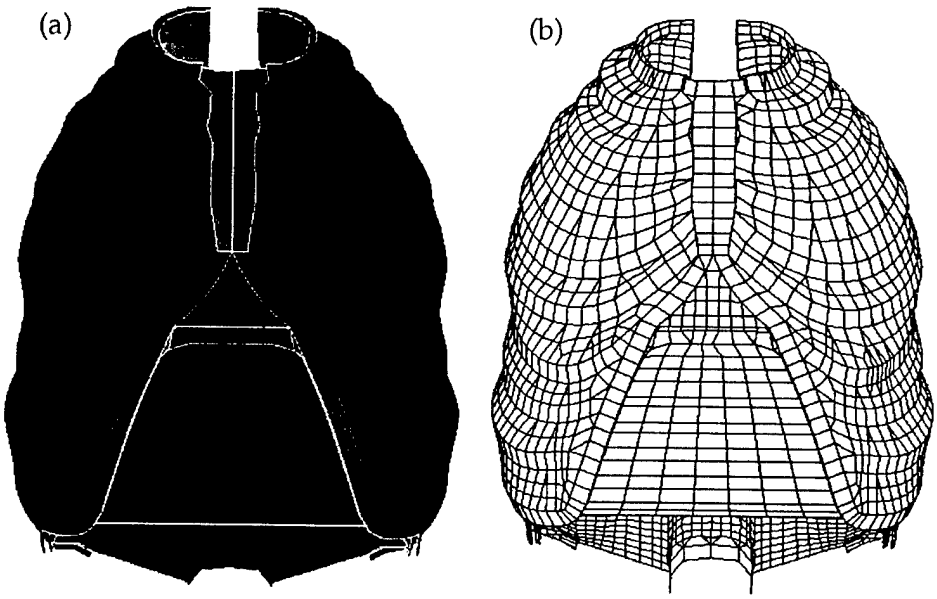


Figure 4. Anterior view of the WSTM99 muscle parts: (a) the parts and (b) their meshes.

Table 2. Element type and material properties for the WSTM muscle parts.

| Part and Material Name[a] | Element Type | $h$ (mm) | $\rho_o$ (g/cm$^3$) | Part Mass (g) | $E$ (MPa) | $\nu$ | $c_L$ (m/s) | $c_T$ (m/s) |
|---|---|---|---|---|---|---|---|---|
| Inner Left Intercostals | S | 10.0 | 1.0 | 1,026 | 1 | 0.30 | 37 | 20 |
| Inner Right Intercostals | S | 10.0 | 1.0 | 1,079 | 1 | 0.30 | 37 | 20 |
| Outer Left Intercostals | S | 10.0 | 1.0 | 1,070 | 1 | 0.30 | 37 | 20 |
| Outer Right Intercostals | S | 10.0 | 1.0 | 1,070 | 1 | 0.30 | 37 | 20 |
| Inner Abdominals | S | 10.0 | 1.0 | 184.6 | 1 | 0.30 | 37 | 20 |
| Outer Abdominals | S | 10.0 | 1.0 | 16.92 | 1 | 0.30 | 37 | 20 |
| Diaphragm | S | 10.0 | 1.0 | 1,046 | 1 | 0.30 | 37 | 20 |

[a]Color coded to Figure 4.

Trachea is meshed with shell elements. The part is assigned a uniform 3.0-mm thickness. Isotropic linear elasticity is applied.

The pulmonary blood vessels are discussed in section 2.4.

## 2.6 Digestive Part

The only digestive part, Esophagus, is described in Figure 7 and Table 5. It is meshed with shell elements and assigned a uniform thickness of 3 mm. Isotropic linear elasticity is applied.

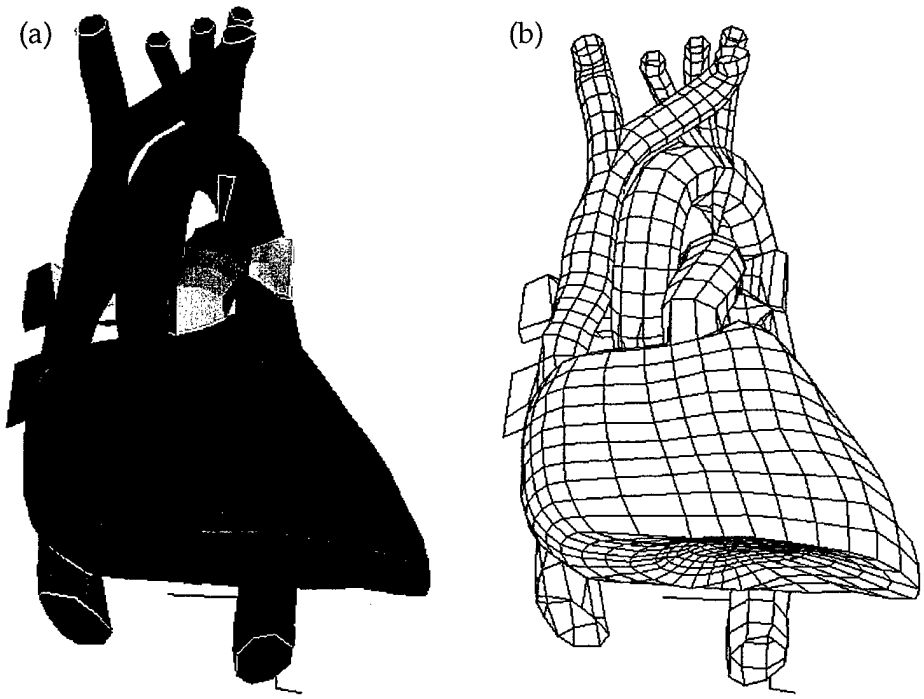


Figure 5. Anterior view of the WSTM99 cardiovascular parts: (a) the parts and (b) their meshes.

Table 3. Element types and material properties of the WSTM99 cardiovascular parts.

| Part and Material Name[a] | Element Type | $h$ (mm) | $\rho_o$ (g/cm$^3$) | $m$ (g) | $E$ (MPa) | $\nu$ | $c_L$ (m/s) | $c_T$ (m/s) |
|---|---|---|---|---|---|---|---|---|
| Ligamentum Arteriosum | S | 10.0 | 2.0 | 3 | 20 | 0.40 | 146 | 60 |
| Heart | H | —[b] | 1.0 | 455 | 3[c] | —[d] | —[e] | —[f] |
| Thoracic Aorta | S | 3.0 | 2.0 | 162 | 4 | 0.40 | 65 | 27 |
| Vena Cava | S | 3.0 | 2.0 | 74 | 20 | 0.40 | 146 | 60 |
| Pulmonary Vein | S | 3.0 | 2.0 | 52 | 20 | 0.40 | 146 | 60 |
| Pulmonary Trunk | S | 3.0 | 2.0 | 58 | 4 | 0.40 | 65 | 27 |
| Arteries | B | —[g] | 2.0 | 1 | 4 | 0.40 | 65 | 27 |

[a]Color coded to Figure 5.
[b]Does not apply to Element Type = H.
[c]Applies only in compression.
[d]Does not apply to Material Model 57.
[e]Equation (1) does not apply to Material Model 57.
[f]Equation (2) does not apply to Material Model 57.
[g]Does not apply to Element Type = B.

## 2.7 Miscellaneous Parts

The remaining parts are described in Figure 8 and Table 6. These include the pleural membranes that surround the lungs, two "neck" parts that form an artificial roof and prevent the aorta and esophagus from excessive lateral motion:

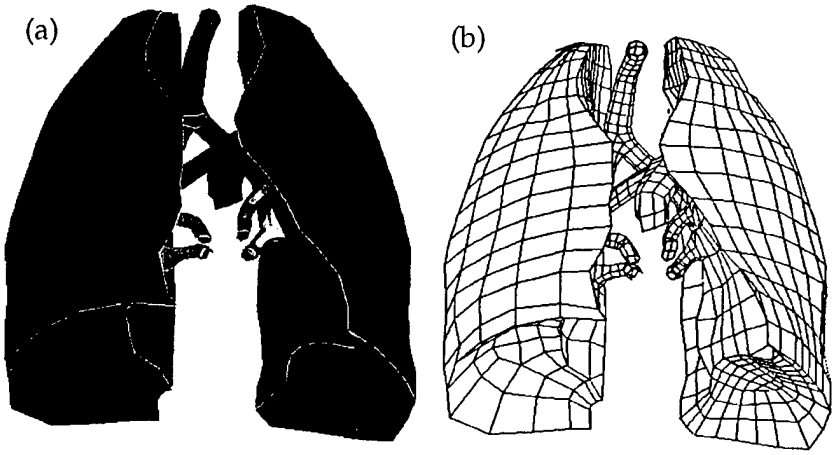


Figure 6. Anterior view of the WSTM99 respiratory parts: (a) the parts and (b) their meshes.

Table 4. Element type and material properties for the WSTM99 respiratory parts.

| Part and Material Name[a] | Element Type | $h$ (mm) | $\rho_o$ (g/cm³) | $m$ (g) | $E$ (MPa) | $\nu$ | $c_L$ (m/s) | $c_T$ (m/s) |
|---|---|---|---|---|---|---|---|---|
| Trachea | S | 3.0 | 2.0 | 62 | 10 | 0.40 | 104 | 42 |
| Left Lung | H | —[b] | 0.6 | 1,000 | —[c] | —[d] | —[e] | —[f] |
| Right Lung | H | —[b] | 0.6 | 1,130 | —[c] | —[d] | —[e] | —[f] |
| Pulmonary Vein | S | 3.0 | 2.0 | 52 | 20 | 0.40 | 146 | 60 |
| Pulmonary Trunk | S | 3.0 | 2.0 | 58 | 4 | 0.40 | 65 | 27 |

[a]Color coded to Figure 6.
[b]Does not apply to Element Type = H.
[c]Applies only in compression.
[d]Does not apply to Material Model 57.
[e]Equation (1) does not apply to Material Model 57.
[f]Equation (2) does not apply to Material Model 57.

Abdominal Mesentery and Abdominal Viscera. The latter accounts for the mass of the omitted abdominal anatomy. Isotropic linear elasticity is applied to all of these parts.

## 3. Critique of WSTM99 as Applied to Ballistics

WSTM99 was, at the time of its selection by ARL, arguably the most anatomically detailed FE thorax model that could be found in the open literature. It embodies much time-consuming labor in anatomy digitization. However, as applied to bullet vs. body armor simulations, WSTM99 has major shortcomings, all of which are amenable to fixing. Indeed, some have been at least partially addressed by Wayne State University since 1999 (Iwamoto et al. 2000; Lee and Yang 2001; Shah et al. 2001).

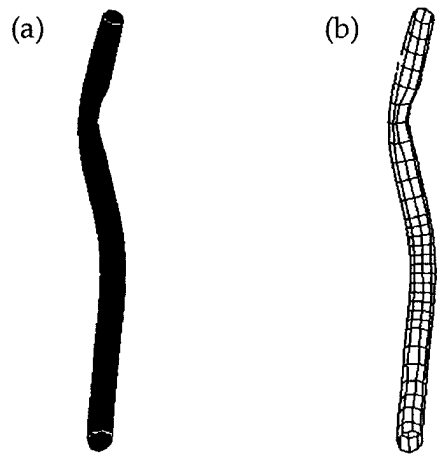


Figure 7. Anterior view of the WSTM99 Esophagus: (a) part and (b) mesh.

Table 5. Element type and material properties for the WSTM99 Esophagus.

| Part and Material Name[a] | Element Type | $h$ (mm) | $\rho_o$ (g/cm$^3$) | Part Mass (g) | $E$ (MPa) | $\nu$ | $c_L$ (m/s) | $c_T$ (m/s) |
|---|---|---|---|---|---|---|---|---|
| Esophagus | S | 3.0 | 2.0 | 59 | 3 | 0.40 | 57 | 23 |

[a]Color coded to Figure 7.

Needed refinements to WSTM99 fall into three categories: (1) anatomical representations, (2) meshing, and (3) biomaterial representations. These categories are considered in turn in sections 3.1, 3.2, and 3.3. For comparison, section 3.4 provides a brief review of the FE thorax models that have appeared in the literature.

## 3.1 Anatomical Representations Issues

(1) WSTM99 unrealistically contains much internal empty space (Figure 9). The subcutaneous layer—the layer of tissue that attaches skin to underlying tissues and organs, is omitted from the model. This layer is composed largely of adipocytes, or fat cells. These small sacks of liquid would introduce substantial dilatational stiffness and, in the case of high-frequency signals, substantial deviatoric stiffness as well.

There is no blood in the circulatory system. Heart, Thoracic Aorta, Vena Cava, Pulmonary Trunk, and Pulmonary Vein are all empty.*

* However, this omission of blood has been addressed in later versions of the Wayne State model (Shah et al. 2001).

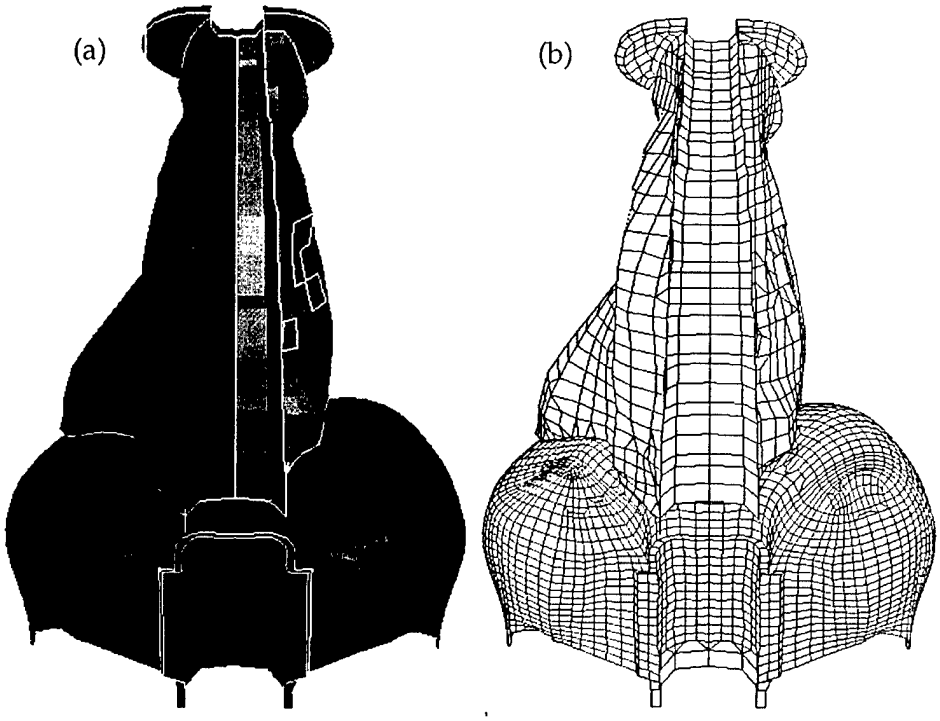


Figure 8. Posterior view of miscellaneous parts of WSTM99: (a) the parts and (b) their meshes.

Table 6. Element type and material properties for miscellaneous parts of WSTM99.

| Part and Material Name[a] | Element Type | $h$ (mm) | $\rho_o$ (g/cm$^3$) | Part Mass (g) | $E$ (MPa) | $\nu$ | $c_L$ (m/s) | $c_T$ (m/s) |
|---|---|---|---|---|---|---|---|---|
| Left Pleural Membrane | S | 3.0 | 2.0 | 309 | 400 | 0.40 | 655 | 267 |
| Right Pleural Membrane | S | 3.0 | 2.0 | 191 | 400 | 0.40 | 655 | 267 |
| Abdominal Mesentery | H | NA | 2.0 | 128 | 70 | 0.40 | 274 | 112 |
| "Neck" | S | 10.0 | 2.0 | 118 | 10 | 0.40 | 104 | 42 |
| "Neck" | H | NA | 2.0 | 54 | 10 | 0.40 | 104 | 42 |
| Abdominal Viscera | S | 10.0 | 9.34 | 10,280 | 1 | 0.30 | 12 | 6 |

[a]Color coded to Figure 8.

There is no air in the respiratory system. Trachea is empty. Left Lung and Right Lung are homogeneous solid structures. No air passages in the lungs are explicitly represented. The initial density of 0.6 g/cm$^3$ assigned to Left Lung and Right Lung is smaller than the density of lung parenchyma tissue. This small initial density was obtained from Dunn and Fry (1961), who weighed dog lungs. It is an effective density intended to introduce inertial effects of the presence air.

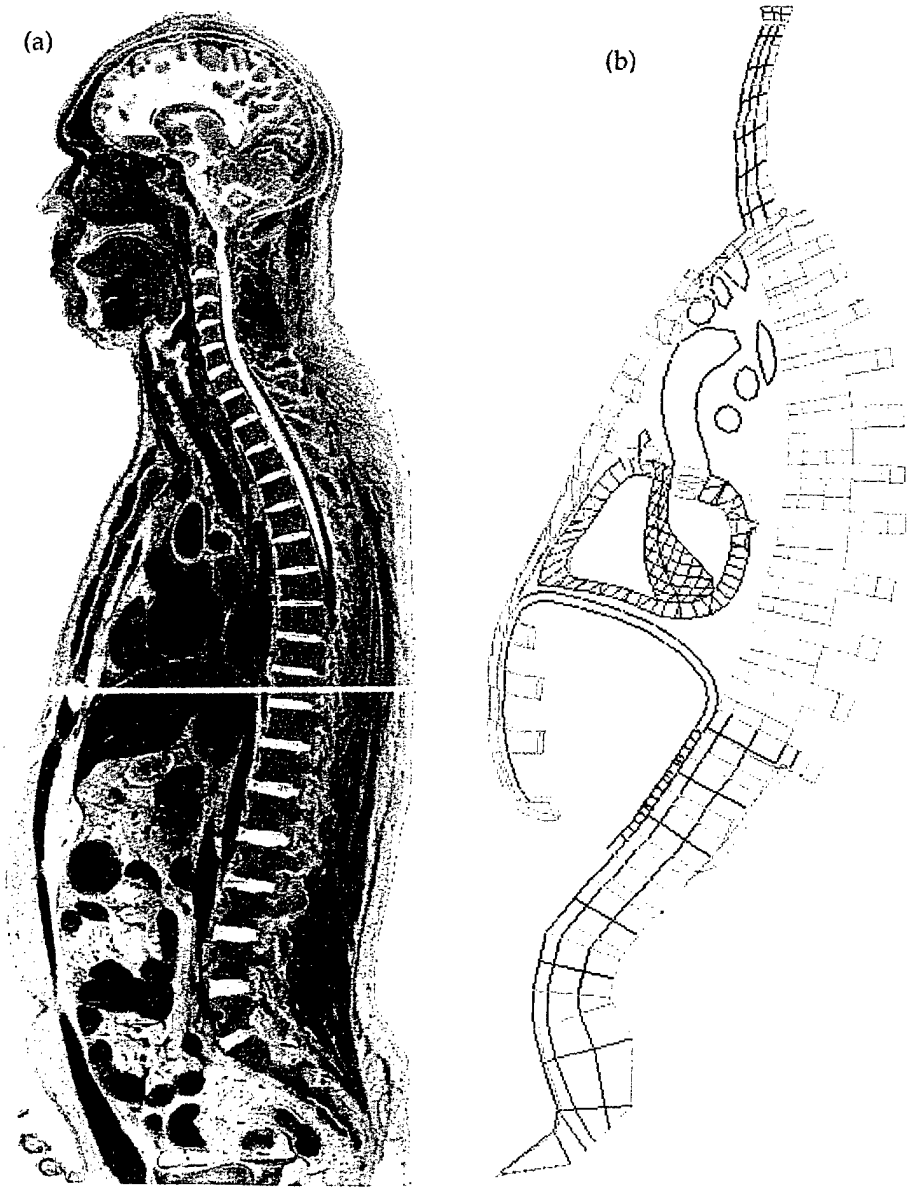


Source: Spitzer and Whitlock (1998), p. 499.
Reproduced with approval from Jones and Bartlett Publishers.

Figure 9. Median section (a) of the male anatomy and (b) of WSTM99. The latter contains much internal empty space.

(2) The complex musculature of the thorax is "abstractly" represented by two uniform-thickness layers that wrap around. Figure 10(a) shows a transverse or horizontal section through the male thorax at the elevation of the T8 vertebra. Muscles include the pectoralis major, covering the chest; the intercostals, composed of 12 discrete pairs of inner and outer sheets strung between each adjacent pair of ribs; the latissimus dorsi; the serratus anterior; the trapezius; and the longissimus thoracis, associated with the spine.

Figure 10(b) shows the WSTM99 representation. Each part associated with muscles has a uniform 10-mm thickness (see Table 2). It may prove difficult to represent the muscular anatomy in accurate detail. A problem with the abstract approach adopted by Wang (1995) is that it has probably led to a level of input adjustment (e.g., perhaps the 10-mm uniform thickness for all muscle parts) inconsistent with a "first-principles"-based methodology. Such a methodology should be based on only these ingredients: the equations of motion (conservation of mass, momentum, and energy), an accurate representation of anatomy, and constitutive properties determined independently from the ballistics test to which the model is applied.

(3) Anatomy of the spinal vertebrae is crudely represented. This is significant in the present application because, as will be discussed in section 6, the T7 vertebra is one of four locations from which accelerometer data were obtained. The crude representation of the vertebrae may also have affected the solution elsewhere. The latter consideration would be even more relevant in cases of posterior impact.

Figure 11(a) shows the actual anatomy of a thoracic vertebra as viewed from above. The spinal cord of neurons passes through the vertebral foramen. The vertebral body, located anteriorly to the foramen, is largely composed of trabecular (cancellous) bone and hence has a smaller stiffness than either the sternum or the ribs (see Table 1). Posteriorly, the spinal cord is surrounded by a hoop of bone, the vertebral arch, that includes, in the order of increasing distance from the body, the pedicle, the transverse process, the lamina, and the spinous process. A pair of ribs attaches to the body and to the transverse processes. The facet and demifacet joints of attachment contain small pads of cartilage.

Figure 11(b) shows much of the WSTM99 Thoracic Vertebrae part as viewed posteriorly. The anatomy in Figure 11(a) has clearly been abstracted. The spinous process is missing. Hence, in section 7.5 experimental acceleration data from the T7 spinous process can only be compared with LS-DYNA accelerations for two elements at a less specific location on the vertebral arch. In WSTM99, Upper Ribs and Lower Ribs

(a)

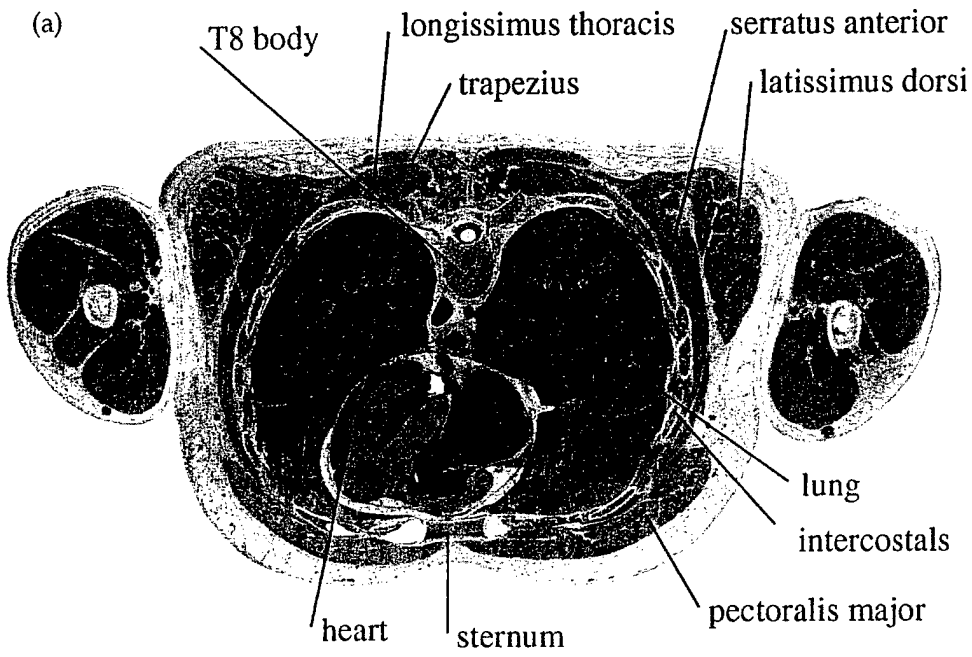


Source: Spitzer and Whitlock (1998), p. 492 (modified).
Reproduced with approval from Jones and Bartlett Publishers.

(b)

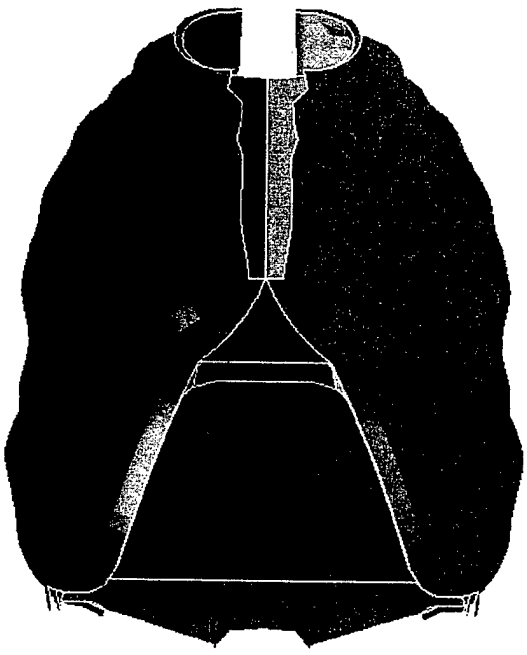

Figure 10. Human thoracic musculature (a) as sectioned and viewed superiorly (red labels indicate muscles) and (b) as represented in WSTM99.

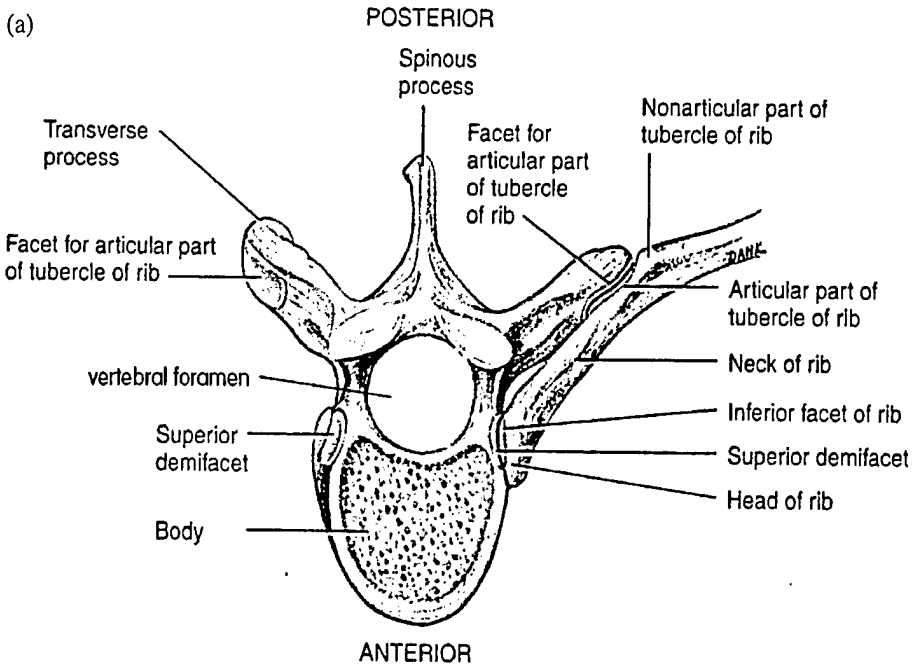


Source: Tortora and Grabowski (2000), p. 212.

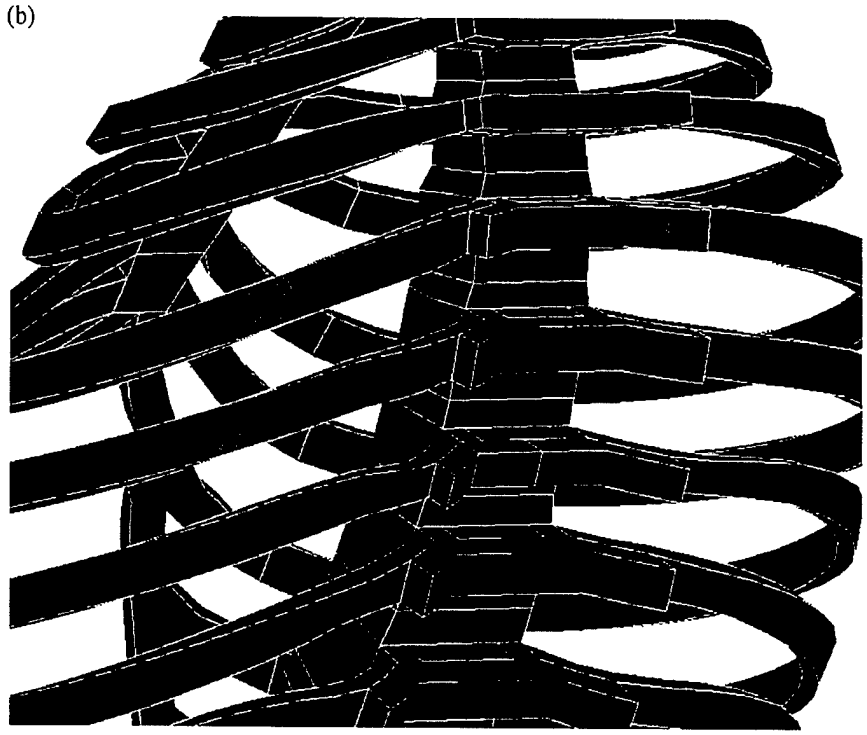


Reproduced with approval from John Wiley & Sons.

Figure 11. (a) Superior view of a thoracic vertebra and (b) posterior view of the thoracic skeleton as represented in WSTM99.

share common nodes with the transverse processes of Thoracic Vertebrae. This neglects any flexibility offered by the cartilage pads.

(4) Anatomy of the sternum is crudely represented. Sternum in WSTM99 is composed of a homogeneous elastic material with properties representative of cortical bone, namely a Young's modulus, $E$, of 11.51 GPa and an initial density, $\rho_0$, of 2.0 g/cm$^3$ (Table 2). The physical sternum actually consists of three fused parts: (1) the manubrium, (2) the sternal body, and (3) the xiphoid process (Figure 12). The manubrium and sternal body each include a thin cortical shell surrounding a less stiff core of trabecular bone (Moore and Dalley 1999 [p. 68]; Spitzer and Whitlock 1998 [pp. 64–89]). The xiphoid process is composed of hyaline cartilage (Snell 2000 [p. 47]) and hence should have properties similar to those of Costal Cartilages in WSTM99.

## 3.2 Meshing Issues

(1) The entire WSTM99 mesh, with a typical element edge length of 10 mm, is coarse for bullet-impact simulations. The mesh density was adequate for the pendulum impactor problem, shown in Figure 1, for which it was developed.

Mesh refinement will not be trivial. The bullet-vest-WSTM99 problem that is described in sections 4, 5, 7, and 8 required about 10 hr of CPU time to run to 25 ms in a non-parallelized calculation on a single Silicon Graphics Inc. R12000 processor. If the edge lengths of each element in WSTM99 and fabric vest were indiscriminately halved to about 5 mm, still locally a very coarse mesh for impact by a 9-mm bullet, the CPU time would increase by a factor of 8 to 16. Mesh refinement would therefore have to be gradually tapered from the location of bullet impact. A caveat is that abrupt jumps in mesh density from one part to its adjacent neighbor can cause the contact algorithm to behave improperly.

(2) Use of one 8-node hexagonal element through the thickness and one-point integration resulted in zero-bending stiffness for the ribs, costal cartilage, and the sternum. In the literature, the ribs have been assumed to behave as curved beams, equilibrating a transverse load via bending stresses (e.g., the experimental-data reduction by Granik and Stein [1973], the previous FE thorax models by Roberts and Chen [1970] and by Sundaram and Feng [1977]. Bending stresses involve a neutral surface dividing the beam's cross section into a region of axial compression and one of axial tension. If this assumption of beam-like behavior, particularly plausible for the ribs and costal cartilage, is in fact correct, then the WSTM99 meshing approach leads to excess skeletal flexibility under frontal impact, presumably compensated for by the muscle parts.

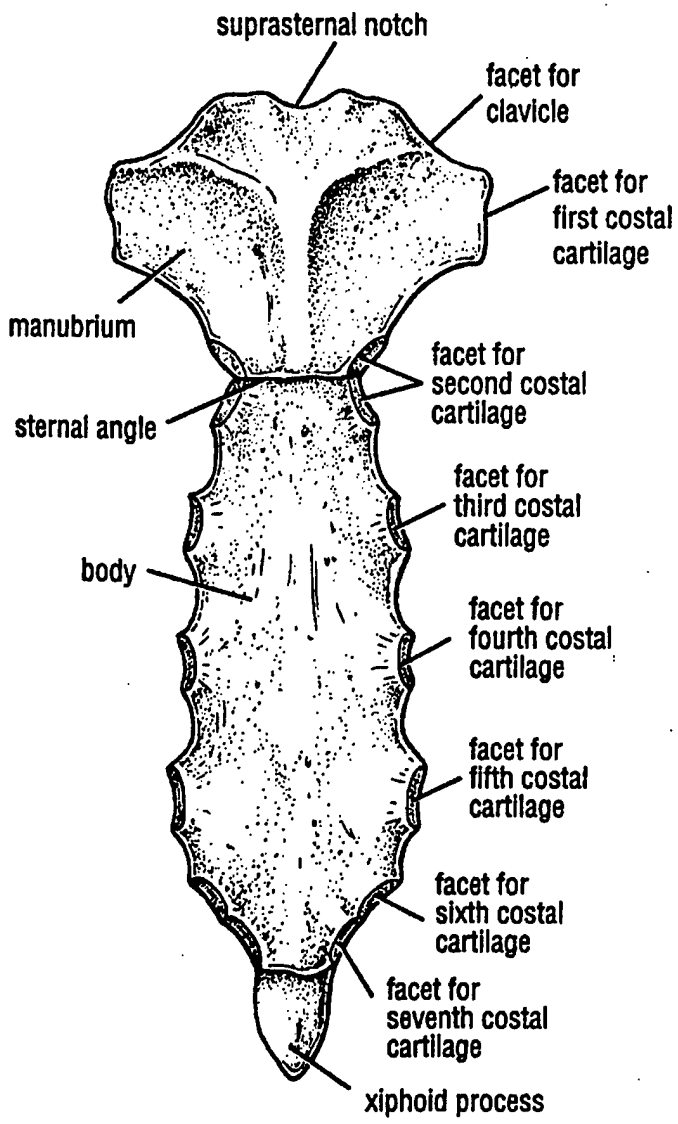


Source: Snell (2000), p. 47.
Reproduced with approval from Lippincott Williams & Wilkens.

Figure 12. The physical sternum.

The dangers of applying a single solid element and reduced integration to beam problems was perhaps first documented and explained independently by Irons (1971) and by Pawsey and Clough (1971). A concise presentation is contained in Cook et al. (1989) on pp. 188–196 and 232–233. The explanation will be presented in two dimensions, in terms of 4-node quadrilaterals instead of 8-node hexagons. The argument is unchanged by a passive transverse third dimension.

In response to a bending moment, classical (Bernoulli-Euler) linearly elastic beam theory calls for the deformation pattern shown in Figure 13(c). This pattern involves zero shear strain throughout the beam. A 4-node quadrilateral element (Figure 13[a]) has a bilinear shape function that interpolates velocities at the four vertex nodes to interior points within the element. The edges of such an element are constrained to remain straight even under a bending moment (Figure 13[b]). Such a deformed quadrilateral element does not have identically zero shear strain throughout. The spurious non-zero shear strain arising from limitations in the element's shape function is called "parasitic shear." Its presence means that some of the applied energy has spuriously gone into strain energy associated with shear deformation. This component of applied energy is therefore unavailable for bending deformation. Hence, if "full integration" were used, i.e., if 2 × 2 Gaussian quadrature were used to retain the full shape function during numerical integration, use of a single quadrilateral element through the beam thickness would result in a model that is too stiff in response to transverse loading.

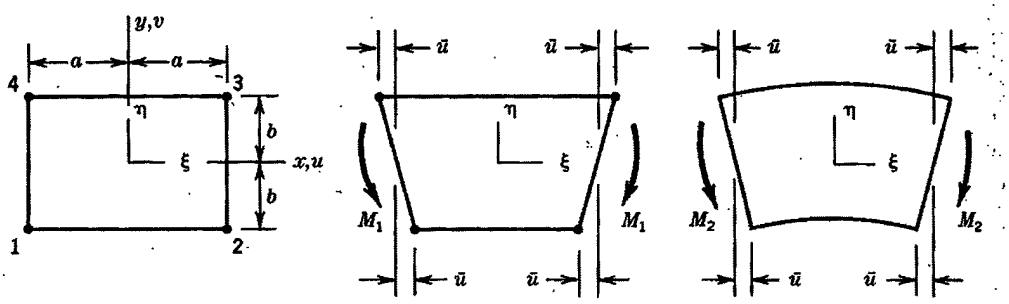


Source: Cook et al. (1989), p. 232.

Figure 13. A fully integrated single element through the thickness produces a beam that is too stiff in bending because some strain energy is associated with shear deformation rather than bending.

Shear strain, while not zero throughout the deformed quadrilateral element in Figure 13(b), is zero at the element's centroid. Single-point Gaussian quadrature makes use of only the centroid values of strain components. This approach discards contributions from much of the element's shape function and results in no strain energy consumed by spurious shear deformation. However, this approach of single-point integration is really an overcompensation in terms of resistance to transverse loading. In effect this approach results in a strain tensor that appears to be spatially constant throughout the element. Hence, bending stresses, compressive on one side of the neutral surface and tensile on the other, are not generated. Instead,

stresses arise only in response to in-plane stretching and compression of the structure. The result is a model that is now too flexible under transverse loading.*

(3) The muscle parts are meshed with shell elements. This ensures that the effects of bending stresses will arise in these parts in response to transverse loading. However, it seems likely that muscles generate primarily membrane stresses rather than bending stresses. In effect, WSTM99 may have reversed the responses of muscle and skeleton to a transverse load.

## 3.3 Biomaterial Representations

(1) In WSTM99, some parts on the periphery of the thorax are assigned artificially large initial densities in order to introduce inertial contributions from anatomical structures omitted from the model. Omitted structures include the limbs, head, shoulder, abdominal viscera, and soft tissue of the neck.

The procedure is illustrated in Figure 14 and Table 7 for Upper Ribs. Lower Ribs includes the lowest nine ribs. Lower Ribs and Sternum are signed properties from the compact bone literature. Upper Ribs, which includes the top three ribs, is assigned the same elastic properties as Lower Ribs. However, Upper Ribs is assigned a density 79 times that of Lower Ribs. Evidently, Upper Ribs has been used to incorporate the mass of the hands, arms, and shoulders omitted from the model. A problem with this approach is that the longitudinal and transverse wave speeds of Upper Ribs is each unrealistically $\sqrt{79}$ or 8.9 times smaller than its counterpart for compact bone. This will affect the solution.

Table 1 reveals that the same procedure has been followed for other skeletal parts. Pelvis, Abdominal Vertebrae, Cervical Vertebrae, and Top Vertebra all share elastic properties with Abdominal Vertebrae but all have been assigned a larger initial density than Abdominal Vertebrae. Abdominal Intervertebral Discs, Cervical Intervertebral Discs, and Top Intervertebral Disc have an analogous relationship with Thoracic Intervertebral Discs.

Outside of the skeletal system, Abdominal Viscera, listed in Table 6, is a fictitious shell structure that lines Diaphragm. It has the elastic properties of muscle, the same 10-mm thickness as Diaphragm and other muscle

* Since 1999, Wayne State University has substantially altered its approach to rib representation. Currently, each rib's cross section is modeled with a single 8-node hexagonal element for the trabecular core, surrounded by shell elements to represent the cortical exterior (Iwamoto et al. 2001; Yang 2002). Thus, the ribs develop bending stresses in more recent versions of the Wayne State model.

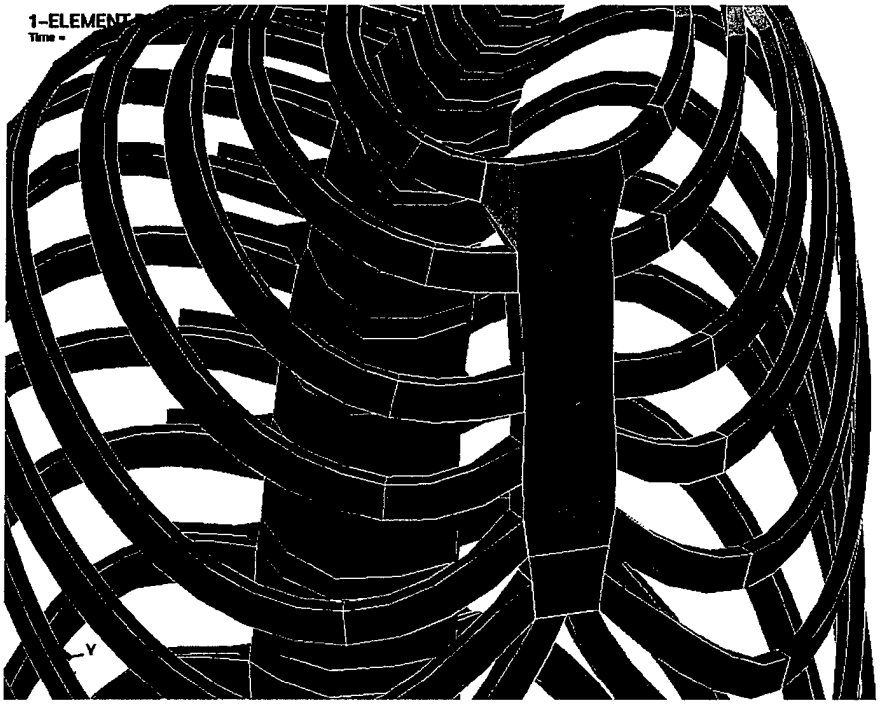

Figure 14. Thoracic skeleton in WSTM99; Lower Ribs and Upper Ribs are distinct parts.

Table 7. Initial densities and longitudinal and transverse wave speeds for Sternum, Lower Ribs, and Upper Ribs.

| Part and Material Name[a] | $\rho_o$ (g/cm$^3$) | $E$ (GPa) | $c_L$ (m/s) | $c_T$ (m/s) |
|---|---|---|---|---|
| Sternum | 2.0 | 11.51 | 2,783 | 1,488 |
| Lower Ribs | 2.0 | 11.51 | 2,783 | 1,488 |
| Upper Ribs | 158.02 | 11.51 | 313 | 167 |

[a]Color coded to Figure 14.

parts, but a larger density than muscle. Abdominal Viscera was presumably introduced to account for the mass of the soft tissue of the abdominal cavity separated from the thoracic cavity by the diaphragm. Abdominal soft tissue includes the liver, spleen, stomach, intestines, kidneys, ureter, etc.

An alternative procedure for introducing inertia of omitted anatomy must be sought. Ideally, local wave speeds should not be rendered unrealistically small.*

* Since 1999, Wayne State University has reduced the use of artificially large densities by expanding the thorax model to include detailed FE models for the shoulder complex and arms (Iwamoto et al. 2000) and the abdominal viscera (Lee and Yang 2001).

(2) Stiffness properties of every biomaterial other than heart and lung tissue are modeled using isotropic linear elasticity (LS-DYNA Material Model 1), with elastic constants $E$ and $\nu$ based on quasi-static data. This approach ignores anisotropy, nonlinearity, and rate dependence.

With the possible exception of bone, there is a lack of dynamic constitutive data for thoracic materials. It is difficult to obtain constitutive data for soft materials at large strain rates. The conventional split Hopkinson bar technique is problematic in this situation for two reasons. First, the traditionally metal incident and transmitter bars severely mismatch the impedance of the specimen so that only a small fraction of the incident stress wave enters the specimen. Second, the specimen's low longitudinal wave speed means that a homogeneous state of stress within the specimen takes a long time to achieve. The usual procedure of processing strain gauge output from the incident and transmitter bars assumes such a state of stress.

(3) For Heart, Left Lung, and Right Lung, Wang (1995) attempted a more sophisticated constitutive representation than Hooke's Law. He applied LS-DYNA Material Model 57, "Low-Density Foam." This model is still isotropic and rate independent. It is still linearly elastic in tension. Its refinement over the model applied to the other biomaterials involves compression, for which the user can specify a nonlinear stress-strain curve point by point. The user can also specify a hysteresis factor less than or equal to 1, from which the unloading curve is constructed from the input curve.

Wang (1995) seems to have digitized Figure 82 from Yamada (1970) for heart muscle and Figure 2 from Vawter et al. (1979) for lung tissue, reproduced here in Figures 15 and 16, respectively. However, these nonlinear curves apply in tension, and Wang (1995) mistakenly applied them to compression. Furthermore, in an attempt to incorporate effects of large strain rates, Wang (1995) multiplied by 10 each stress value digitized from Figures 15 and 16.

## 3.4 Other FE Thorax Models

Perhaps the earliest FE thorax model is that of Roberts and Chen (1970), which represented the ribs, costal cartilage, sternum, and even vertebral column using beams elements, thereby ensuring the generation of bending stresses (Figure 17). All other anatomical features were neglected in the model. Two distinct materials appear: "bone" and "cartilage." Linear elasticity was applied to each. The model was applied to small displacement, small strain, elastostatic analyses of three distinct frontal loadings.

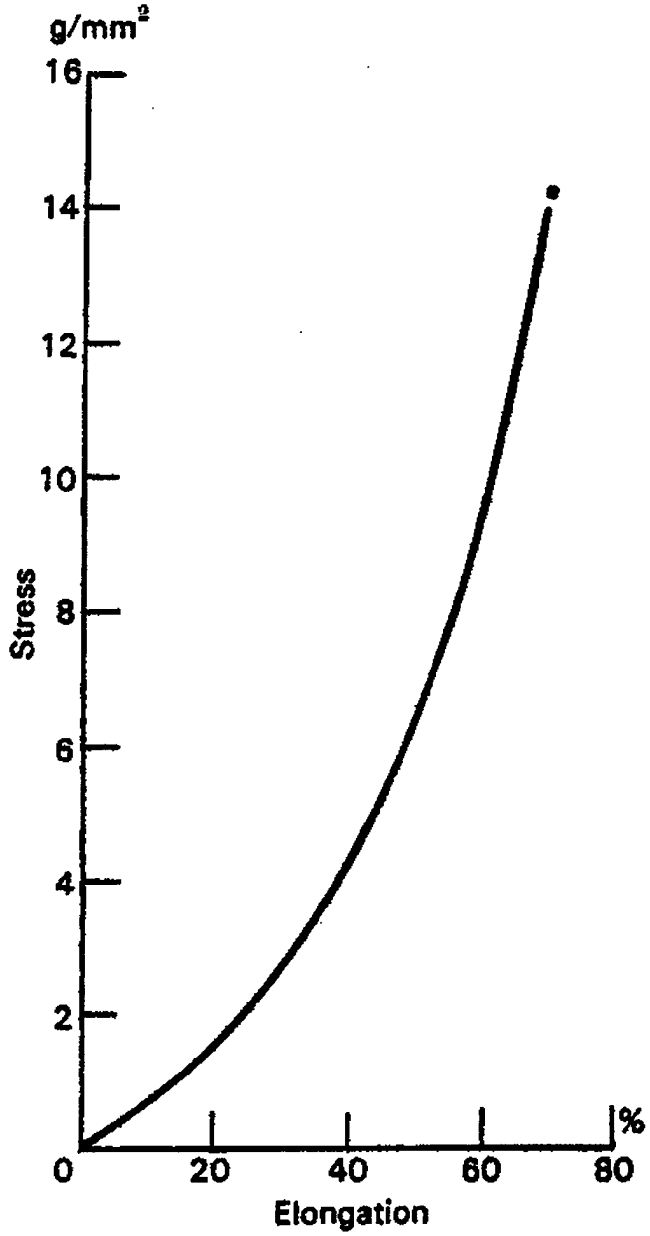


Source: Yamada (1970), p. 107.

Figure 15. Quasi-static stress-strain curve in uniaxial tension for cardiac muscle from humans 20–29 years of age.

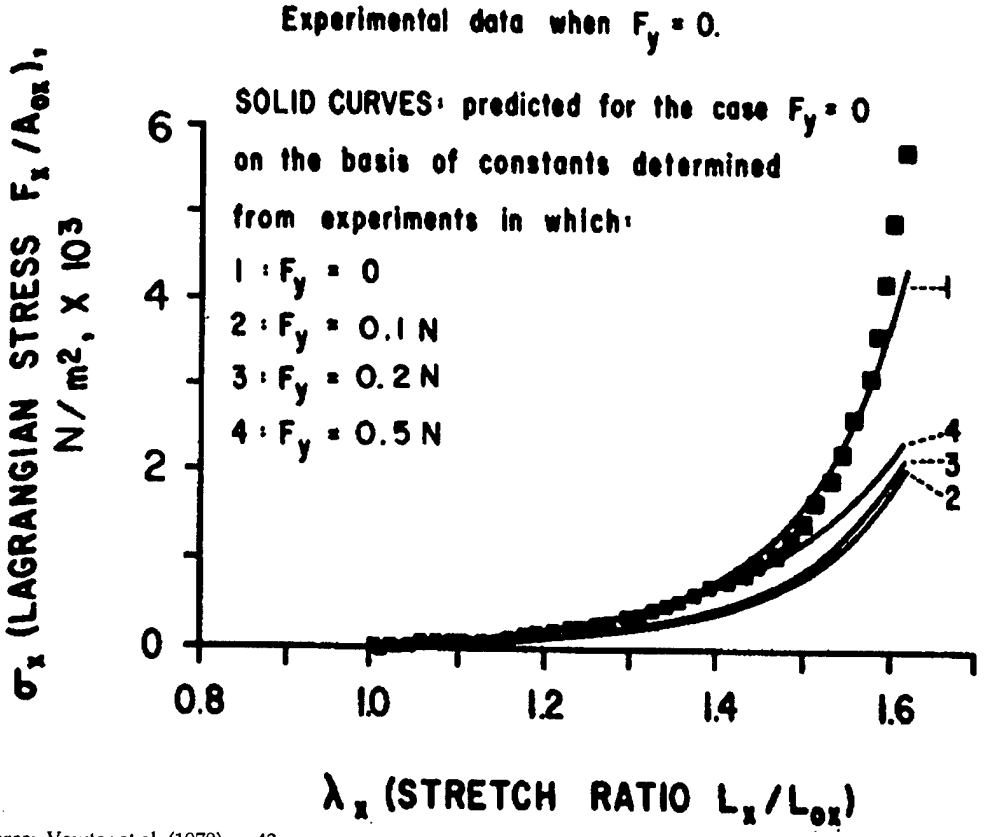


Source: Vawter et al. (1979), p. 43.

Figure 16. Quasi-static stress-strain curve for dog's lung parenchyma in uniaxial tension. The discrete squares are the experimental data used by Wang (1995). The solid curves are theoretical predictions; the cases when $F_y \neq 0$ correspond to biaxial loading (not applicable to the experimental data shown).

Sundaram and Feng (1977) retained the application of beam elements to the ribs, costal cartilage, and spine. They applied plate elements to the sternum, added a layer of muscles modeled with membrane elements, and added a small number of large solid elements to represent internal soft tissue. The use of beam and plate elements ensured bending stresses in the skeletal parts, while the use of membrane elements ensured the absence of bending stresses in the thoracic muscles. They also assumed linear elastic behavior for all materials and restricted attention to small displacement, small strain, elastostatic analyses.

Chen (1978) added a similarly crude representation of soft tissue to the model in Roberts and Chen (1970), which he then applied to dynamic impact problems. Small displacements, small strains, and linear elasticity were still assumed.

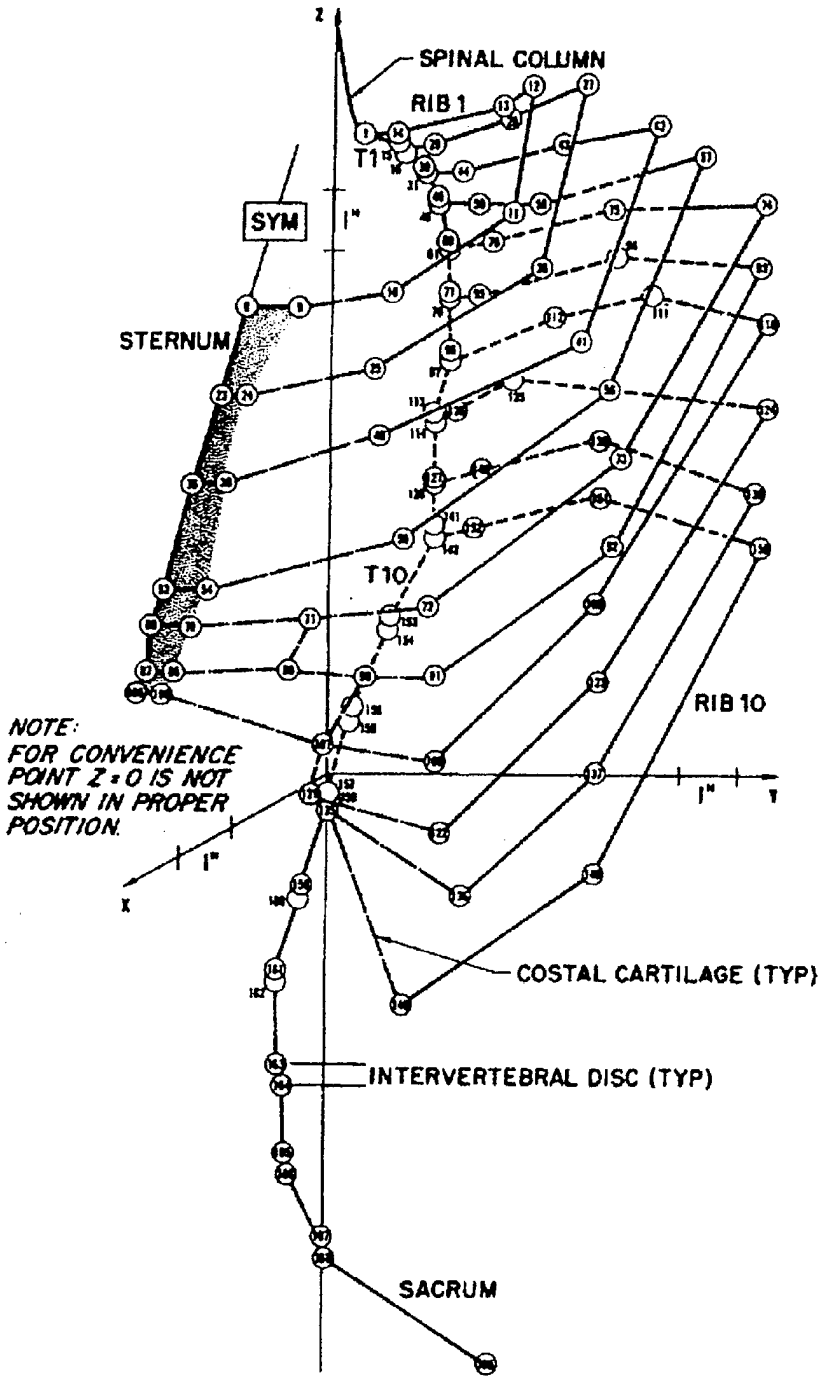


Source: Roberts and Chen (1970), p. 528.

Figure 17. The FE thorax model of Roberts and Chen (1970); only the skeleton is represented, and beam elements are used.

Wang (1995) cites Plank and Eppinger (1991), which presents a thorax model that seems to be the origin of some features of WSTM99. Moreover, Plank and Eppinger (1991) studied the same problem as did Wang (1995) (compare Figures 1 and 18[a]). Plank and Eppinger (1991) employed exclusively 8-node hexagonal elements. In particular, this applies to the skeletal parts, the ribs, costal cartilage, sternum, vertebrae, and intervertebral discs. Figure 18(b) shows the ribs and costal cartilage to be meshed with two elements through the thickness in at least one of the thickness directions. This arrangement would be able to capture at least some bending stresses even in the case of one-point Gaussian integration. Muscles were explicitly included. The internal viscera were not modeled in detail but lumped together as a homogeneous "Viscoelastic Interior." Plank and Eppinger (1991) originated the procedure of using artificially dense parts, "Concentrated Head Mass," "Concentrated Arm Mass," and "Concentrated Lower Body Mass," to introduce the mass of omitted anatomy. Linear viscoelasticity was applied to muscles and Viscoelastic Interior. Linear elasticity was applied to all other materials. The analysis included dynamic effects and effects of large deformation and displacements.

Masiello (1997) presents an FE thorax model developed by JAYCOR Corporation. This model complements most others in that the lungs and heart are explicitly represented while all other structures (skeleton, muscles, etc.) are smeared into two homogeneous parts: "Epidermis/Muscle/Skeletal" and "Abdomen" (Figure 19). The model was developed specifically for blast loading problems in which injury to the heart and lungs was deemed to be the main focus.

Jolly and Kwon (2000) used beam elements to model the ribs, costal cartilage, sternum, vertebrae, and intervertebral discs. Muscles were modeled with 8-node hexagonal elements. Linear elasticity was applied to bone and cartilage. A linear viscoelastic model, after Plank and Eppinger (1991), was applied to muscle. All internal viscera were omitted. This model was specifically developed for body armor applications. The two problems analyzed in Jolly and Kwon (2000) are a 9-mm Remington bullet against a fabric armor and a 7.62-mm North Atlantic Treaty Organization (NATO) bullet against fabric plus a ceramic plate.

# 4. Adding a Kevlar Vest to WSTM99

## 4.1 FE Mesh

An FE model of a multi-ply fabric vest composed of Kevlar KM2 was added to the exterior of WSTM99. This model consists of a single 8-node hexagonal element through the thickness. Hence, the plies are not represented individually but are combined into a homogeneous medium. The total areal density of the

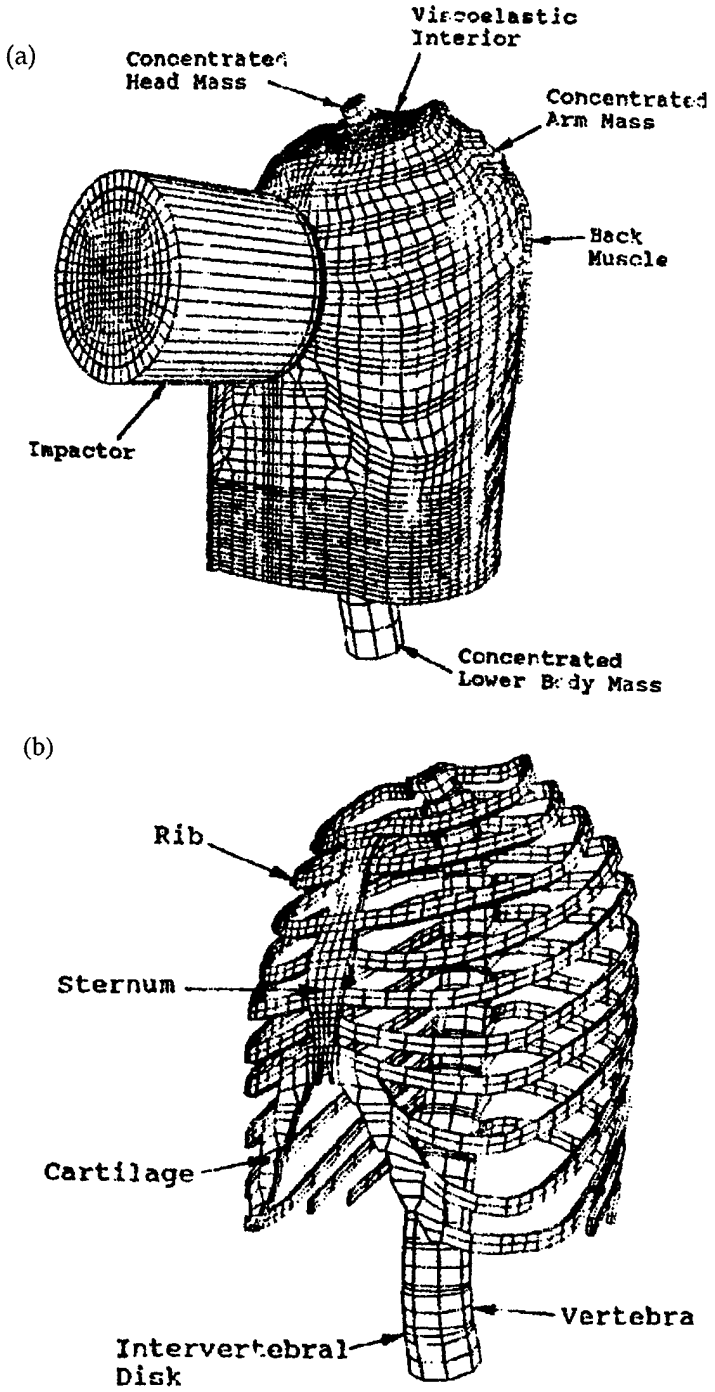


Source: Plank and Eppinger (1991), p. 903.

Figure 18. The FE thorax model of Plank and Eppinger (1991): (a) the entire model with impactor and (b) the skeletal parts.

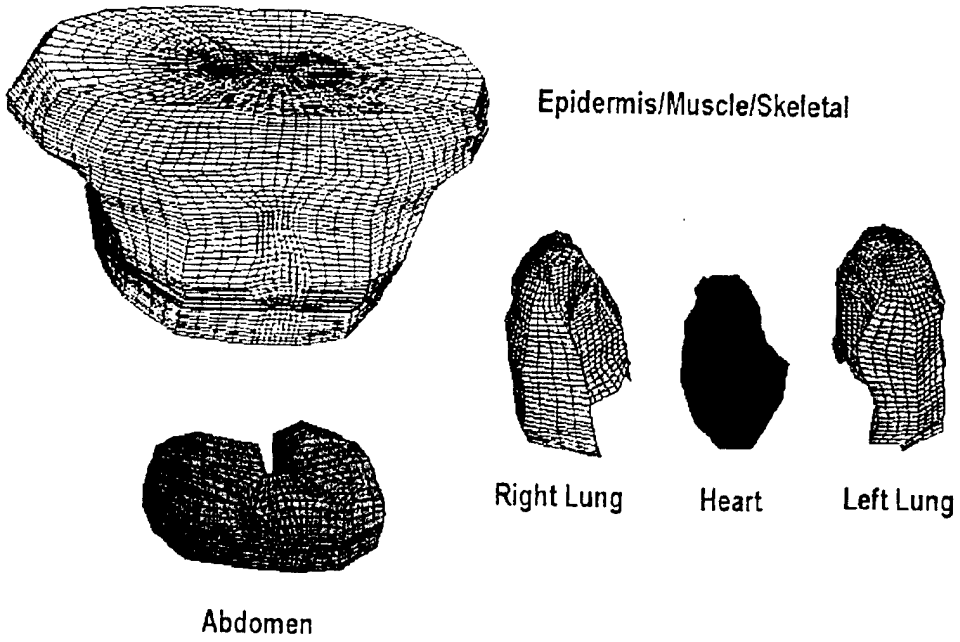


Source: Masiello (1997), p. 2-2.

Figure 19. The FE thorax model of Masiello (1997).

23 plies was known to be 5.22 kg/m$^2$. Following the method in Johnson et al. (1999), the effective initial thickness, *d*, assigned to the FE model of the vest is the ratio of areal density to the initial fiber volumetric density, or 1440 kg/m$^3$. This ratio is 3.63 mm. In this way, the fiber's volumetric density, needed to obtain proper wave speeds, and the vest's areal density are both accurately represented in the FE model.

A single integration point was applied to each 8-node hexagonal element. This reduced integration scheme, in effect, resulted in a spatially uniform stress tensor within each finite element, i.e., through the vest's thickness. Hence, bending stresses were discarded. The vest generated only in-plane membrane stresses and a spatially uniform transverse stress (see the discussion in section 3.2 in the context of ribs, costal cartilage, and sternum).

This approach of neglecting bending stresses and retaining only in-plane membrane stresses and a uniform transverse stress, while problematic in the case of ribs, costal cartilage, and sternum, seems appropriate as applied to the fabric vest. Each ply of the plain woven vest is composed of a set of warp yarns and an orthogonal set of fill yarns (Figure 20). Upon ballistic transverse impact, the vest undergoes out-of-plane deflection and each yarn is elongated in axial tension. In addition, yarns in the vicinity of impact are transversely compressed.

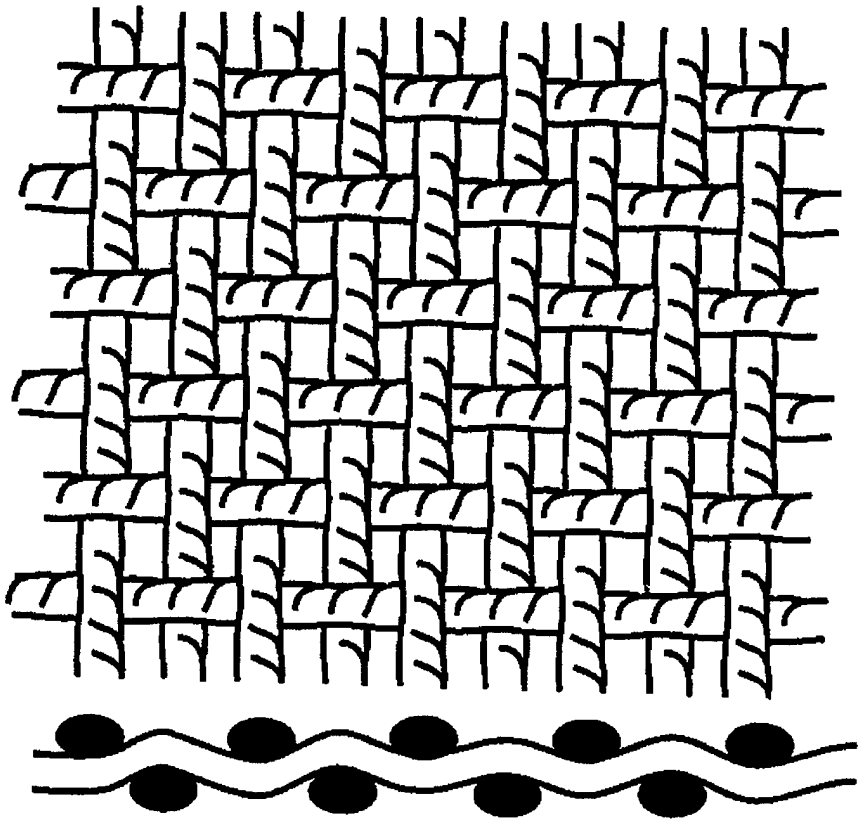

Source: Warner (1995), p. 271.

Figure 20. Plain weave structure of a ply of the Kevlar vest.

HyperMesh software (Altair Engineering 2000) was used to generate the mesh of a fabric vest's FE model. First "lines" were constructed linking outermost nodes on WSTM99 (Figure 21). A "skin" was then created using bicubic splines. This skin was moved outwards by 2 mm to ensure clearance of WSTM99 by all vest nodes. A uniform-thickness mesh was created using this skin as the inner surface (Figure 22). The element's typical in-plane dimension of 10 mm was chosen for compatibility with WSTM99 (Figure 23).

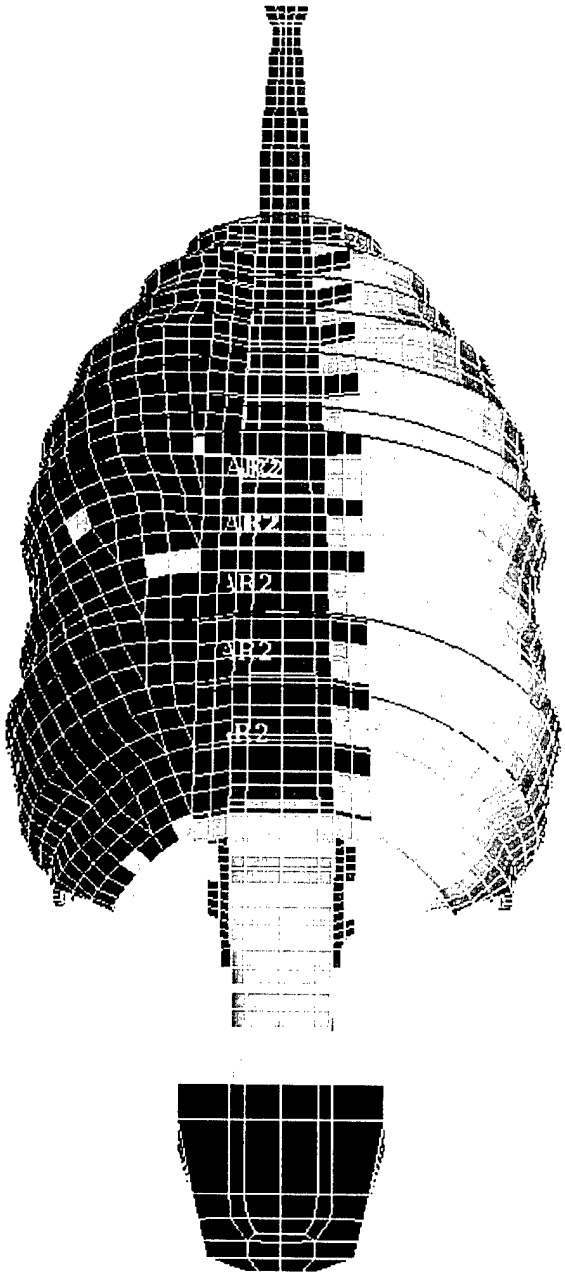

Figure 21. HyperMesh was used to generate lines linking outermost nodes on WSTM99.

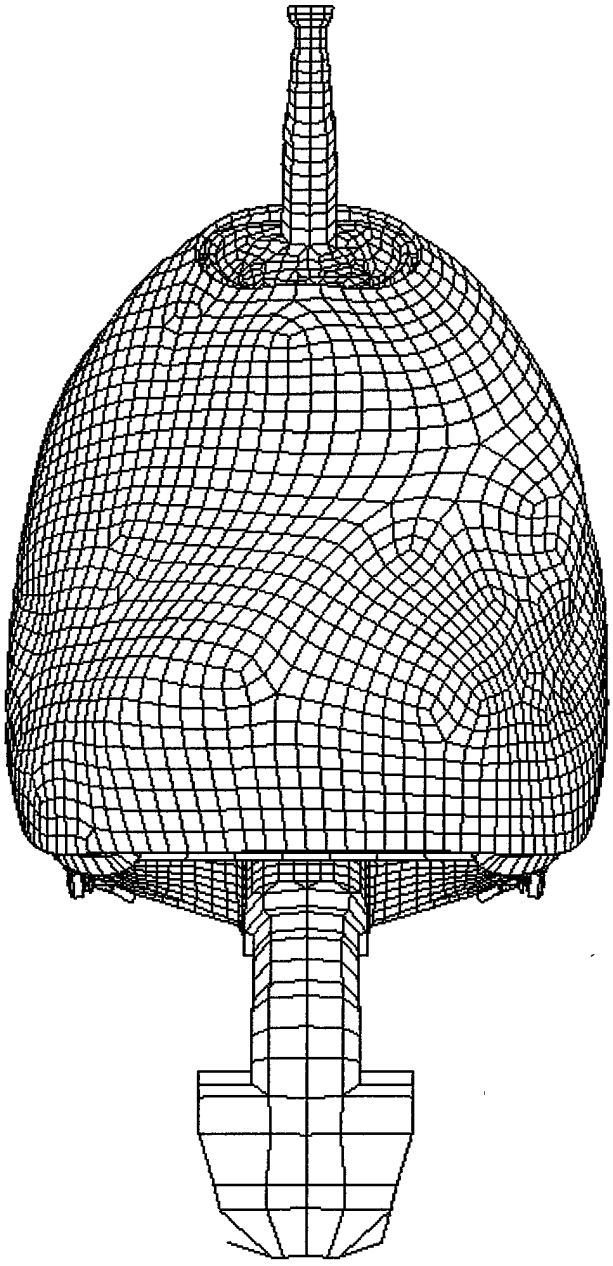

Figure 22. A mesh for the fabric vest was added to WSTM99.

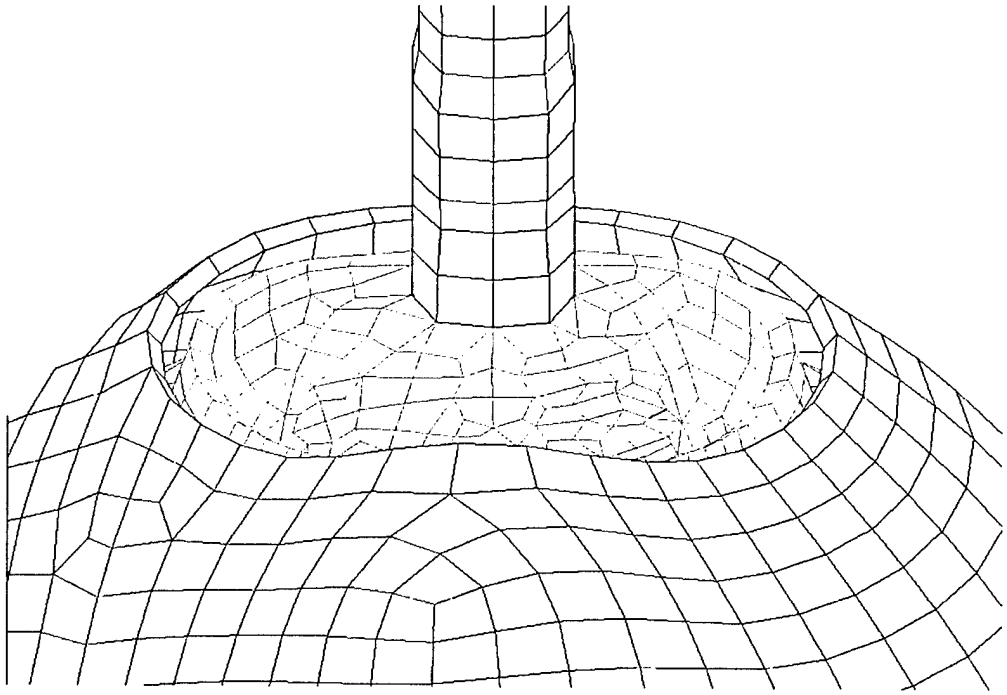

Figure 23. The fabric mesh has one 8-node hexagonal element through the 3.63-mm thickness and a typical in-plane element dimension of 10 mm.

## 4.2 Constitutive Modeling

A multi-ply Kevlar vest can be viewed as composed of a homogeneous orthotropic material. Its tensile stiffness and strength when pulled in-plane along the warp yarns are different than when pulled along the fill yarns. Moreover, its stiffness when pulled in-plane at 45° to both the warp and fill yarns is smaller than either its warp or fill direction stiffness because of a "scissoring" mechanism, whereby yarns rotate in the plane without much elongation (Hearle 1969). The fabric's transverse compressive stiffness is expected to differ markedly from its in-plane stiffnesses.

In-plane fabric stiffnesses along both warp and fill directions exhibit nonlinearity. Figure 24 is an idealized sketch of a typical stress-strain curve obtained from a quasi-static uniaxial tension test on a single ply of a plain-woven Kevlar fabric loaded along either the warp or fill direction (though the number would be different in the two cases). This curve includes a low-strain, relatively low-stiffness, region during which progressive uncrimping of the fabric yarns occurs (Grosberg 1969). Young's modulus in this first region is denoted $E_1$. This is followed by a larger stiffness region in which the yarns are fully uncrimped and the Young's modulus $E_2 > E_1$ applies. The strain corresponding to transition between these two regions is the locking strain, $\varepsilon_{lock}$. For plain-woven, 850-denier KM2, Johnson et al. (1999) presents the values $E_1$ = 7.4 GPa, $E_2$ = 74.0 GPa, $\varepsilon_{lock}$ = 0.025, and Poisson's ratio $v$ = 0.2. No indication is given of how this $v$ estimate

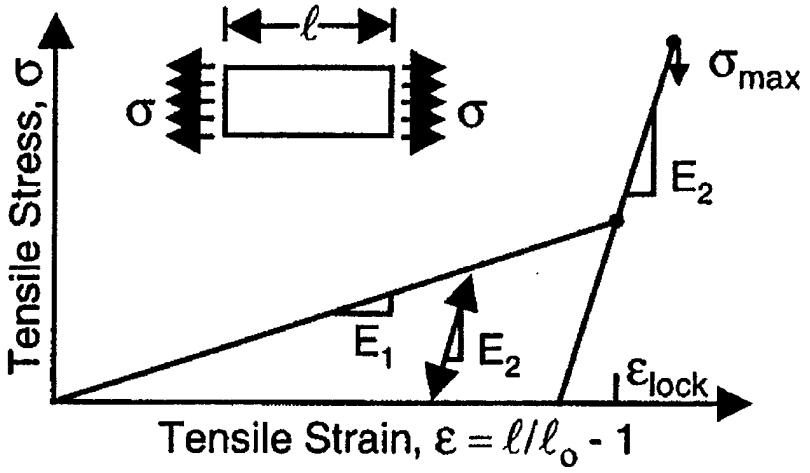


Source: Johnson et al. (1999), p. 964.

Figure 24. Sketch of a typical quasi-static uniaxial stress-strain curve for a single ply of Kevlar fabric.

was obtained, but its small value seems reasonable for this case of two orthogonal sets of yarns. Furthermore, no indication is given as to whether the values pertain to warp or fill direction.

Highly dynamic constitutive data have recently become available with the adaptation of the tensile split Hopkinson bar method applied to fabrics. Published results indicate that fabrics become stiffer under high rates of loading (Shim et al. 2001).

In the calculations in sections 7 and 8, the Kevlar KM2 vest is modeled as isotropic and linearly elastic. Its Young's modulus, $E$, is identified with the uncrimped modulus, $E_2$, of Johnson et al. (1999). This approach is analogous to that applied to most biomaterials in WSTM99. The values assigned to $E$, $v$, and initial density $\rho_0$ were obtained from Jackson et al. (1999) and are listed in Table 8.

Table 8. Constitutive properties for the KM2 vest.

| | |
|---|---|
| $E$ (GPa) | 74.0 |
| $\nu$ | 0.20 |
| $\rho_0$ (kg/m$^3$) | 1440 |

# 5. Modeling the 9-mm Remington Bullet

## 5.1 FE Mesh

The 9-mm Remington bullet drawing in Figure 25 was obtained from Olin Corporation. The bullet consisted of a lead core enclosed by a thin full-metal jacket composed of copper gilding. Since the fabric vest and WSTM99 are composed of elements with a typical edge length of 10 mm, the bullet was modeled with a single 8-node hexagonal element (Figure 26). Specifically, the bullet was a parallelepiped. Two sides, including the one that first struck the vest, were squares with the area of a 9-mm-diameter circle. The four sides orthogonal to these were rectangles with length determined so that, when the density of lead was assigned, the FE bullet model had a mass of 124 grains (gr), equal to the total mass of the physical bullet (lead plus gilding). The element was assigned the initial velocity of the bullet in test 524—425.5 m/s.

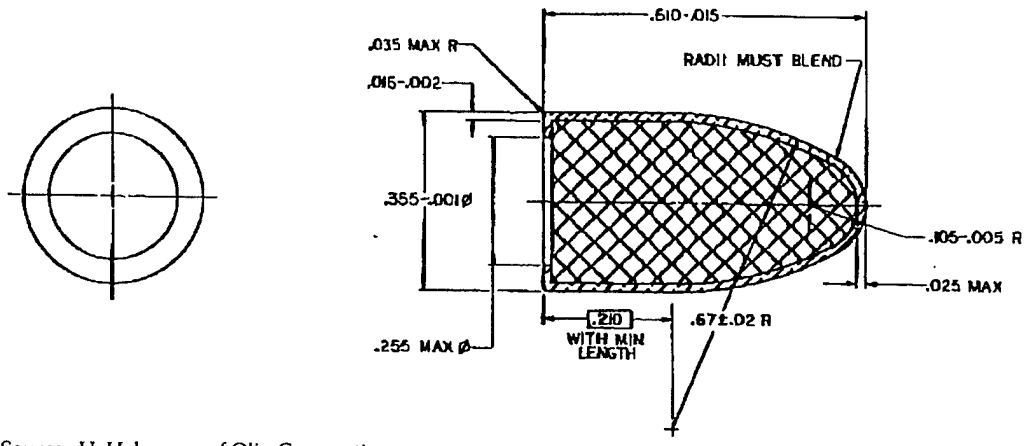


Source: H. Halverson of Olin Corporation.

Figure 25. Olin Corporation's drawing of the Remington 9-mm bullet.

This single element approach to modeling the bullet allows the amplitude of the initial stress wave delivered to the vest and thorax to be accurately mimicked. However, the subsequent deformation of the bullet was not accurately captured by a one-element representation. This limitation has a greater bearing on the late-time large-deflection stage of the problem than on the early-time wave stage. It is not clear during which phase life-threatening injuries to the heart, lungs, and liver are more likely to occur.

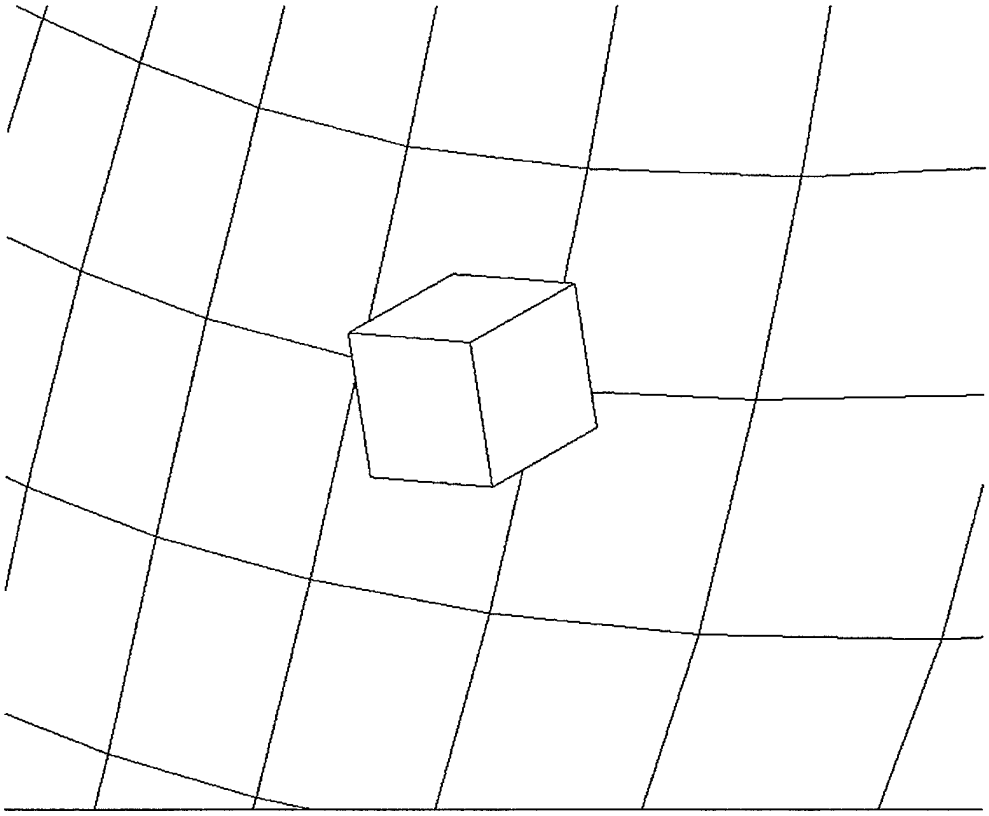

Figure 26. A single-element bullet strikes the vest at the mid-sternum location.

## 5.2 Constitutive Modeling

The bullet was assigned material properties of lead. Its dilatational motion was modeled with the Mie-Grüneison equation of state, according to which thermodynamic pressure, $P$, is related to compression, $\mu$, and internal energy per unit volume, $e$, by

$$P = \frac{\rho_0 C^2 \mu \left[ 1 + \mu \left( 1 - \frac{\gamma_0}{2} \right) \right]}{1 - \mu(S-1)} + \gamma_0 e \tag{3}$$

for compressed material and by

$$P = \rho_0 C^2 \mu + \gamma_0 e \tag{4}$$

for expanded material. Constants $C$ and $S$ are defined in terms of the features of the material's shock velocity-particle velocity curve, assumed to be linear. $C$ is the intercept of this curve, and $S$ is the slope. The Grüneison parameter is assumed to be a constant, $\gamma_0$. Compression is defined by

$$\mu = \frac{\rho - \rho_0}{\rho_0}, \tag{5}$$

where $\rho_0$ is initial density and $\rho$ is current density. The lead's specific heat at constant pressure, $c_p$, assumed to be a material constant, was used to compute temperature. Lead values for material constants $\rho_0$, $C$, $S$, $\gamma_0$, and $c_p$ were obtained from Kohn (1969) and are listed in Table 9.

Table 9. Material constants for the lead.

| | |
|---|---|
| $\rho_0$ (kg/m$^3$) | 11350 |
| $C$ (km/s) | 2.100 |
| $S$ (GPa) | 1.45 |
| $\gamma_0$ | 2.20 |
| $c_p$ (J/kg-K) | 12890. |
| $G$ (GPa) | 5.516 |
| $Y$ (GPa) | 0.03447 |

The lead's deviatoric behavior was modeled with isotropic, von Mises plasticity. Perfect plasticity was assumed, with the yield stress, $Y$, a constant, independent of strain, strain rate, and temperature. Prior to yield and during unloading, deviatoric behavior was governed by a constant elastic shear modulus, $G$. This shear modulus was also employed in the radial return algorithm. The values assigned to material constants $G$ and $Y$ were obtained from Johnson (1999) and given in Table 9. No damage model was applied to the lead.

# 6. Natick-AFIP-ATC Tests on Human Thoracic Tissue

## 6.1 Introduction

At the Armed Forces Institute of Pathology (AFIP), three tests were performed in which a 9-mm Remington bullet was fired at a velocity, $v$, of 425–448 m/s into a vest of multiple plain-woven plies of Kevlar KM2 worn by human thoracic tissue (Mackiewicz et al., to be published) (Table 10). The aim point was the center of the sternum. The tests were ethically approved by three institutional review boards.

The thoracic tissue was instrumented with Endevco accelerometers surgically implanted at four locations: (1) the lowest quarter of the posterior sternum, (2) the carina (bifurcation point) of the trachea, (3) the ligamentum arteriosum (a ligament that joins the aorta and the pulmonary trunk), and (4) the spinous process of the T7 vertebra. Figure 27 uses WSTM99 to illustrate these four

Table 10. Test impact speeds, cadaver ages, and Endevco Corporation accelerometer models.

| Test | $v$ (m/s) | Age (years) | Sternum | Trachea | Ligamentum Arteriosum | T7 Vertebra |
|---|---|---|---|---|---|---|
| 524 | 425.5 | 73 | 7264B-500 | 7265A | ND | 7265A |
| 678 | 448.1 | 85 | 7264A-2000 | 7265A | 7270A-20K | 7265A |
| 637 | 445.6 | 92 | 7270A-20K | 7265A | 7264B-500 | 7265A |

Note: ND = no data available.

locations. At each location, the gauge was sutured to the tissue. At the sternum and T7 vertebra, suturing involved the periosteum (De Maio 2001).

The accelerometer model numbers are given in Table 10 (De Maio and Parks 2001; Blethen 2001). The gauge characteristics, obtained from Endevco Corporation, are presented in Table 11. There were budget constraints on gauge selection, and there were no previously reported acceleration measurements of the trachea, ligamentum arteriosum, or sternum to serve as guidance. Of the three gauges, model 7265A, used on the trachea and T7 vertebra, had the smallest amplitude range and frequency range and the largest mass. At the sternum and ligamentum arteriosum, either model 7264B-500 or 7270A-20K was used, depending on the test. Of these, model 7270A-20K had the larger operating ranges for both frequency and amplitude, but it also had the larger mass. A sampling interval of 40 μs was used for model 7264B-500, and a sampling interval of 10 μs was used for the other models.

## 6.2 General Comments on Experimental Error

If the experimental data are to be used as "benchmarks" for the computations, it is important to be aware of limitations to the data. Furthermore, awareness of limitations revealed in these can lead to more accurate results in future tests. Six issues regarding the experimental accelerations are relevant:

(1) amplitude range limitations of the instrumentation,

(2) time response limitations of the instrumentation,

(3) additional temporal filtering and/or amplitude saturation imposed by electronics peripheral to the accelerometer,

(4) possible slippage of the accelerometer,

(5) impedance mismatch between the gauge and the surrounding thoracic media, and

(6) inertial loading on body parts from the instrumentation.

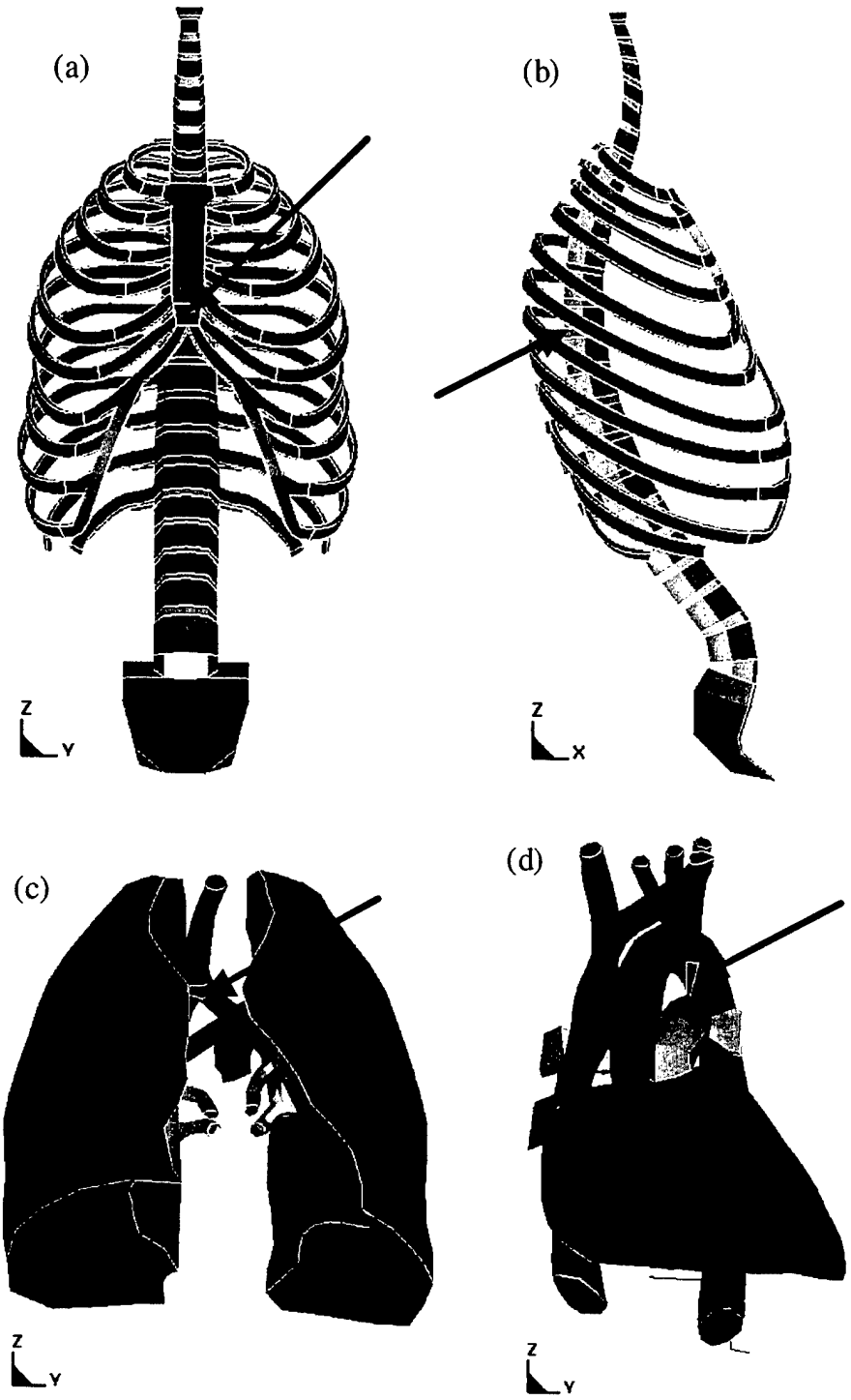


Figure 27. The four accelerometer locations: (a) lowest quarter of the posterior sternum, (b) spinous process of the T7 vertebra, (c) carina of the trachea, and (d) ligamentum arteriosum. Drawings show parts of WSTM99.

Table 11. Endevco Corporation accelerometer characteristics and sampling interval used for each.

| Model | Mass[a,b] (g) | Amplitude Range[b,c] (g's) | Frequency Range[b] (kHz) | Mounted Resonance Frequency[b] (kHz) | Period Corresponding to Frequency Range (μs) | Sampling Interval[d] (μs) |
|---|---|---|---|---|---|---|
| 7265A | 5 | ±100 | 0–0.8 | 2.7 | 1300 | 40 |
| 7264B-500 | 1 | ±500 | 0–3.0 | 17 | 330 | 10 |
| 7264A-2000 | 1 | ±2,000 | 0–4.0 | 25 | 250 | 10 |
| 7270A-20K | 1.5 | ±20,000 | 0–50 | 350 | 20 | 10 |

[a]Does not include mass of the cable.
[b]Source: Endevco Corporation (2001).
[c]±5% maximum, reference 100 Hz.
[d]Source: Blethen (2001).
Note: g's = gravitational acceleration.

The author was unable to obtain any information pertaining to issue (3). Regarding issue (4), autopsies following each test revealed no obvious signs of gauge slippage, i.e., the gauge appeared to be still sutured in place in every case for which data were reported (De Maio 2001).

Regarding, issue (5), the transmission and reflection of longitudinal and transverse stress waves at the sternum-gauge interface were governed by the characteristic impedances, $\rho c_L$ and $\rho c_T$, of the sternum and gauge (see Kolsky 1963, pp. 31–36). Unless these quantities for the gauge material matched those of the surrounding media in the thorax, stress-wave boundary conditions along the sternum-gauge interface were altered by the presence of the gauge. The same point applies at the trachea-gauge, ligamentum-gauge, and T7-gauge interfaces.

Issues (1), (2), and (6) are discussed in section 6.3 in the context of the four specific measurement locations.

## 6.3 Axial Acceleration Measurements

For each experimental signal to be shown in subsections 6.3.1 and 6.3.2, the time axis has been translated so that substantially non-zero values commence at time $t = 0$. For each experimental signal to be shown, axial accelerations are negative if in the same direction as the bullet's initial velocity vector and are positive if in the recoil direction. Each experimental signal was sampled at a time interval of either 10 or 40 μs depending on the gauge (see Table 10). However, in each instance the frequency response of the gauge caused additional low-pass filtering of the experimental signal.

### 6.3.1 Sternum

In the three tests, an accelerometer was sutured to the periosteum at the lowest quarter of the posterior side of the sternum (De Maio 2001). Figure 28 presents the experimental axial acceleration signals from the three tests, and Table 12 extracts the information from Tables 10 and 11 relevant to the sternum.

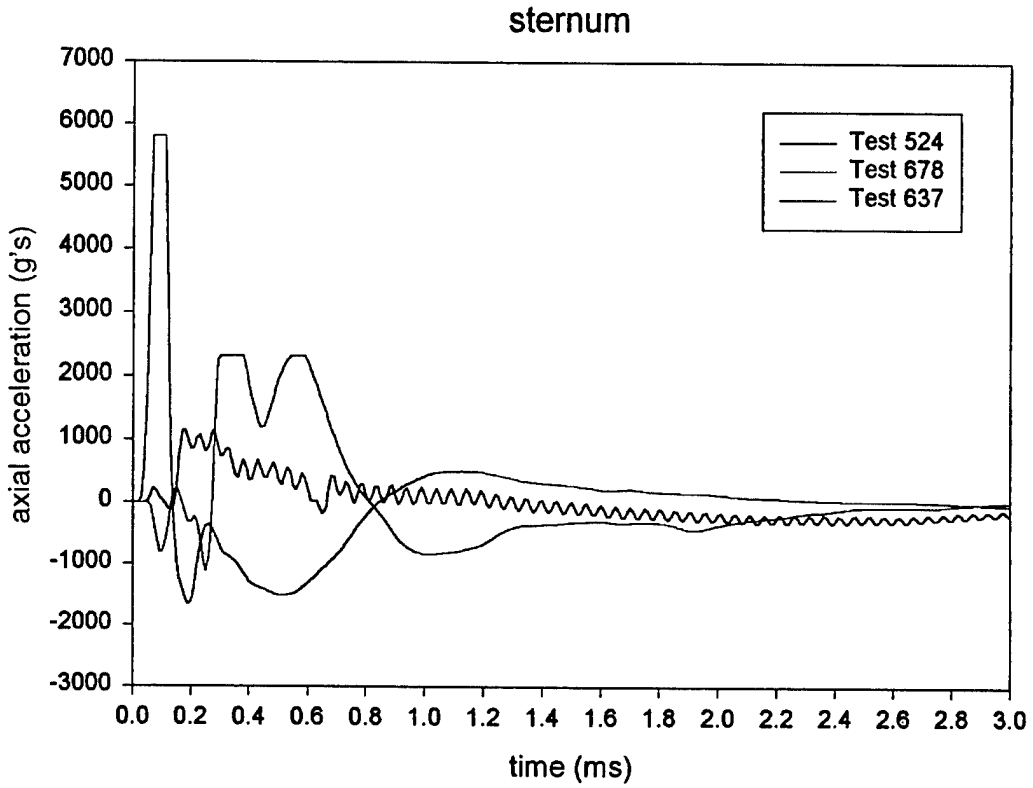


Figure 28. Axial accelerations measured on the posterior sternum vs. time from the three tests.

Table 12. Characteristics of the Endevco Corporation accelerometers attached to the lower posterior sternum in the three tests.

| Test | Endevco Gauge | Gauge Mass (g) | Gauge Amplitude Range (g's) | Gauge Frequency Range (kHz) | Mounted Resonance Frequency (kHz) | Period Corresponding to Frequency Range (μs) | Sampling Interval (μs) |
|---|---|---|---|---|---|---|---|
| 524 | 7264B-500 | 1 | ±500 | 0–3.0 | 17 | 330 | 10 |
| 678 | 7264A-2000 | 1 | ±2,000 | 0–4.0 | 25 | 250 | 10 |
| 637 | 7270A-20K | 1.5 | ±20,000 | 0–50 | 350 | 20 | 10 |

Note: Color coded to Figure 28.

A longitudinal wave analysis applied to the sternum as represented in WSTM99 can be used to estimate the desirable frequency response for the gauge. Upon frontal impact to the sternum, a longitudinal stress wave is introduced within the sternum. The thickness (dimension approximately aligned with the bullet's path and the gauge's axis) of Sternum in WSTM99 is 13 mm. Sternum in WSTM99 is composed of a homogeneous elastic material with properties representative of cortical bone, namely a Young's modulus, $E$, of 11.51 GPa, and an initial density, $\rho_0$, is 2.0 g/cm$^3$ (Table 2). The corresponding longitudinal wave speed, $c_L$, is 2.8 mm/μs. Hence, round-trip transit times for a longitudinal wave along the thickness is 9.3 μs. The corresponding frequencies is 110 kHz. This is also the lowest natural frequency once rigid body motion is discarded for longitudinal free vibrations of Sternum assuming that both surfaces are free. If once accepts the preceding wave analysis, then gauge 7264B-500 and even gauge 7270A-20K appear inadequate to resolve longitudinal waves in the through-thickness direction. A caveat is that Sternum in WSTM99 is a simplication of the physical anatomy, as discussed in section 3.1, issue (4).

The test 678 signal in Figure 28 show slight clipping at 2300 g, which is consistent with the gauge's amplitude range of ±2000 g's. The test 524 signal in Figure 28 exceeds the gauge's amplitude range of ±500 g's, and the evident 20 kHz oscillation corresponds to the gauge's mounted mechanical resonance frequency.

The Endevco 7264B-500, 7264A-2000, and 7270A-20K gauges have masses of 1, 1, and 1.5 g, respectively. These masses seem sufficiently small relative to the 80-g approximate total mass of the sternum. This estimate of 80 g is based on the total mass of the 28 elements that constitute Sternum in WSTM99.

Endevco 7264B-500 and Endevco 7264A-2000 should not be used for future sternum acceleration measurements. This assessment is based on amplitude and frequency limitations in the first case and at a minimum amplitude limitations in the second case. Endevco 7270A-20K is better but should ideally be replaced with a gauge that has an operating frequency range of 0 to at least 110 kHz.

### 6.3.2 Trachea

In the three tests, an accelerometer was sutured to the anterior surface of the carina (bifurcation point) of the trachea (De Maio 2001). Figure 29 shows the tracheal acceleration data, and Table 13 collects information applicable to the Trachea from Tables 10 and 11.

Endevco gauge 7265A was used in each of tests 524, 678, and 637. This gauge's operating frequency range of 0–0.8 kHz was only marginally adequate for the experimental signal from test 637 and was slightly exceeded by the signals from tests 524 and 678. The signal from test 637 displays amplitude saturation at 100 g's, which is expected based on the gauge's characteristics. The signal from test 678 saturates at a somewhat smaller amplitude of 29 g's. The signal from

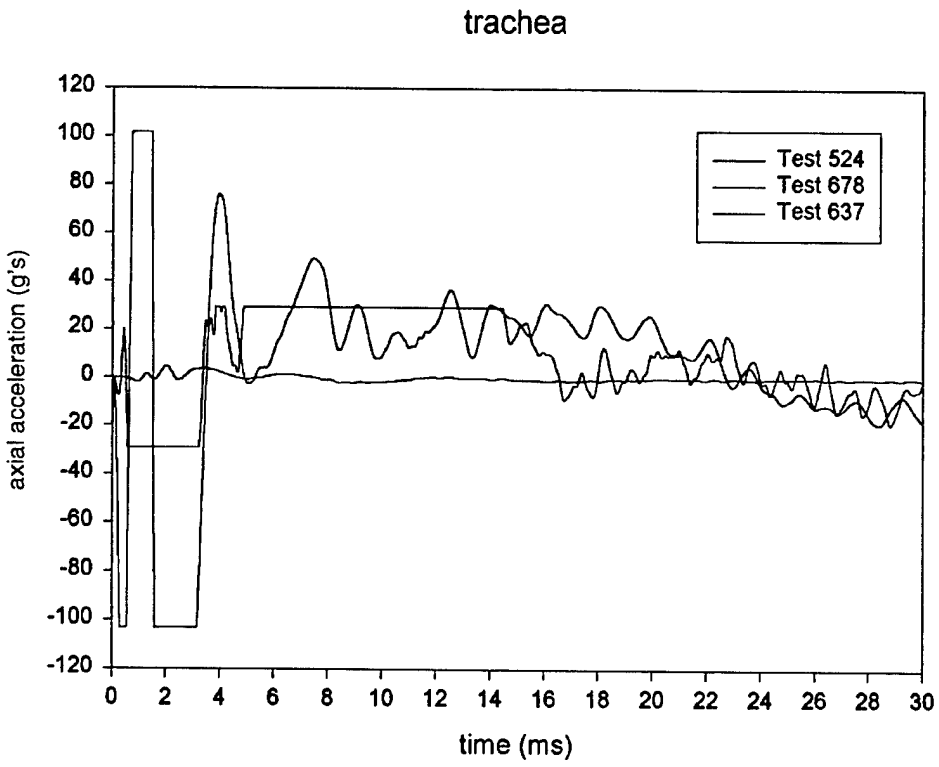


Figure 29. Axial accelerations measured at the carina of the trachea vs. time from the three tests.

Table 13. Characteristics of the Endevco Corporation accelerometers attached to the carina of the trachea in the three tests.

| Test | Endevco Gauge | Gauge Mass (g) | Gauge Amplitude Range (g's) | Gauge Frequency Range (kHz) | Mounted Resonance Frequency (kHz) | Period Corresponding to Frequency Range (ms) | Sampling Interval (μs) |
|---|---|---|---|---|---|---|---|
| 524 | 7265A | 5 | ±100 | 0–0.8 | 2.7 | 1.3 | 40 |
| 678 | 7265A | 5 | ±100 | 0–0.8 | 2.7 | 1.3 | 40 |
| 637 | 7265A | 5 | ±100 | 0–0.8 | 2.7 | 1.3 | 40 |

Note: Color coded to Figure 29.

test 524 displays amplitudes that are curiously smaller than those from tests 678 and 637 and suspiciously smaller than accelerations measured at the posterior sternum a short distance away. Perhaps the gauge in test 524 slipped relative to the trachea. The Endevco 7265A gauge has a mass of 5 g, 8% of the 62-g total mass of all elements that constitute Trachea in WSTM99. Figure use of Endevco 7265A for carina acceleration can be ruled out based on amplitude response and frequency response.

### 6.3.3 Ligamentum Arteriosum

In the tests, an accelerometer was sutured to the ligamentum arteriosum, near its connection with the aorta (De Maio 2001). No data were obtained from test 524. Figure 30 plots acceleration data from tests 678 and 637. Gauge characteristics for these tests are collected in Table 14.

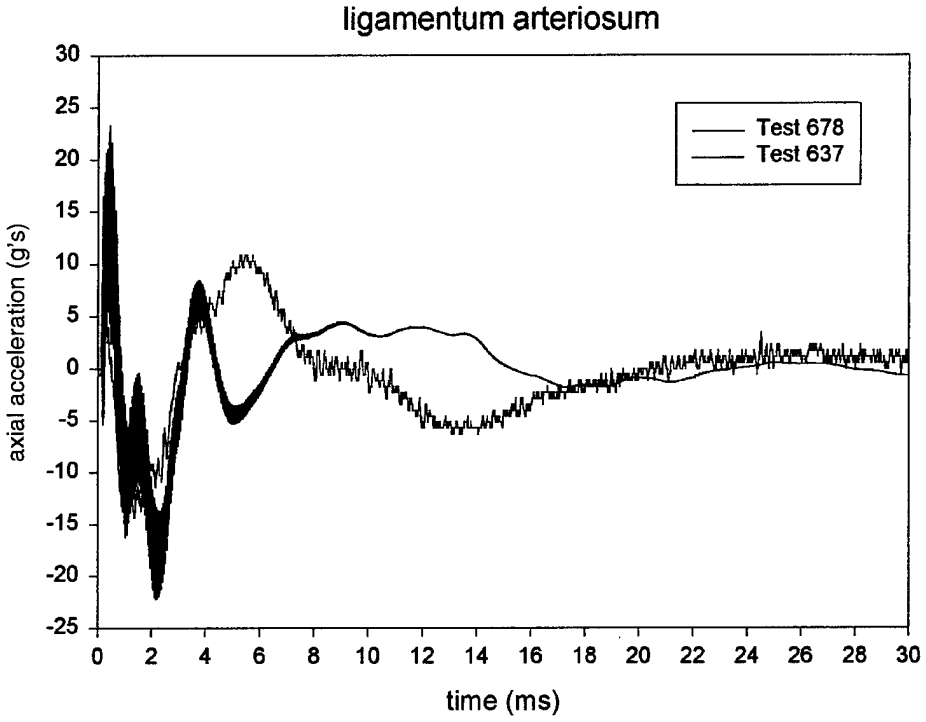


Figure 30. Axial accelerations measured on the ligamentum arteriosum vs. time from two tests.

Table 14. Characteristics of the Endevco Corporation accelerometers attached to the ligamentum arteriosum in two tests.

| Test | Endevco Gauge | Gauge Mass (g) | Gauge Amplitude Range (g's) | Gauge Frequency Range (kHz) | Mounted Resonance Frequency (kHz) | Period Corresponding to Frequency Range (μs) | Sampling Interval (μs) |
|---|---|---|---|---|---|---|---|
| 678 | 7270A-20K | 1.5 | ±20,000 | 0–50 | 350 | 20 | 10 |
| 637 | 7264B-500 | 1 | ±500 | 0–3.0 | 17 | 330 | 10 |

Note: Color coded to Figure 30.

Endevco 7264B-500 exhibits the same phenomenon that it did on the sternum in Figure 28, 20-kHz oscillations that are almost certainly spurious and associated with mechanical resonance of the gauge.

In WSTM99, the four elements that constitute Ligamentum Arteriosum have a combined mass of only 3 g. The 1.5-g mass of the Endevco 7270A-20K is therefore a concern. However, the effective mass of the ligamentum arteriosum must include contributions from the large connected arteries, namely the aorta and the pulmonary trunk (Parks 2001). Adequacy of the Endevco 7270A-20K for ligamentum arteriosum acceleration cannot be ruled out.

### 6.3.4 T7 Vertebra

In the tests, an accelerometer was sutured to the periosteum covering the spinous process of the T7 vertebra (De Maio 2001). An Endevco 7265A gauge was used in all three tests. Figure 31 plots the acceleration data vs. time, and Table 15 collects 7265A characteristics.

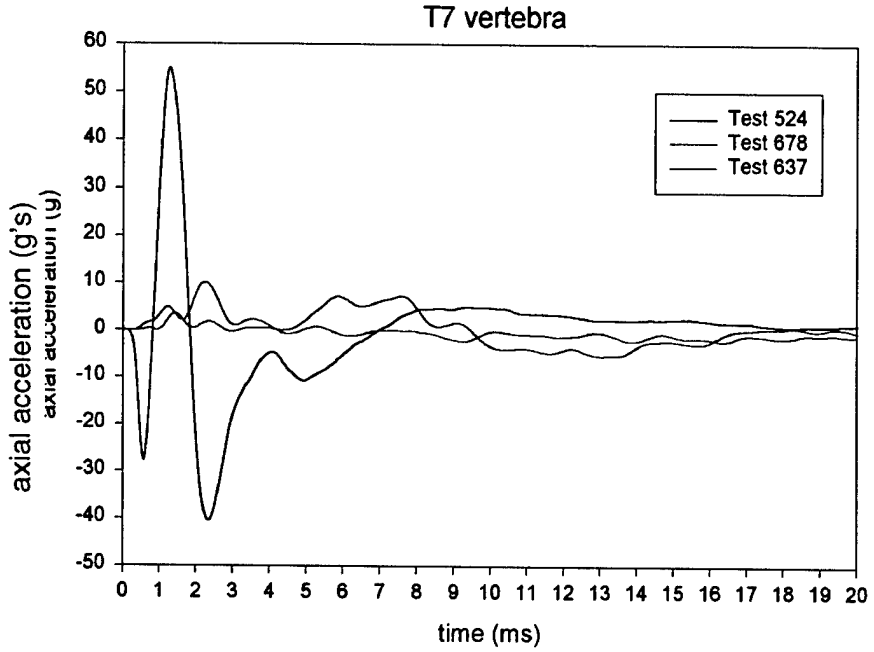


Figure 31. Axial accelerations measured on the spinous process of the T7 vertebra vs. time from the three tests.

Table 15. Characteristics of the Endevco Corporation accelerometers attached to the spinous process of the T7 vertebra in the three tests.

| Test | Endevco Gauge | Gauge Mass (g) | Gauge Amplitude Range (g's) | Gauge Frequency Range (kHz) | Mounted Resonance Frequency (kHz) | Period Corresponding to Frequency Range (ms) | Sampling Interval (μs) |
|---|---|---|---|---|---|---|---|
| 524 | 7265A | 5 | ±100 | 0–0.8 | 2.7 | 1.3 | 40 |
| 678 | 7265A | 5 | ±100 | 0–0.8 | 2.7 | 1.3 | 40 |
| 637 | 7265A | 5 | ±100 | 0–0.8 | 2.7 | 1.3 | 40 |

Note: Color coded to Figure 31.

Amplitude saturation in the experimental signals does not appear to have occurred in Figure 31. However, the gauge's frequency range is only marginally adequate for the signals seen in this figure. Higher frequency components may well have been discarded by the gauge.

In WSTM99, the total mass of the elements that comprise Thoracic Vertebrae is 802 g. Averaging this evenly over the 11 vertebrae included in the part gives a mass per vertebra of 73 g. The mass of Endevco 7265A is 5 g, or 7% of this value.

Adequacy of Endevco 7265A for T7 acceleration can be ruled out based on its frequency response.

## 7. Computational Results for Axial Velocity Contours

Figures 32–46 present axial velocity contours at successive times after initial bullet-vest impact from the LS-DYNA solution. The axial direction is associated with the initial path of the bullet. Axial velocities are negative if in the same direction as the bullet's initial velocity vector. Fringe levels are in meters per second. Note that the fringe levels peak at ±1 m/s. This sensitive scale was chosen to detect wave arrival times and because a 1 m/s velocity, though a small fraction of the bullet's impact speed of 425.5 m/s, seems significant in terms of potential injury. Figures 32–36 are two-dimensional (2-D) drawings of the medial cross section of WSTM99, the vest, and the bullet. Note that only the midsurface is drawn for parts meshed with shell elements. Figures 37–46 are three-dimensional (3-D) drawings of the skeletal parts in isolation. Figures 37–41 view these parts from an anterior location, and Figures 42–46 view them from a posterior location.

During the first 400 μs after impact, a region of axial acceleration in the direction of the bullet's initial velocity can be seen to spread across the sternum from the hit location (Figures 33–35 and 37–40). At 500 μs, elastic recoil in the central portion of the sternum has occurred (Figures 35 and 40). At 2.5 ms, much of the sternum is moving with an axial velocity opposite in direction to that of the bullet initially (Figures 36 and 41).

Motion reaches the spine surprisingly quickly. By 15 μs after initial impact of the vest by the bullet, the T4 vertebra has undergone appreciable acceleration, as shown by a small blue region (Figure 42). The fourth rib, which terminates on the T4 vertebra and contacts the sternum at a point closer to the aim point then does any other rib, presumably provided the path for the velocity wave to reach the T4 vertebra. However, the contour plots in Figures 37 and 42 do not clearly visualize such a wave and a compact-bone longitudinal wave speed of 2.8 mm/μs (Table 1) means a wave front displacement in 15 μs of only 42 mm. Hence, the observation of substantial T4 motion at 15 μs is not fully understood.

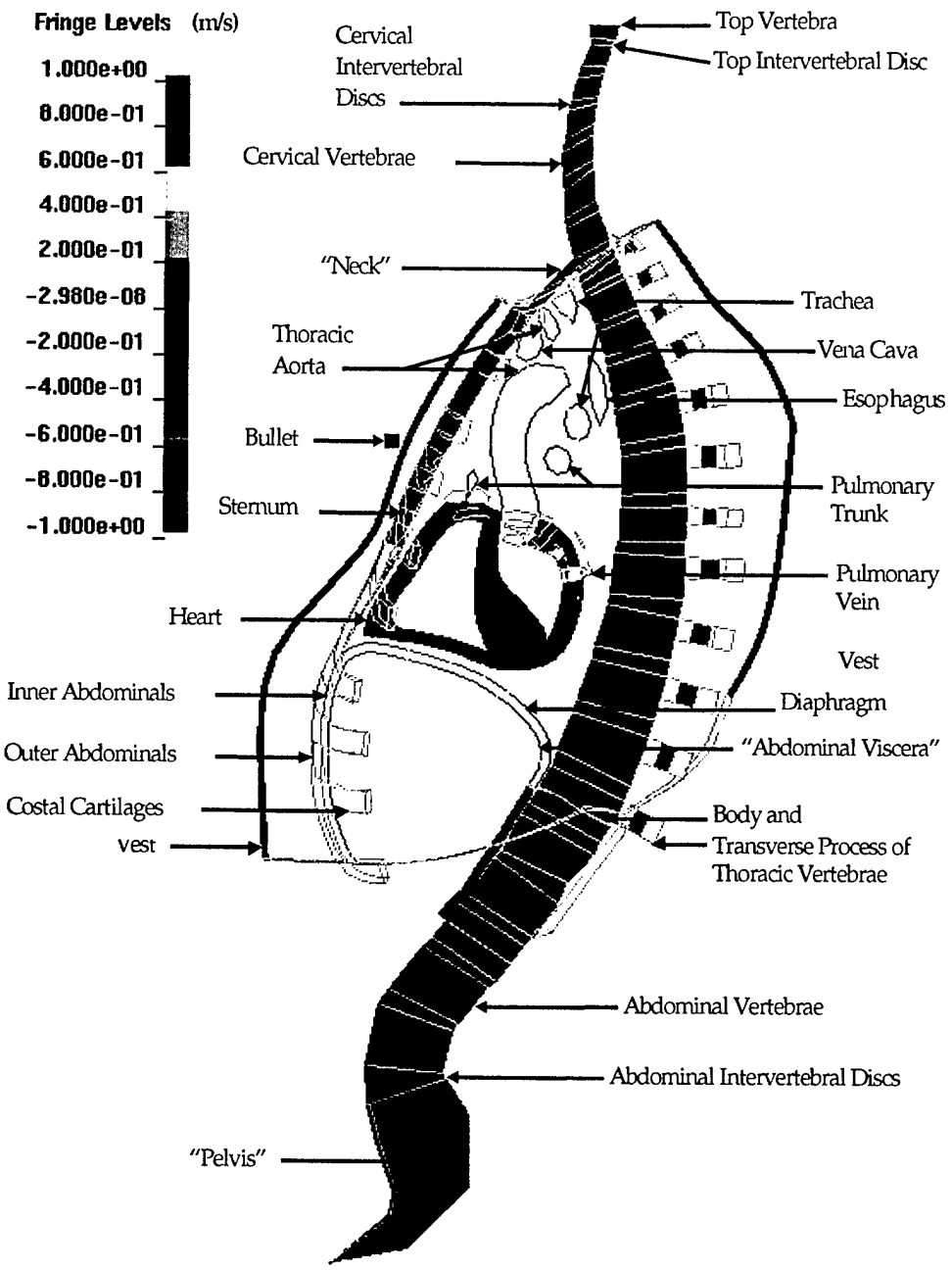


Figure 32. Medial cross sections of WSTM99, the vest, and the bullet showing initial axial velocity contours at the instant that the bullet impacts the vest (time $t = 0$).

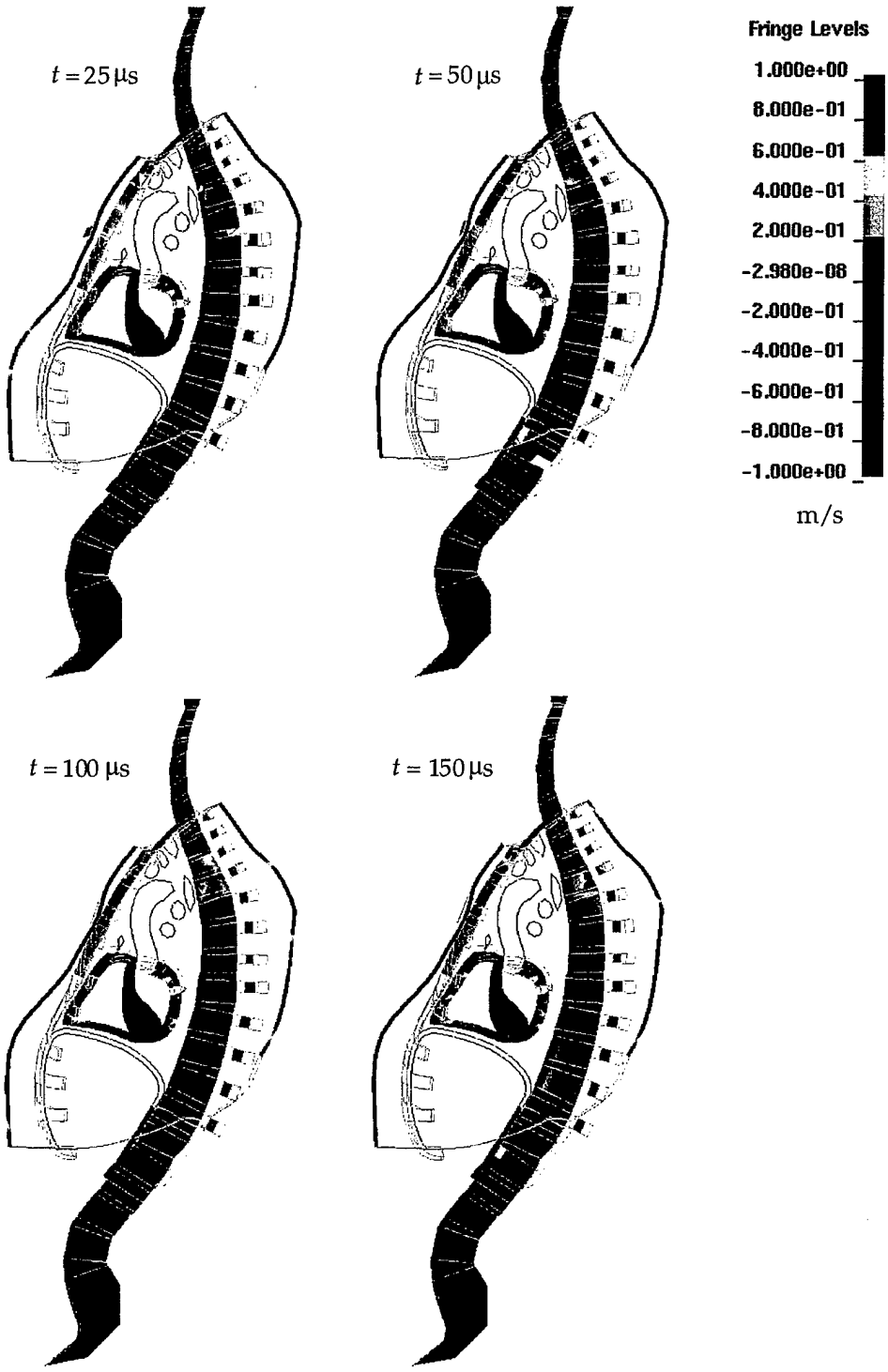


Figure 33. Medial cross sections of WSTM99, the vest, and the bullet showing computed axial velocity contours at 25, 50, 100, and 150 μs after initial impact.

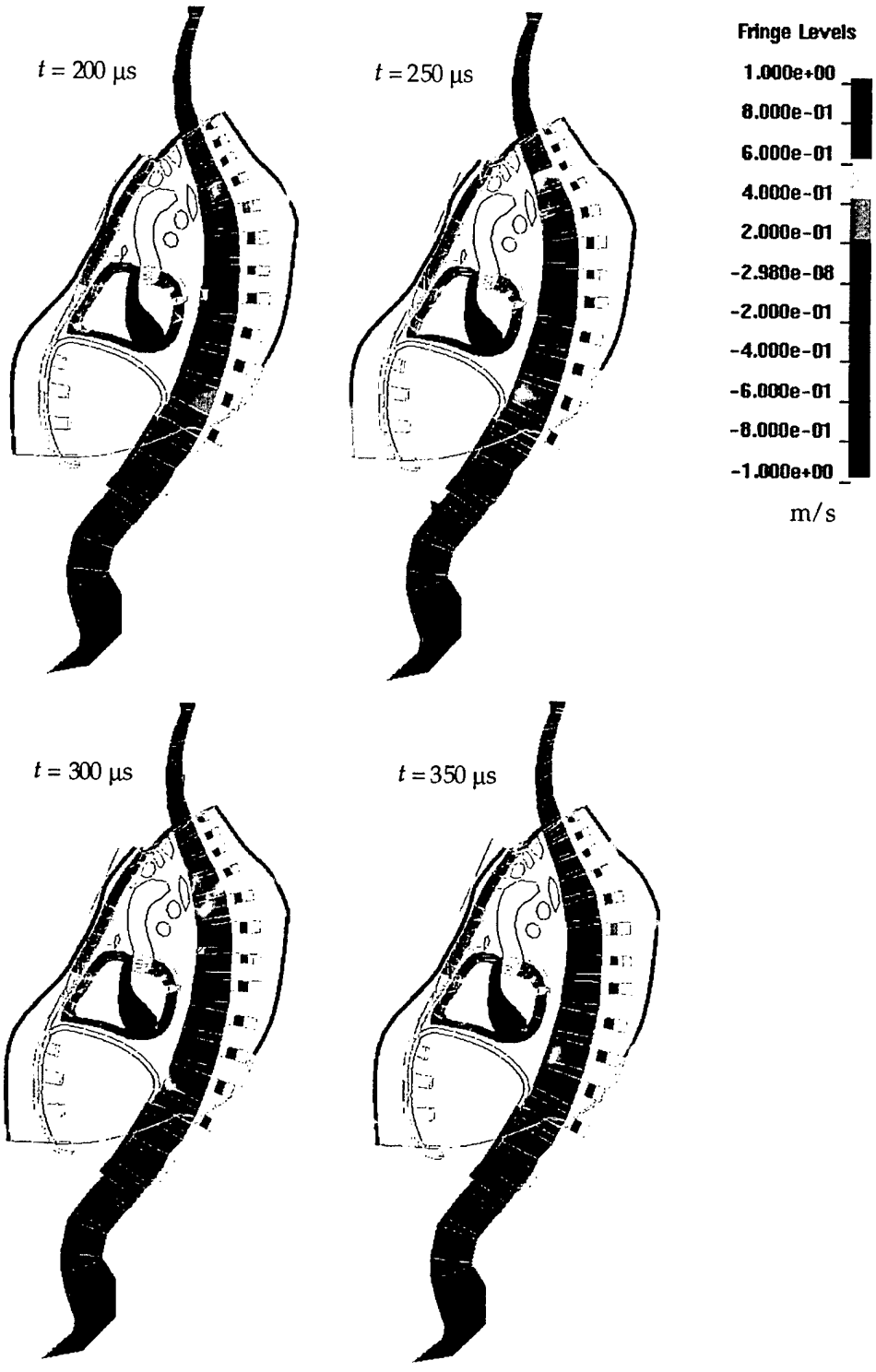


Figure 34. Medial cross sections of WSTM99, the vest, and the bullet showing computed axial velocity contours at 200, 250, 300, and 350 μs after initial impact.

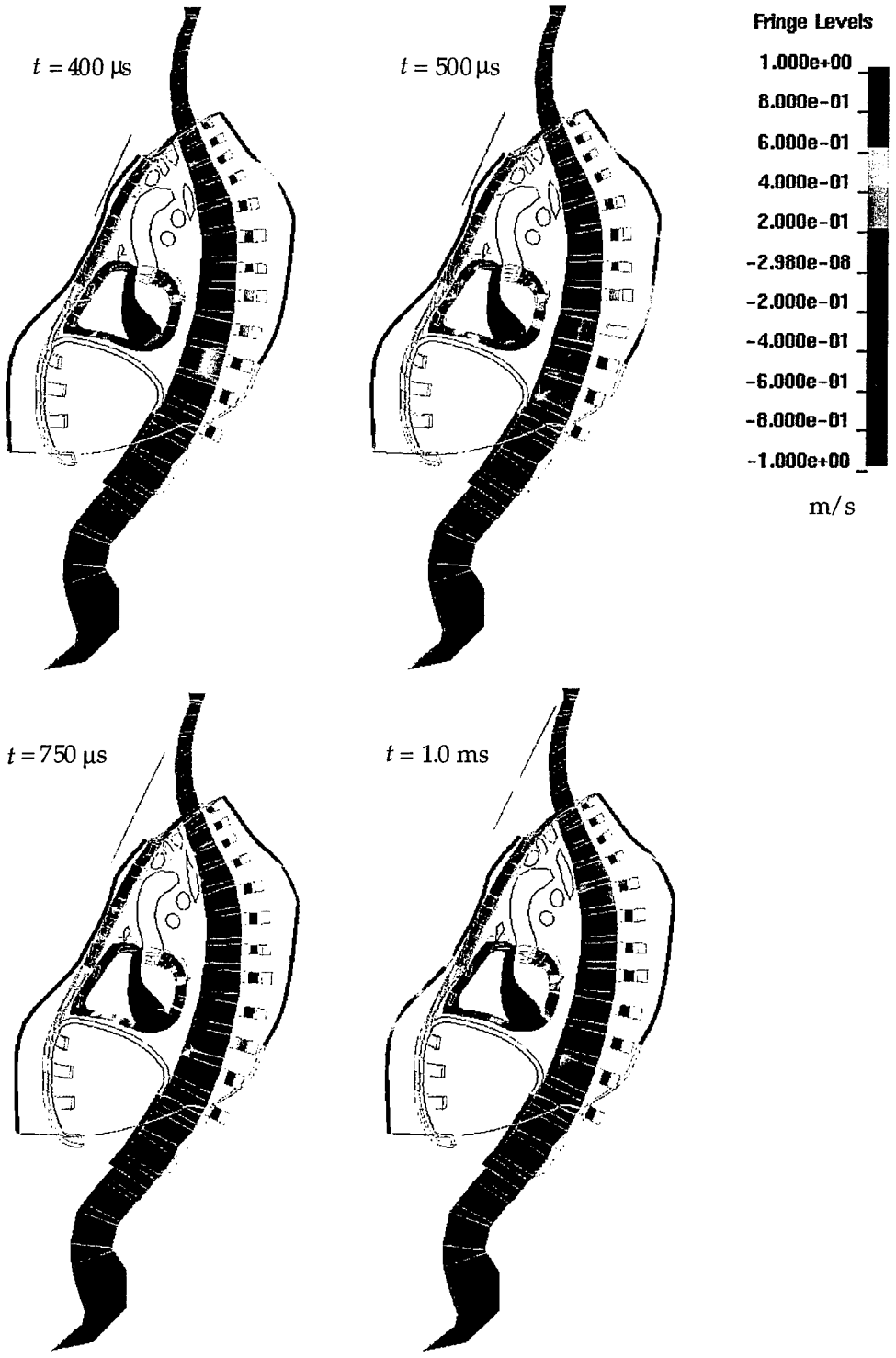


Figure 35. Medial cross sections of WSTM99, the vest, and the bullet showing computed axial velocity contours at 400 μs, 500 μs, 750 μs, and 1.0 ms after initial impact.

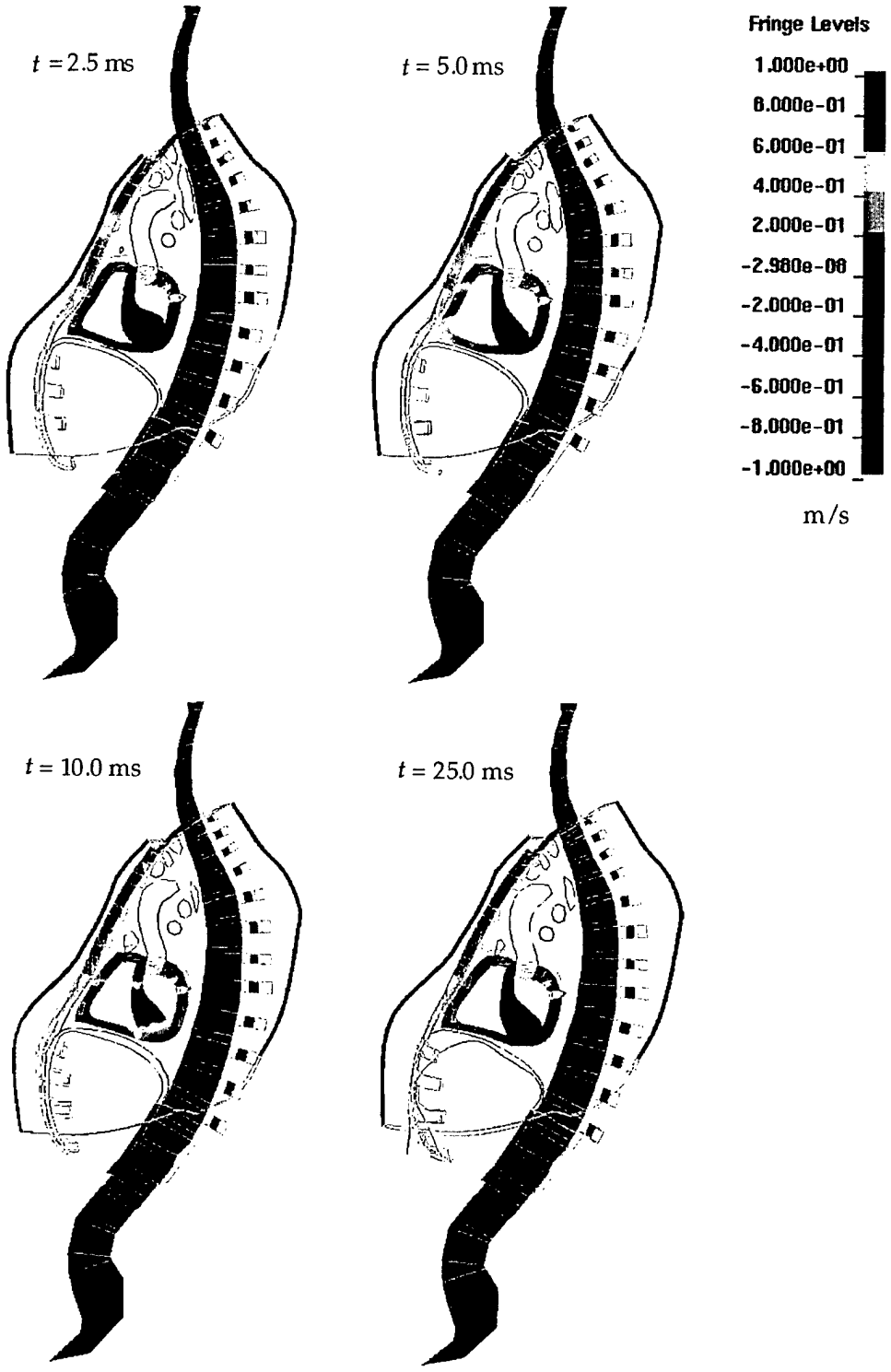


Figure 36. Medial cross sections of WSTM99, the vest, and the bullet showing computed axial velocity contours at 2.5, 5.0, 10.0, and 25.0 ms after initial impact.

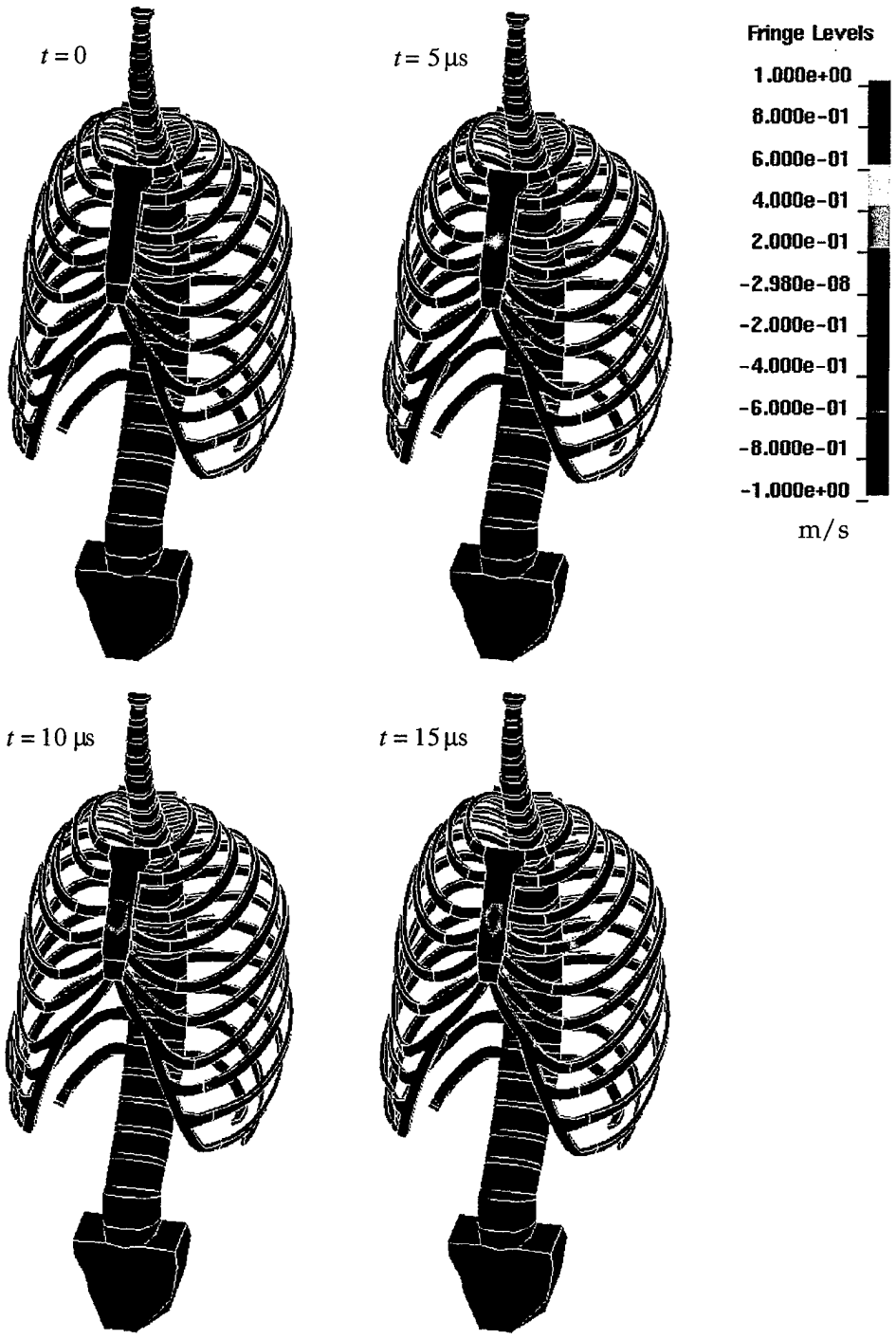


Figure 37. Anterior view of WSTM99 skeletal parts showing computed axial velocity contours initially and at 5, 10, and 15 μs after initial impact of the bullet and vest.

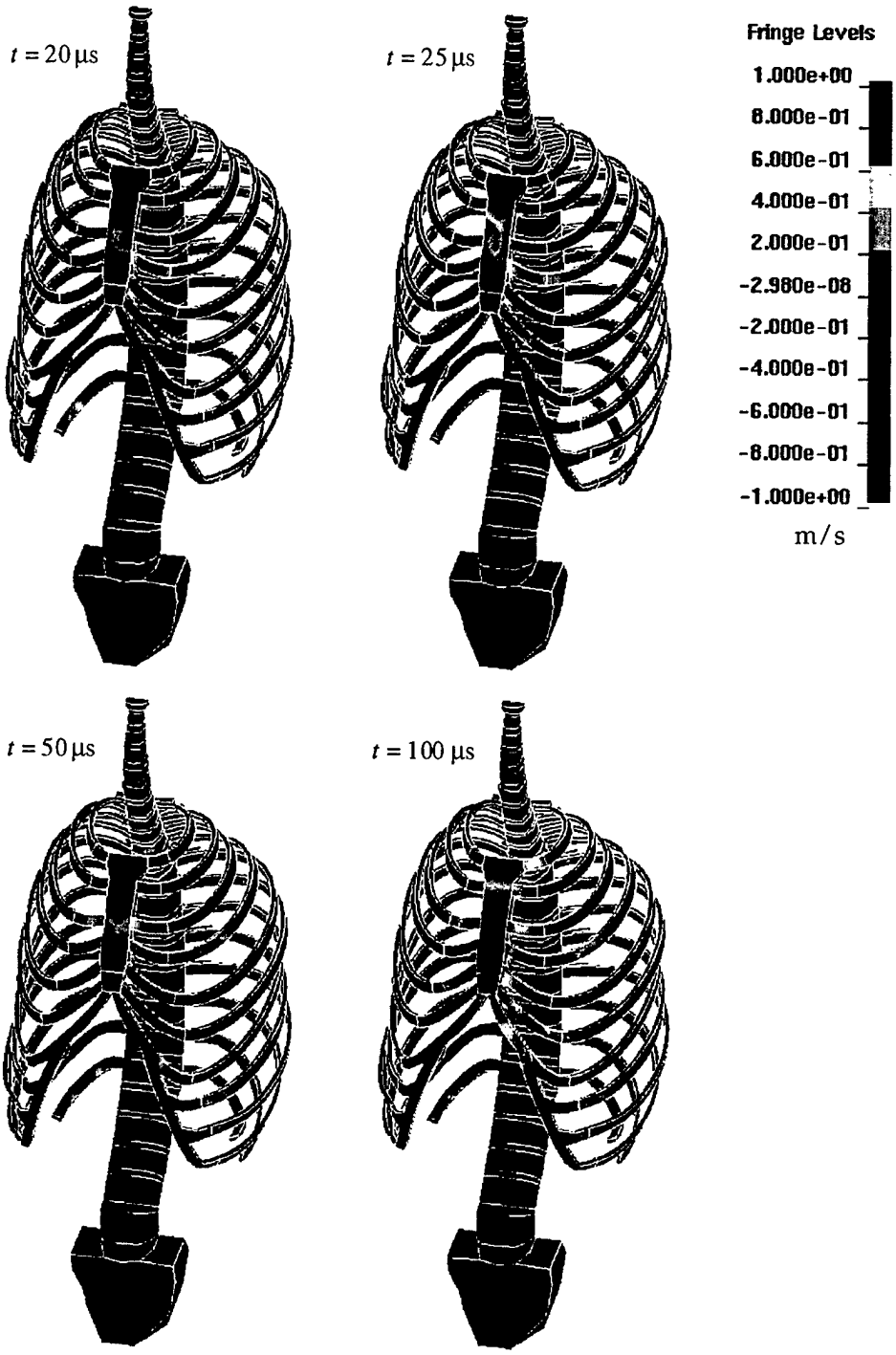


Figure 38. Anterior view of WSTM99 skeletal parts showing computed axial velocity contours at 20, 25, 50, and 100 μs after initial impact of the bullet and vest.

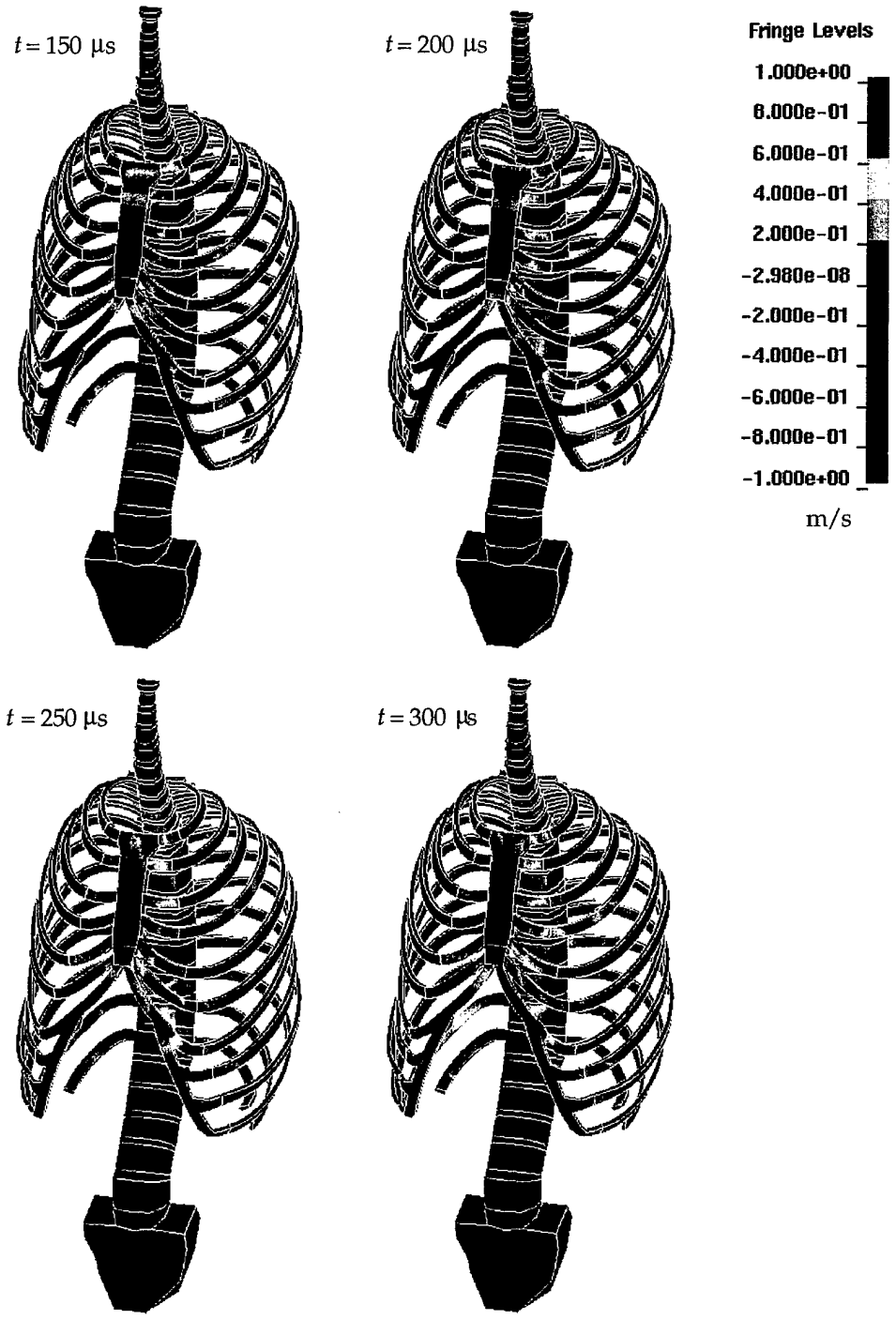


Figure 39. Anterior view of WSTM99 skeletal parts showing computed axial velocity contours at 150, 200, 250, and 300 μs after initial impact of the bullet and vest.

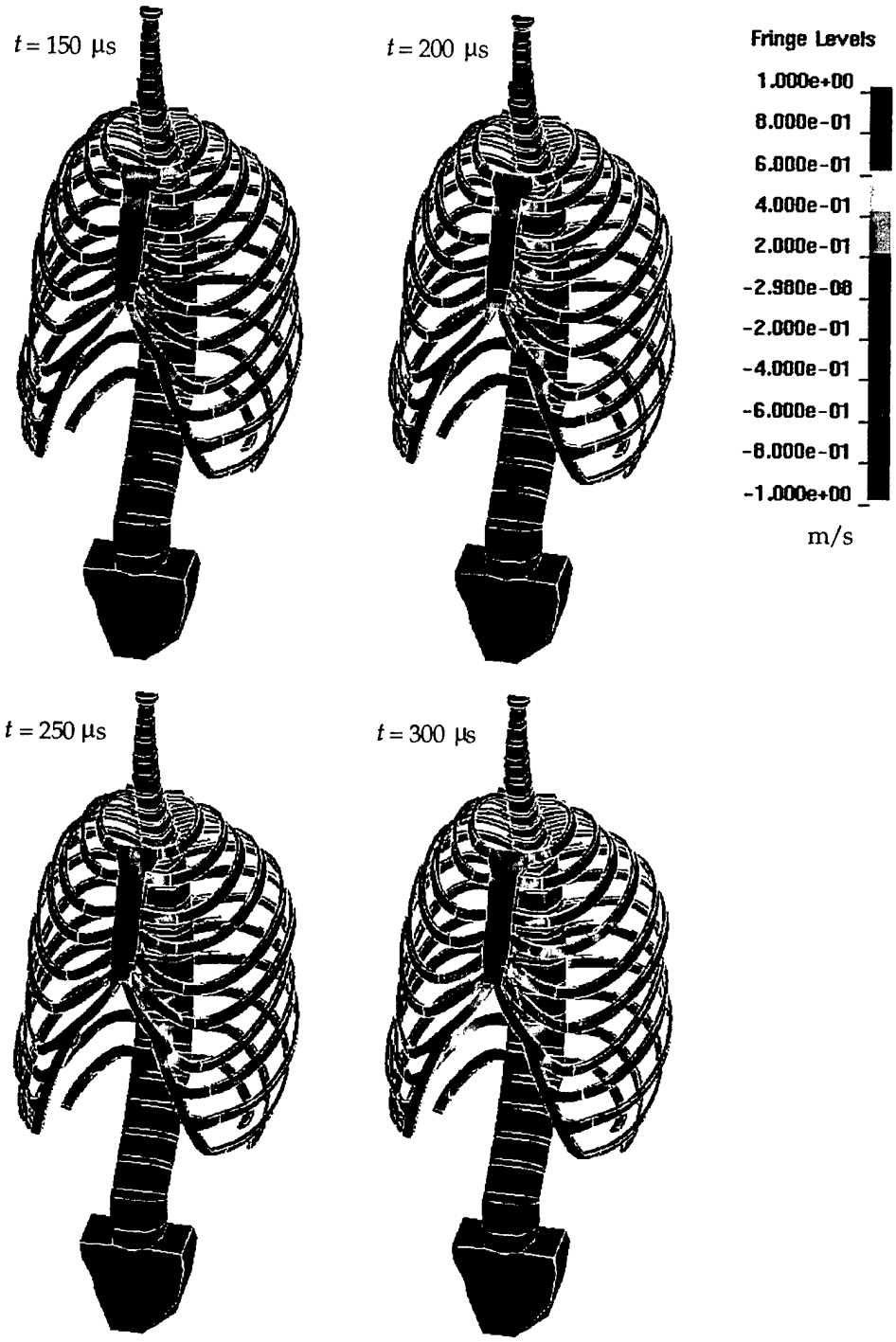


Figure 40. Anterior view of WSTM99 skeletal parts showing computed axial velocity contours at 350, 400, 500, and 750 μs after initial impact of the bullet and vest.

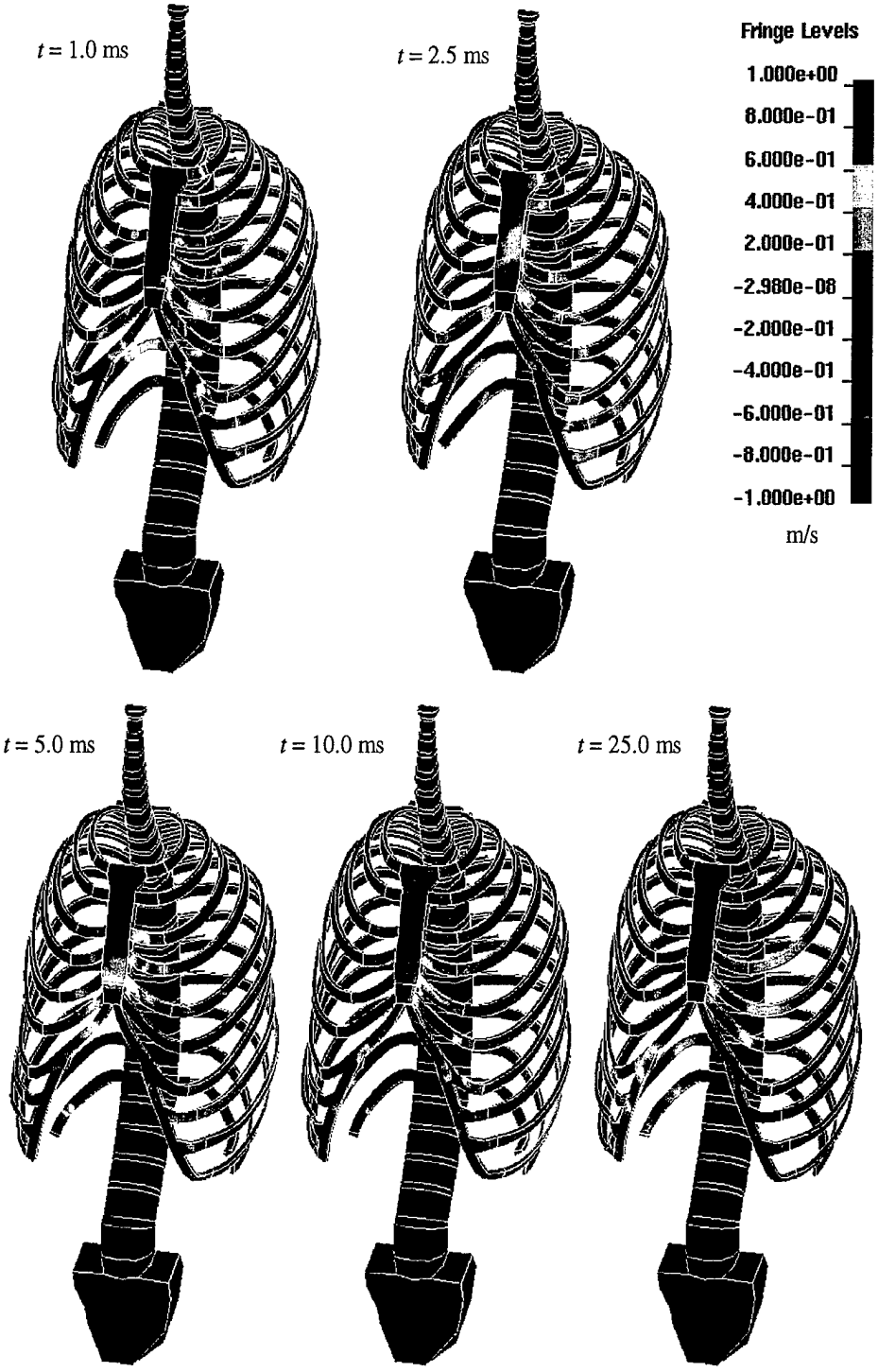


Figure 41. Anterior view of WSTM99 skeletal parts showing computed axial velocity contours at 1.0, 2.5, 5.0, 10.0, and 25.0 ms after initial impact of the bullet and vest.

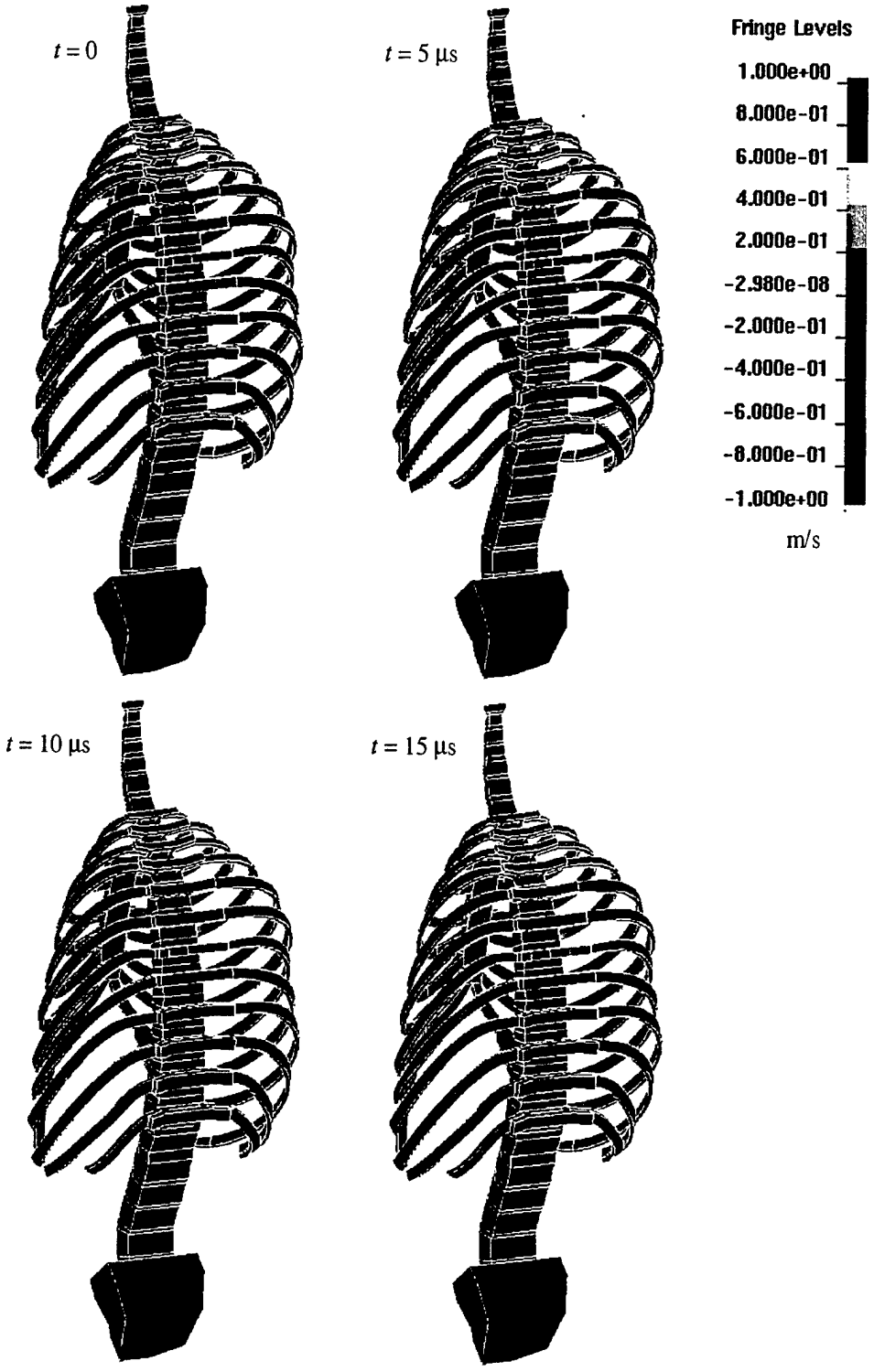


Figure 42. Posterior view of WSTM99 skeletal parts showing computed axial velocity contours initially and at 5, 10, and 15 μs after initial impact of the bullet and vest.

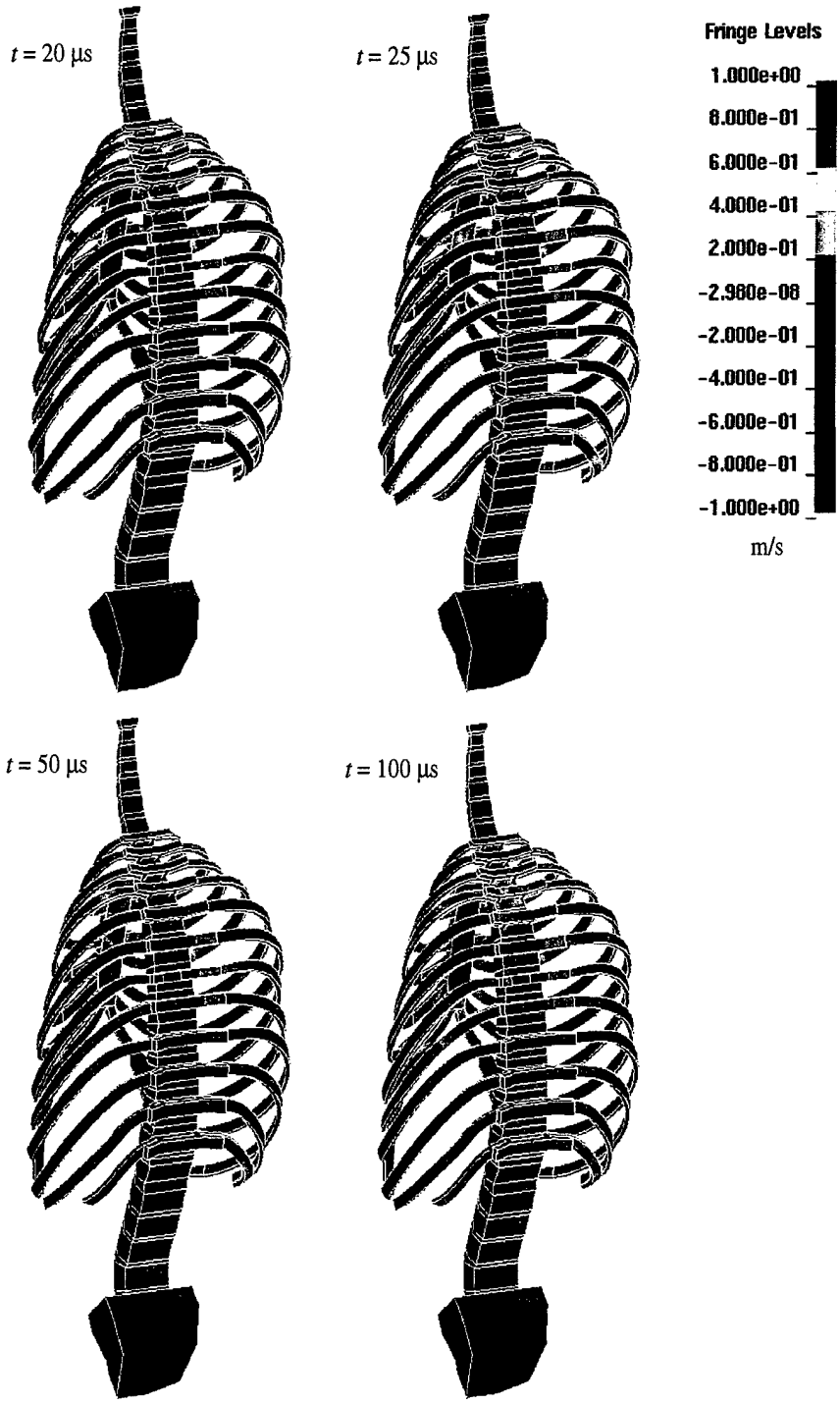


Figure 43. Posterior view of WSTM99 skeletal parts showing computed axial velocity contours at 20, 25, 50, and 100 μs after initial impact of the bullet and vest.

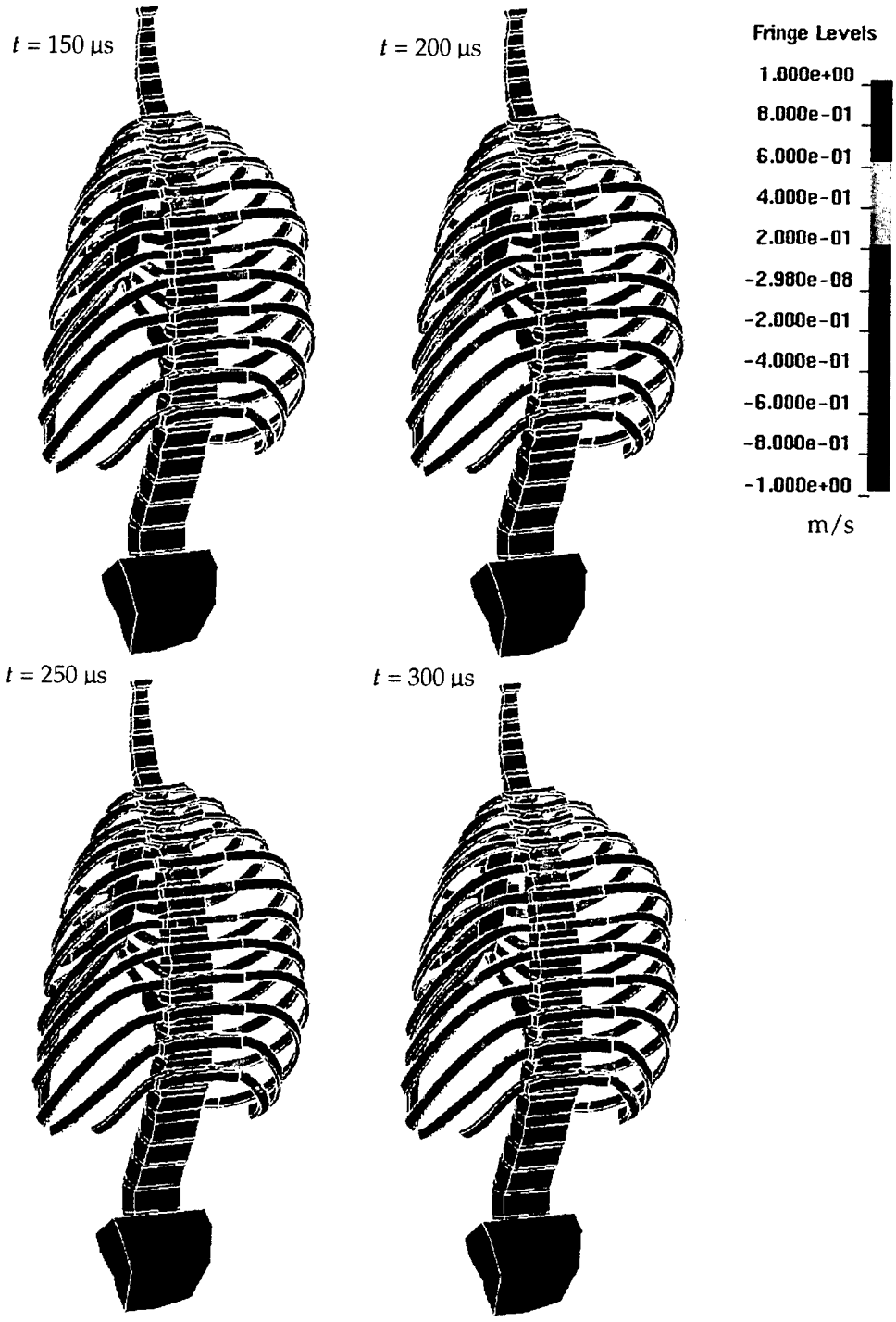


Figure 44. Posterior view of WSTM99 skeletal parts showing computed axial velocity contours at 150, 200, 250, and 300 μs after initial impact of the bullet and vest.

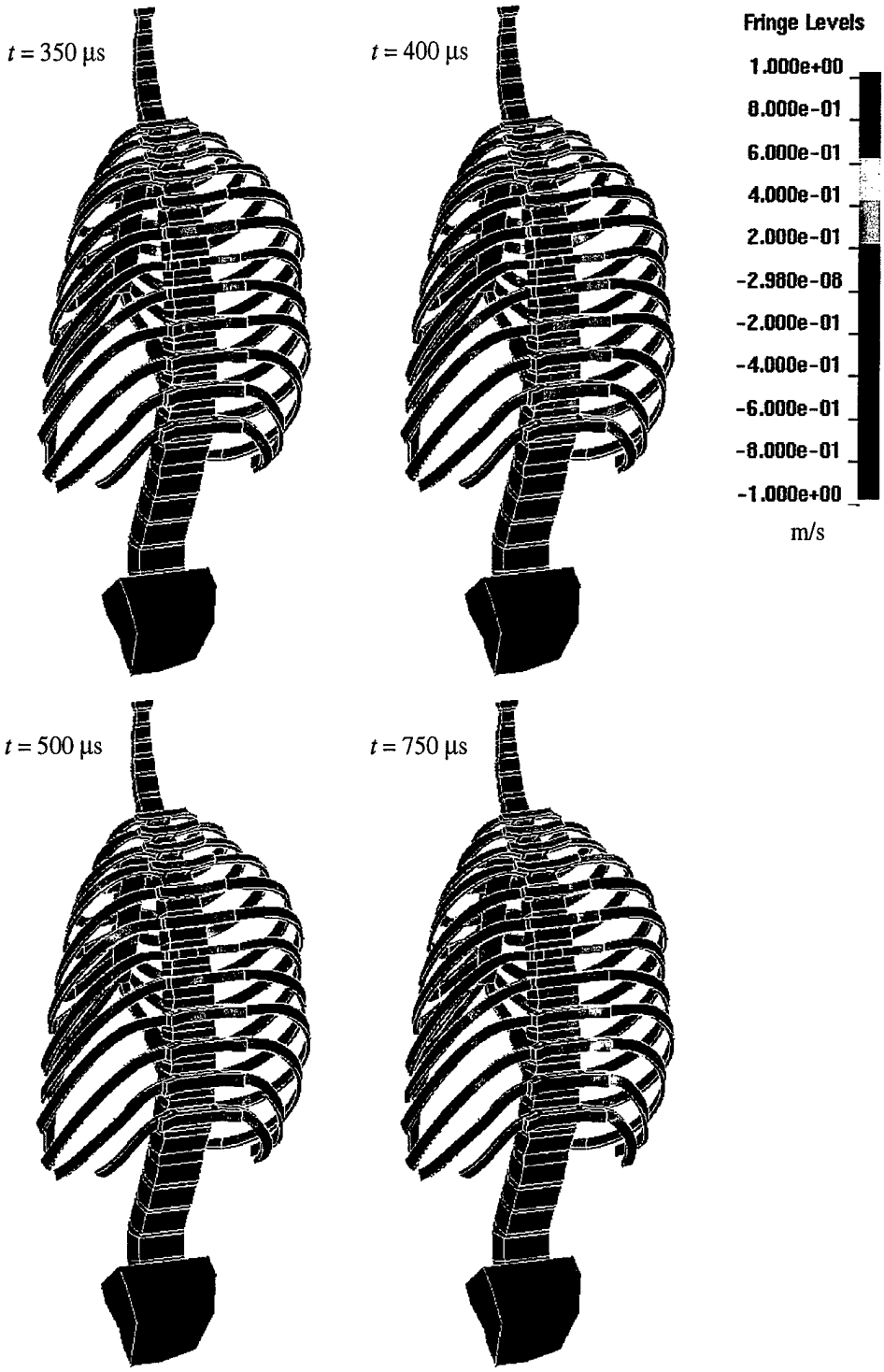


Figure 45. Posterior view of WSTM99 skeletal parts showing computed axial velocity contours at 350, 400, 500, and 750 μs after initial impact of the bullet and vest.

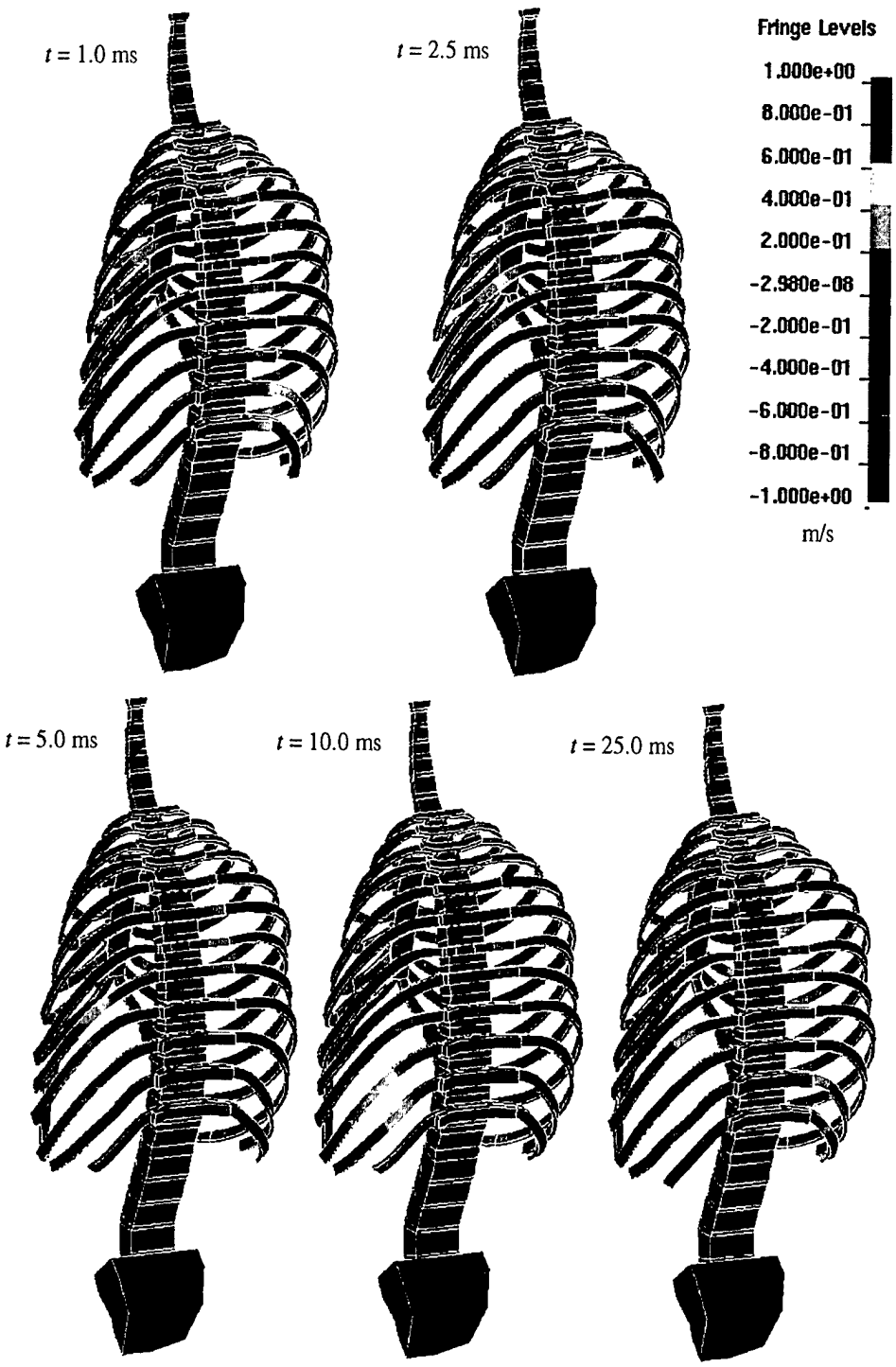


Figure 46. Posterior view of WSTM99 skeletal parts showing computed axial velocity contours at 1.0, 2.5, 5.0, 10.0, and 25.0 ms after initial impact of the bullet and vest.

In contrast, the T7 vertebra, which has about the same elevation as the aim point on the sternum and was therefore selected for instrumentation in the Natick-AFIP-ATC tests, never attains an axial velocity as large as 1 m/s at the discrete times captured in these figures. However, vertebrae other than T4 do attain a velocity as large as 1 m/s—T10 at 250 μs and T9 and T11 at 350 μs (Figure 34).

An axial velocity of at least 1 m/s in the direction of the bullet's initial velocity has been attained by much of the heart's anterior wall at 500 μs (Figure 35) and by most of the heart's anterior, posterior, and internal walls at 2.5 ms (Figure 36).

# 8. Computational Acceleration Results Compared With Experiment

Computational results for axial acceleration were obtained at the four locations from which experimental data are reported in Mackiewicz et al. (to be published). These are the lowest quarter of the posterior sternum, the anterior surface of the carina of the trachea, the ligamentum arteriosum, and the spinous process of the T7 vertebra.

Each experimental signal was sampled at a time interval of either 10 or 40 μs depending on the gauge (see Table 10). However, in each instance the frequency response of the gauge caused additional low-pass filtering of the experimental signal. Hence, the computational solution was sampled at a time interval of either 20, 250, 330, or 1300 μs, depending upon the frequency response of the gauge from which data were compared. Throughout the history plots in sections 8.2–8.5, axial accelerations are negative if in the same direction as the bullet's initial velocity vector (the same sign convention adopted in the contour plots of section 7).

## 8.1 Sternum Axial Acceleration

The mesh of the Sternum in WSTM99 is viewed from a posterior location in Figure 47. The mesh consists of 28 8-node hexagonal elements. In order to best track axial acceleration of the lower sternum, the lowest four elements were removed to form a new distinct part (shown in red in Figure 47). This part shares common nodes with adjacent elements of the remaining Sternum, so that no relative motion is possible. Axial acceleration of the center of mass of this new part is smoother in time than axial acceleration of a finite element node on the posterior side of Sternum. This smoothing is a consequence of spatial averaging and is believed to produce a more accurate result. The lumping of mass into discrete nodes tends to cause unrealistic spikes in response, which this spatial averaging corrects.

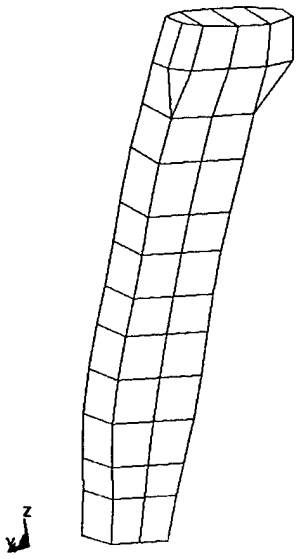


Figure 47. Mesh of Sternum; the lowest four elements are grouped into a separate part to track axial acceleration of the lowermost quarter of the sternum.

Figure 48 displays the computational signal for sternal axial acceleration sampled at 10-μs intervals. In Figures 49 and 50, the computational signal for sternal axial acceleration has been sampled at intervals of 20 and 250 μs, respectively, and compared with experimental signals from tests 637 and 678, respectively. In these tests Endevco models 7270A-20K and 7264A-2000, respectively, were employed (Table 10). The period corresponding to the top of the gauge's frequency range (Table 11) is equal to the sampling rate applied to the computational signal. Peak values for the computational and experimental signals in each of Figures 49 and 50 are collected in Table 16.

In Figure 49, the computational signal shows a larger (in absolute value) peak negative acceleration (in the direction of the bullet's initial path) by about a factor of 6, but the peak positive accelerations (recoil) in computation and experiment are in close agreement. The general shapes of the computational and experimental signals display close agreement after the initial 300 μs, but the computational signal displays larger oscillations at a frequency of roughly 10 kHz. There are two possible general explanations for the presence of these oscillations in the computational signal but not in the experimental signal. One is that they are physically meaningful and are not present in the experimental signal because of one of the unresolved issues raised in section 6. These issues include (3) possible filtering imposed by the electronics peripheral to the gauge, (4) possible slippage of the gauge relative to the sternum, and (5) impedance mismatch between the gauge and the surrounding medium. The second possible general explanation is that the oscillations were spuriously introduced into the

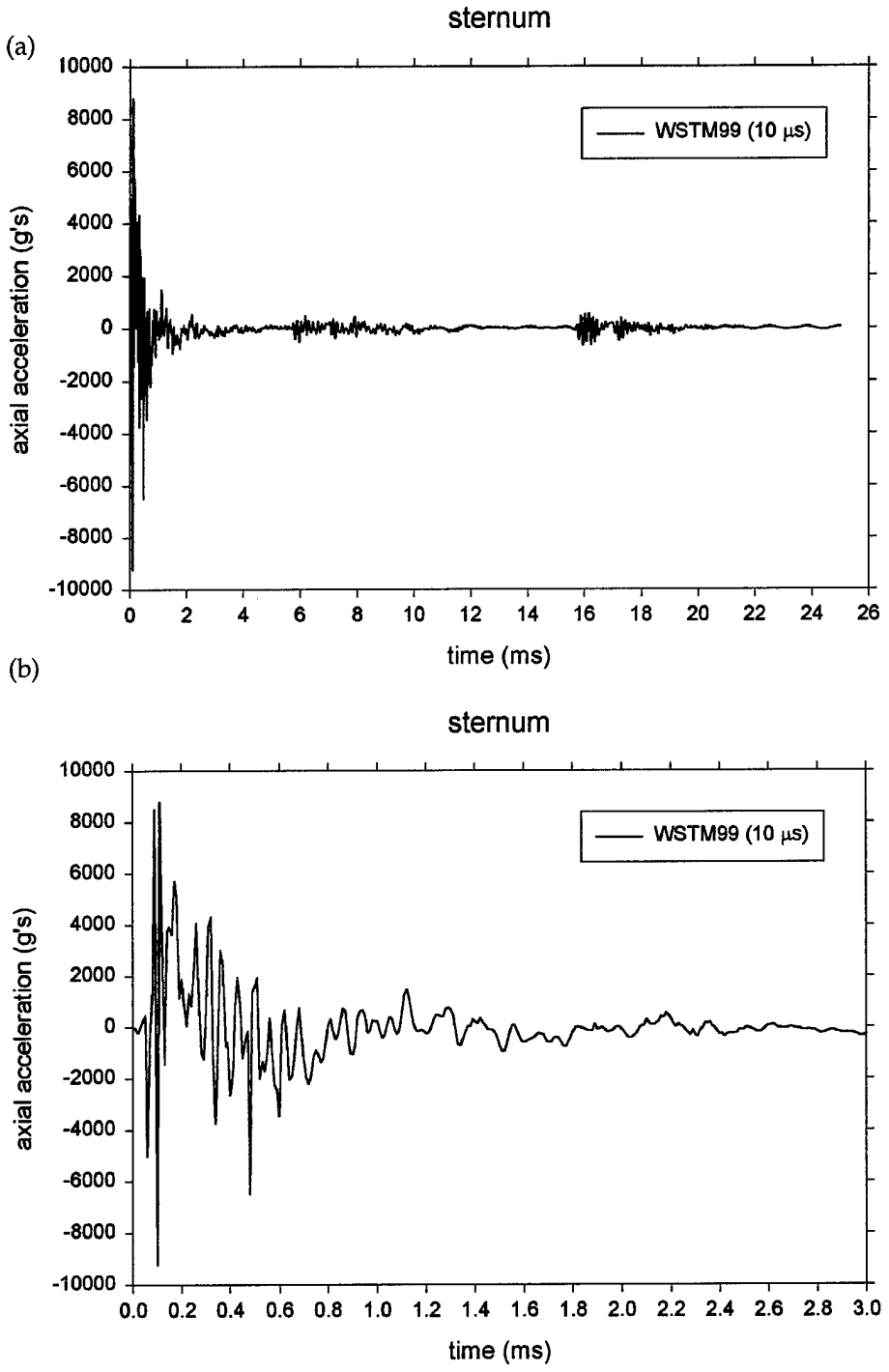


Figure 48. Computational results from WSTM99 for axial acceleration of the posterior sternum vs. time sampled at 10-μs intervals; (a) time from 0 to 25 ms and (b) time from 0 to 3 ms.

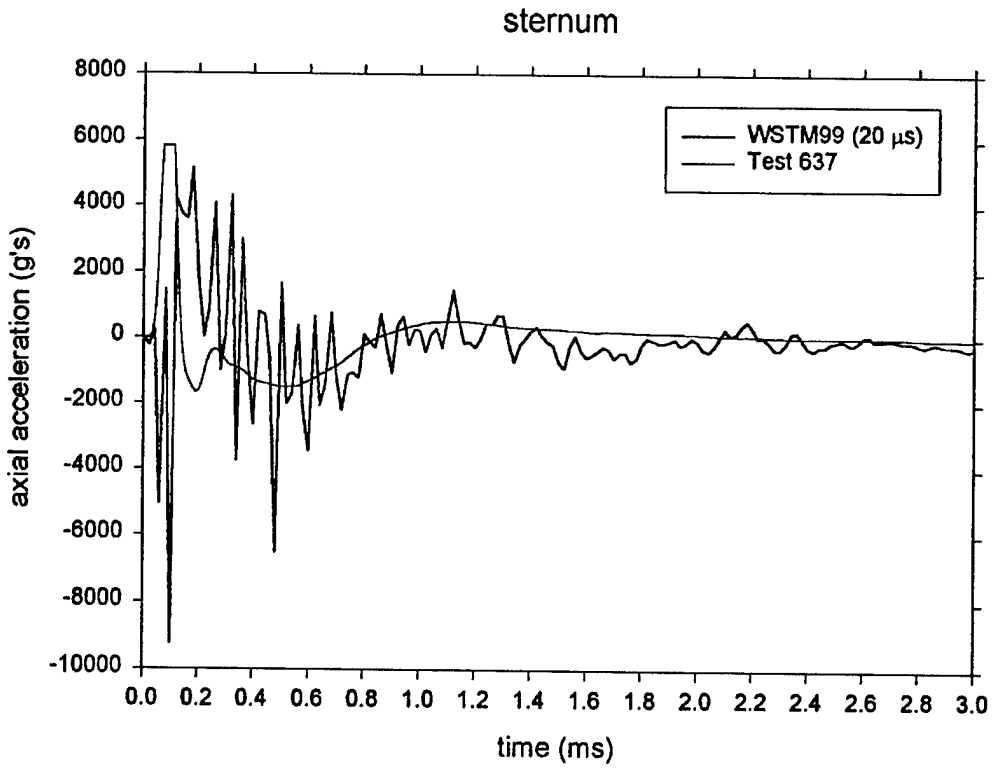


Figure 49. Computational results sampled at 20-μs intervals and compared with test 637 data for the axial acceleration of the lowest quarter of the posterior sternum vs. time after initial impact.

computational signal by the discretization into a spatially coarse FE mesh or by one of the other WSTM99 modeling issues that were raised in section 3.

In Figure 50, there is an initial negative peak in the computational signal that is not present in the experimental signal. Subsequently, the computational and experimental signals display good agreement in terms of peak accelerations in both negative and positive directions (Table 16), but the computational signal again shows larger oscillations.

## 8.2 Trachea Axial Acceleration

In the three tests, an accelerometer was sutured to the anterior surface of the carina (bifurcation point) of the trachea (De Maio 2001). The WSTM99 mesh of Trachea is shown in Figure 51. The trachea is composed of 212 4-node shell elements. Three of these elements, drawn in red, were separated to form a new part that shares common nodes with the remaining trachea. The purpose is to more accurately track axial acceleration of the carina, identified with the center of mass motion of this new part.

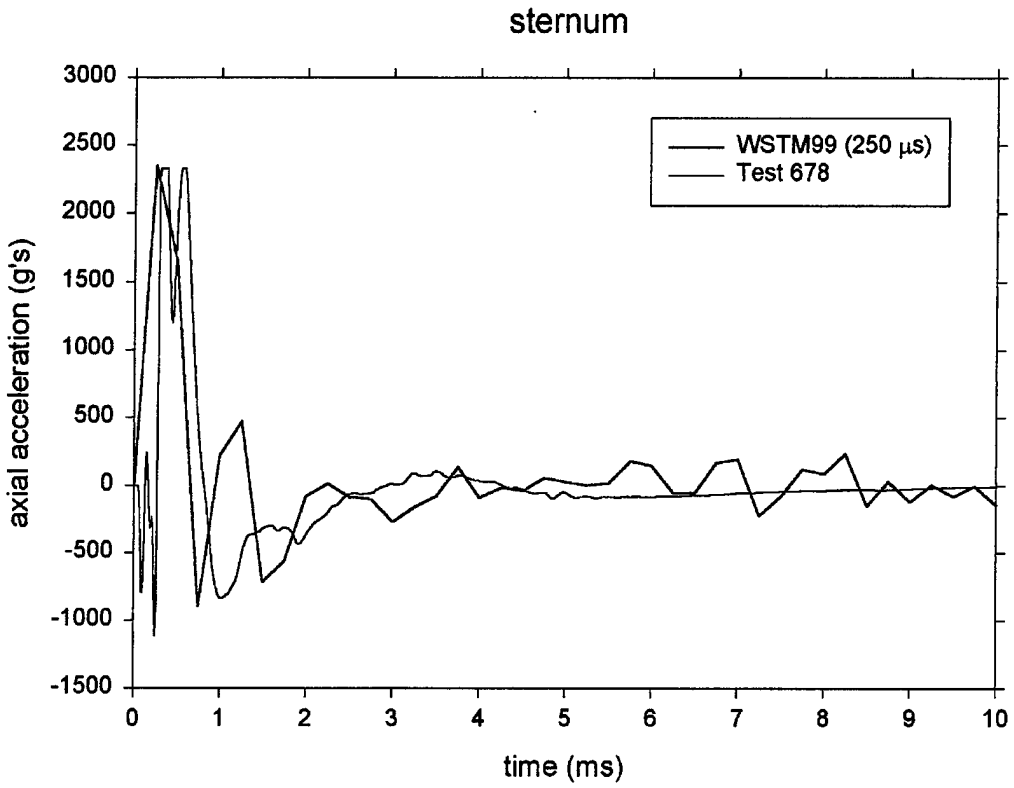


Figure 50. Computational results sampled at 250-μs intervals and compared with test 678 data for the axial acceleration of the lowest quarter of the posterior sternum versus time after initial impact.

Table 16. Computational peak axial acceleration of the lowest quarter of the posterior sternum as a function of sampling interval compared with experiment.

| Computation/Test No. | Peak Acceleration (g's) |
|---|---|
| WSTM99 (10 μs) | -9228<br>+8801 |
| WSTM99 (20 μs) | -9228<br>+5150 |
| Test 637 | -1651<br>+5809 |
| WSTM99 (250 μs) | -893<br>+2348 |
| Test 678 | -1107<br>+2325 |

Notes: The sampling interval applied to the computational signal is indicated in parentheses. Color coded to Figures 48–50.

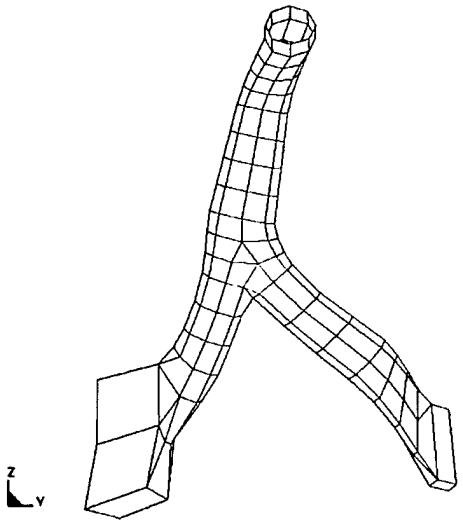

Figure 51. Mesh of Trachea; three elements are grouped into a separate part to track axial acceleration of the carina.

The computational result for tracheal acceleration sampled at 10-μs intervals is displayed in Figure 52. Endevco gauges 7265A was used in each of tests 524, 678, and 637 (see Table 10). Accordingly, the computational signal was sampled at 1300-μs intervals and compared with experimental signals in Figure 53 and Table 17.

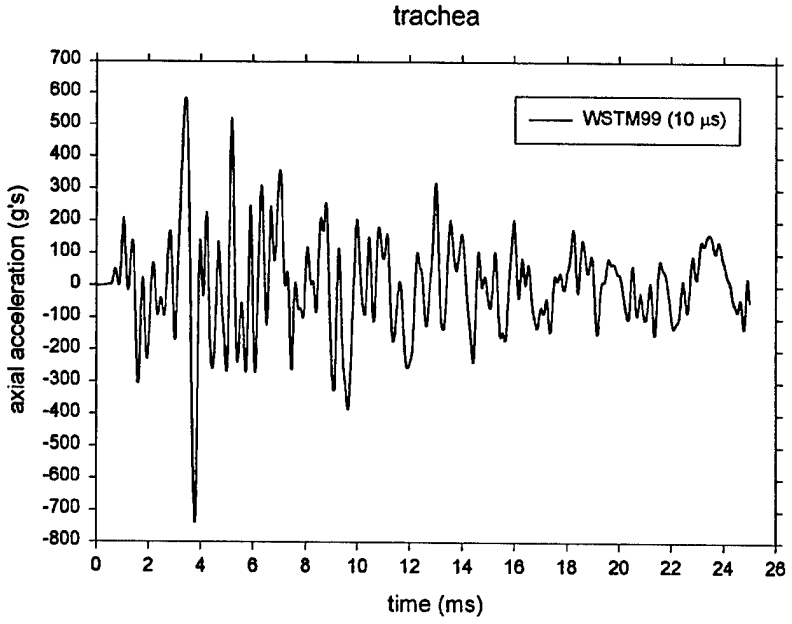


Figure 52. Computational results from WSTM99 for axial acceleration of the carina of the trachea vs. time sampled at 10-μs intervals.

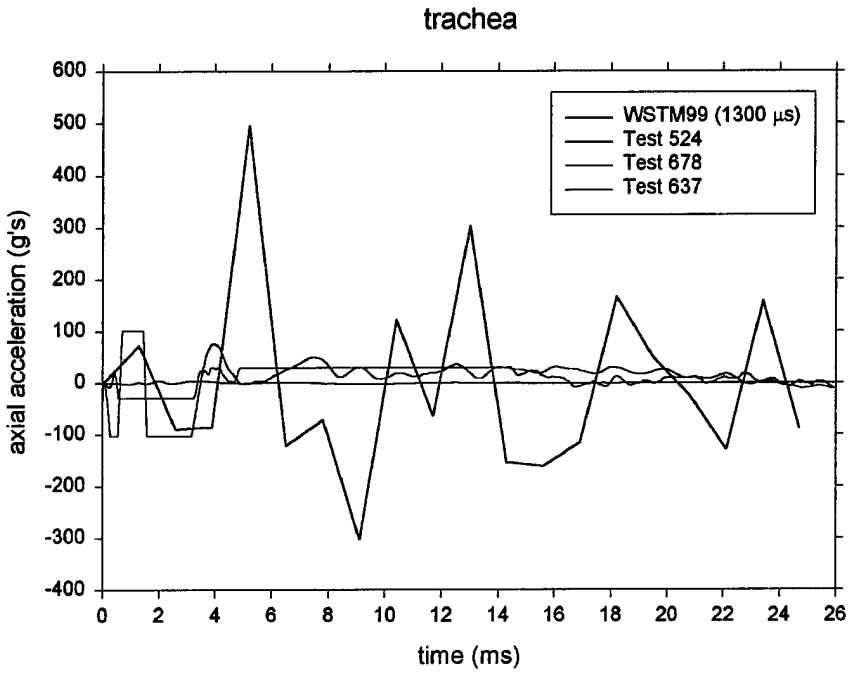


Figure 53. Computational results sampled at 1300-μs intervals and compared with data from tests 524, 678, and 637 for the axial acceleration of the carina of the trachea vs. time after initial impact.

Table 17. Computational peak axial acceleration of the carina of the trachea as a function of sampling interval compared with experiment.

| Computation/Test No. | Peak Acceleration (g's) |
|---|---|
| WSTM99 (10 μs) | -737<br>+583 |
| WSTM99 (1300 μs) | -302<br>+494 |
| Test 524 | -2<br>+5 |
| Test 678 | -29<br>+29 |
| Test 637 | -103<br>+102 |

Notes: The sampling interval applied to the computational signal is indicated in parentheses. Color coded to Figure 53.

The computational signal, when sampled at 1300-μs intervals, displays substantially larger peak axial accelerations in both directions than those observed in the three tests. As noted in subsection 6.3.2, the Endevco 7265A appears to have saturated in tests 678 and 637 and perhaps slipped in test 637. This gauge should not be used on the carina in future tests.

## 8.3 Ligamentum Arteriosum

In the tests, an accelerometer was sutured to the ligamentum arteriosum, near its connection with the aorta (De Maio 2001). Ligamentum Arteriosum in WSTM99 consists of four 4-node shell elements. The axial acceleration of the center of mass of all four elements is identified with that of ligamentum arteriosum and plotted in Figure 54 for a sampling interval of 10 μs.

In Figures 55 and 56, the computational signals sampled at 20- and 330-μs intervals, respectively, are compared with experimental signals from tests 678 and 637, respectively. Peak values are collected in Table 18.

The observation that peak computational acceleration exceeds peak experimental acceleration by an order of magnitude in Figure 56 can probably be attributed to amplitude and frequency saturation of the Endevco 7264B-500 gauge used in test 637. Recall the discussion in subsection 6.3.3 regarding inadequacies of this gauge.

This same observation in Figure 55 is more difficult to explain in the case of the Endevco 7270A-20K used in test 678. Adequacy of this gauge could not be ruled out in subsection 6.3.3. Perhaps slippage of the gauge is indicated, or the deficiencies in WSTM99 noted in section 3 may have produced a misleading computational result at the ligamentum arteriosum.

## 8.4 T7Axial Acceleration

In the tests, an accelerometer was sutured to the periosteum covering the spinous process of the T7 vertebra (De Maio 2001). In WSTM99, T7 is included in the part Thoracic Vertebrae, which is meshed with 8-node hexagonal elements. Two of these elements were separated to form a new part in order to smoothly track axial acceleration (Figure 57).

The computational signal sampled at 10-μs intervals is plotted in Figure 58. Endevco 7265A was used in all three tests (Table 10). The computational signal filtered at 1300-μs intervals is compared with experiment in Figure 59 and Table 19. The computational signal exceeds the gauge's 100-g's amplitude range, but the experimental signals peak at substantially less than 100 g's. In subsection 6.3.4, the experimental signals at T7 were judged to be suspect based on the gauge's inadequate frequency response. The discrepancies between computational and experimental T7 accelerations can perhaps be attributed to excessive filtering of the experimental signal by Endevco 7265A or to deficiencies

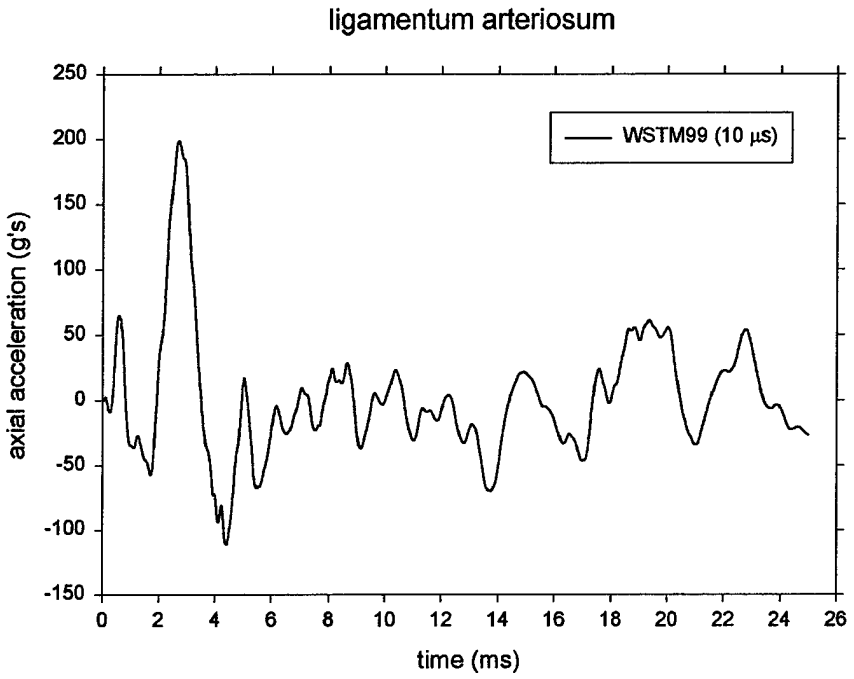


Figure 54. Computational results from WSTM99 for axial acceleration of the ligamentum arteriosum vs. time sampled at 10-μs intervals.

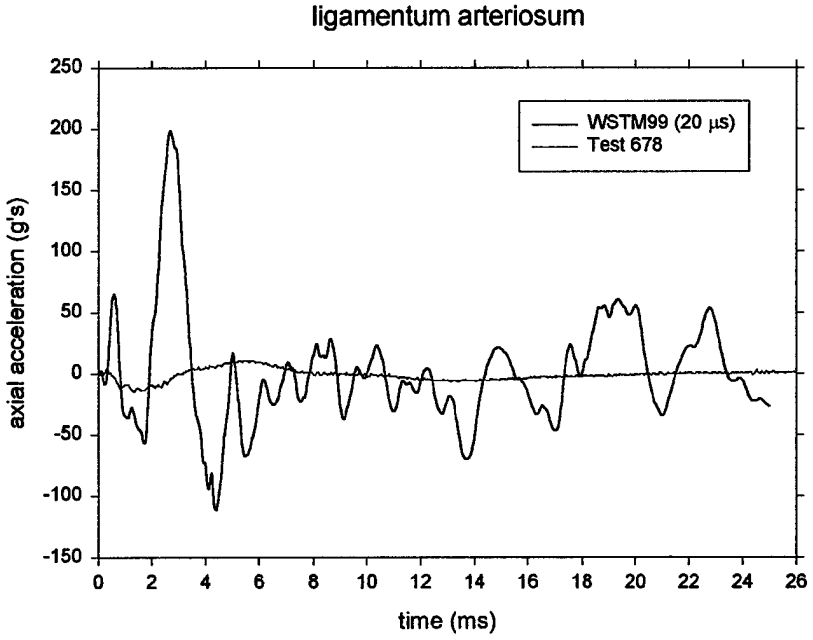


Figure 55. Computational results sampled at 20-μs intervals and compared with data from test 678 for the axial acceleration of the ligamentum arteriosum vs. time after initial impact.

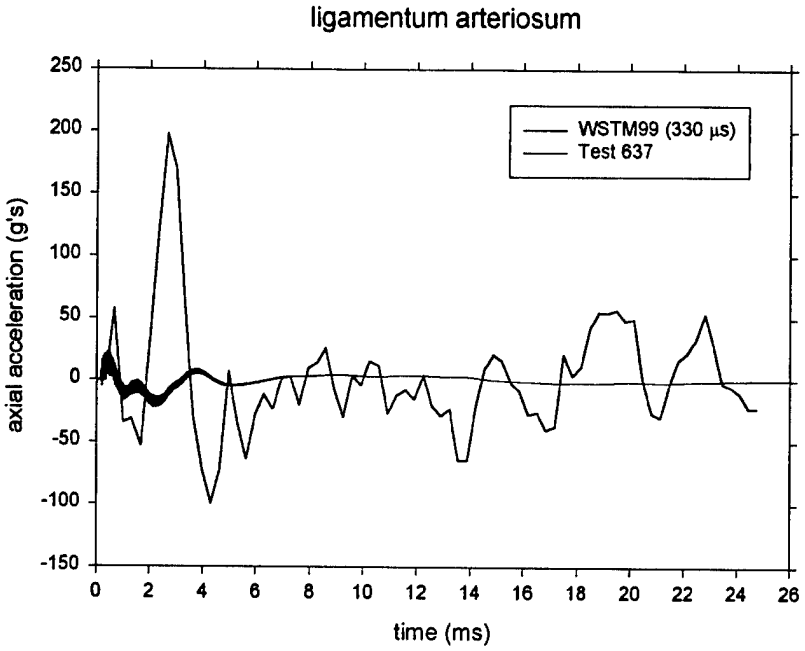


Figure 56. Computational results sampled at 330-μs intervals and compared with data from test 637 for the axial acceleration of the ligamentum arteriosum vs. time after initial impact.

Table 18. Computational peak axial acceleration of the ligamentum arteriosum compared with experiment.

| Computation/Test No. | Peak Acceleration (g's) |
|---|---|
| WSTM99 (10 μs) | -111<br>+199 |
| WSTM99 (20 μs) | -111<br>+199 |
| Test 678 | -14<br>+11 |
| WSTM99 (330 μs) | -99<br>+198 |
| Test 637 | -22<br>+23 |

Notes: The sampling interval applied to the computational signal is indicated in parentheses. Color coded to Figures 54–56.

(a)

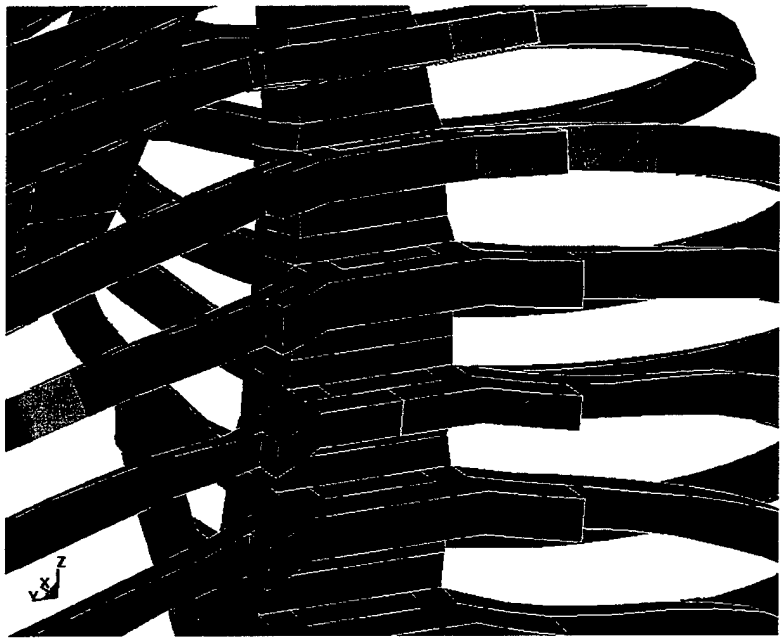

(b)

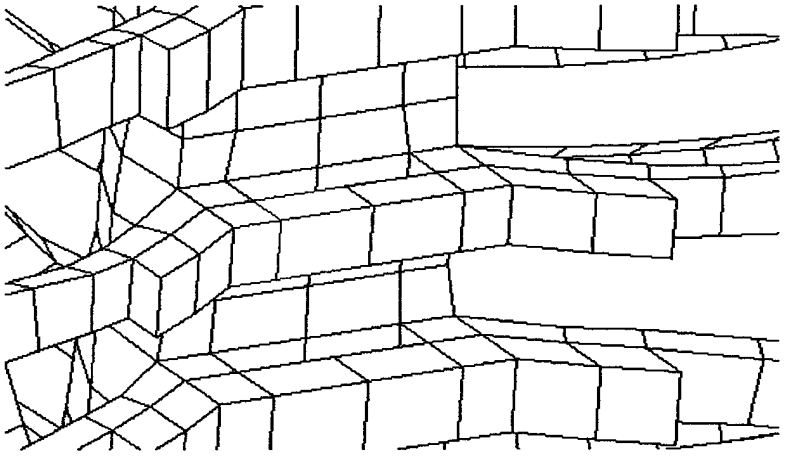

Figure 57. (a) Part and (b) mesh of the T7 vertebra; two elements are grouped into a separate part to track axial acceleration of the spinous process.

in WSTM99 noted in section 3. The WSTM99 representation of the ribs as composed entirely of elastic cortical bone is particularly relevant because the neglected damping provided by the cellular core of physical ribs might well lead to excessive spinal motion.

(a)

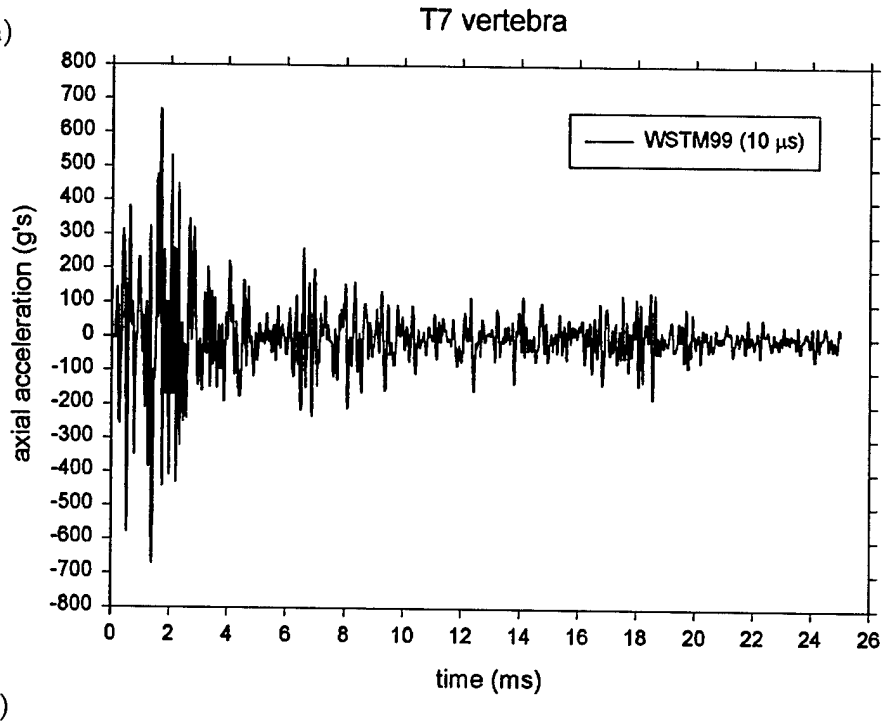


(b)

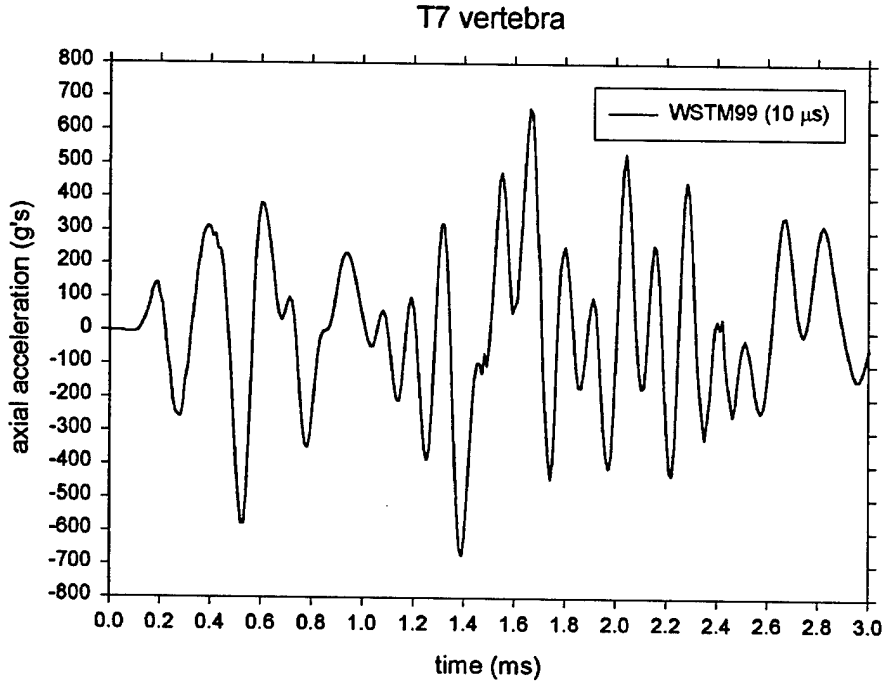


Figure 58. Computational results from WSTM99 for axial acceleration of the spinous process of T7 vertebra vs. time sampled at 10-μs intervals; (a) time from 0 to 25 ms and (b) time from 0 to 3 ms.

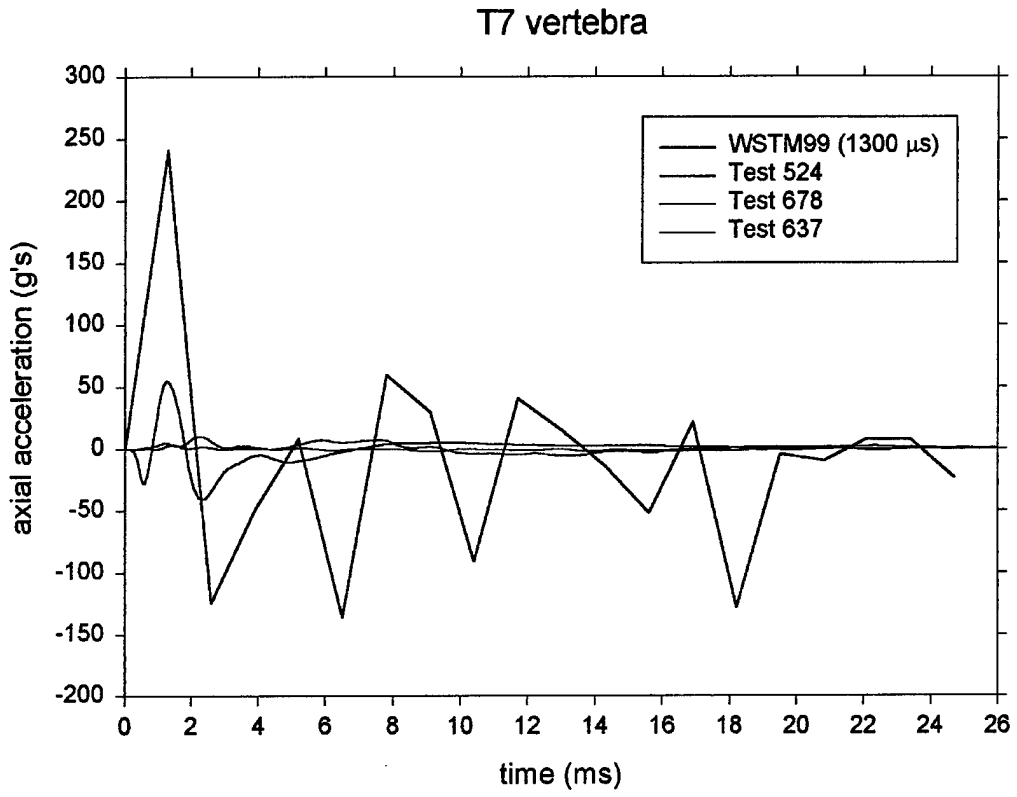


Figure 59. Computational results sampled at 1300 μs intervals and compared with data from tests 524, 678, and 637 for the axial acceleration of the spinous process of the T7 vertebra vs. time after initial impact.

Table 19. Computational peak axial acceleration of the spinous process of the T7 vertebra compared with experiment.

| Computational/Test No. | Peak Acceleration (g's) |
|---|---|
| WSTM99 (10 μs) | -670<br>+667 |
| WSTM99 (1300 μs) | -136<br>+241 |
| Test 524 | -40<br>+55 |
| Test 678 | -5<br>+7 |
| Test 637 | -2<br>+10 |

Notes: The sampling interval applied to the computational signal is indicated in parentheses. Color coded to Figures 58 and 59.

# 9. Concluding Remarks

## 9.1 Summary of Results

The 1999 version of the Wayne State Thorax Model, WSTM99, originally developed for automotive applications, was applied to the simulation of a 9-mm Remington bullet striking a multi-ply Kevlar vest worn by a human thorax. The bullet impact speed was 425.5 m/s, and the hit location was the vest material covering the center of the sternum. This simulated three tests performed on human thoracic tissue at the AFIP. In those tests, Endevco accelerometers were placed at four locations: the posterior sternum, the carina of the trachea, the ligamentum arteriosum, and the spinous process of the T7 vertebra.

Computational contour plots for axial (along the path of the bullet) velocity showed that larger peak velocities were attained at the T3 and T4 vertebrae than at the T7 vertebra that was instrumented in the tests. This phenomenon is presumably accounted for by the geometry of the ribs, the third and fourth ribs providing a relatively short path from the hit location to the spine.

Computational results for axial acceleration, when sampled at 10-μs intervals, displayed peak values of -9228 g's and +8801 g's at the posterior sternum, -737 g's and +583 g's at the carina of the trachea, -111 g's and +199 g's at the ligamentum arteriosum, and -670 g's and +667 g's at the back of the T7 vertebra. Here, the sign convention of positive in the direction of the bullet's initial path and negative in the opposite (recoil) direction has been used.

At the sternum and the ligamentum arteriosum, the computational axial acceleration was sampled at 20-μs intervals in order to compare with experimental data from the single test in which the Endevco 7270A-20K gauge was employed (test 637 in the case of the sternum and test 678 in the case of the ligamentum arteriosum). The other gauges employed were judged to be inadequate for the application. These were the Endevco 7265A at the trachea and the T7 vertebra, the Endevco 7264B-500 at the sternum and the ligamentum arteriosum, and the Endevco 7264A-2000 at the sternum.

At the sternum, the peak computational results when sampled at 20-μs intervals were -9228 g's and +5150 g's, as compared with -1650 g's and +5809 g's in the experiment with the Endevco 7270A-20K. At the ligamentum arteriosum, the peak computational results were -111 g's and +199 g's, as compared with -14 g's and +11 g's in the experiment with the Endevco 7270A-20K. Hence, peak axial acceleration was accurately predicted (to within 11%) at the sternum in the positive direction, but was overpredicted by a factor 5.6 at the sternum in the negative direction and by factors of 7.9 and 18.1 at the ligamentum arteriosum in the negative and positive directions, respectively. Furthermore, subsequent to

these peak values, the computational acceleration signals at both the sternum and the ligamentum arteriosum displayed oscillations of larger amplitude than were present in the corresponding experimental signal.

At both the sternum and the ligamentum arteriosum, if one assumes the experimental acceleration signal to be reliable, then the computational overprediction should be explained in terms of comments presented in sections 3, 4, and 5 for WSTM99, the vest model, and the bullet model, respectively. In the case of the sternal acceleration, attention should be focused on the bullet and vest modeling and on those WSTM99 issues raised in section 3 that pertain to the sternum itself and to the supporting costal cartilage and ribs (i.e., issue (4) in section 3.1, issues (1) and (2) in section 3.2, and issue (2) in section 3.3). In the case of the ligamentum arteriosum, it would be more difficult to pinpoint the most culpable features of WSTM99.

If, on the other hand, one chooses to attribute the discrepancies between computation and experiment to flaws in the data, then the experimental issues listed in section 6.2 should be used to account for small measured accelerations. Issue (4), possible slippage of the accelerometer, and issue (6), inertial loading by the accelerometer, would both lead to small measured values. Both of these issues are more likely applicable at the ligamentum arteriosum than at the sternum. Issue (3), additional filtering imposed by peripheral electronics, and issue (5), impedance mismatch between the gauge and the surrounding media, have not been ruled out at either location.

## 9.2 Plans for Future Work

Computational sources for the discrepancies between computed accelerations and the measurements include anatomical representations in WSTM99; meshing issues in WSTM99, the fabric, and the bullet; biomaterial representations in WSTM99; and fabric constitutive modeling. All of these issues are amenable to improvement.

The modest size of the WSTM99 mesh (15,671 nodes) allows for substantial refinements in mesh density. The meshing of ribs and costal cartilage should be replaced with elements that allow for the generation of bending stresses. In the case of bone, dynamic constitutive data exist (e.g., McElhaney [1966]), which can be utilized in refining the material model. For the softer biomaterials, a need exists for dynamic constitutive testing.

INTENTIONALLY LEFT BLANK.

# 10. References


Altair Engineering. HyperMesh Tutorials. Version 3.1, 2000.

Blethen, W. C. Personal communication. U.S. Army Aberdeen Test Center, Aberdeen Proving Ground, MD, 2001.

Chen, P. H. "Finite Element Dynamic Structural Model of the Human Thorax for Chest Impact Response and Injury Studies." *Aviation, Space, and Environmental Medicine*, vol. 49, pp. 143–149, 1978.

Cook, R. D., D. S. Malkus, and M. E. Plesha. *Concepts and Applications of Finite Element Analysis*. 3rd Edition, New York: Wiley, 1989.

De Maio, M. Personal communication. Armed Forces Institute of Pathology, Washington, DC, 2001.

De Maio, M., and S. A. Parks. Personal communication. Armed Forces Institute of Pathology, Washington, DC, 2001.

Dunn, F., and W. J. Fry. "Ultrasonic Absorption and Reflection by Lung Tissue." *Physics in Medicine and Biology*, vol. 5, pp. 401–410, 1961.

Endevco Corporation. <http://www.endevco.com>. 2001.

Granik, G., and I. Stein. "Human Ribs: Static Testing as a Promising Medical Application." *Journal of Biomechanics*, vol. 6, pp. 237–240, 1973.

Grosberg, P. "The Tensile Properties of Woven Fabrics." *Structural Mechanics of Fibers, Yarns, and Fabrics*, vol. 1, edited by J. W. S. Hearle, P. Grosberg, and S. Backer, New York: Wiley-Interscience, pp. 339–354, 1969.

Hearle, J. W. S. "Shear and Drape of Fabrics." *Structural Mechanics of Fibers, Yarns, and Fabrics*, vol. 1, edited by J. W. S. Hearle, P. Grosberg, and S. Backer, New York: Wiley-Interscience, pp. 371–410, 1969.

Irons, B. M. "Quadrature Rules for Brick Based Finite Elements." *International Journal of Numerical Methods in Engineering*, vol. 3, pp. 293–294, 1971.

Iwamoto, M., K. Miki, M. Mohammed, A. Nayef, K. H. Yang, P. C. Begeman, and A. I. King. "Development of a Finite Element Model of the Human Shoulder." *Stapp Car Crash Journal*, vol. 44, pp. 281–297, 2000.

Johnson, G. R. Personal communication. Alliant Techsystems, Hopkins, MN, 1999.

Johnson, G. R., S. R. Beissel, and P. M. Cunniff. "A Computational Model for Fabrics Subjected to Ballistic Impact." *18th International Symposium on Ballistics*, vol. 2, edited by W. G. Reinecke, Technomic Publishing, Lancaster, PA, pp. 962-969, 1999.

Jolly, J. E., and Y. W. Kwon. "Computer Modeling and Simulation of Bullet Impact to the Human Thorax." NPS-ME-00-002, Naval Postgraduate School, Monterey, CA, June 2000.

Kohn, B. J. "Compilation of Hugoniot Equations of State." AFWL-TR-69-38, Air Force Weapons Laboratory, Kirtland Air Force Base, NM, p. 81, April 1969.

Kolsky, H. *Stress Waves in Solids*. New York: Dover, 1963.

Lee, J. B., and K. H. Yang. "Development of a Finite Element Model of the Human Abdomen." *Stapp Car Crash Journal*, vol. 45, pp. 79-100, 2001.

Livermore Software Technology Corporation. LS-DYNA Keyword User's Manual, Nonlinear Dynamic Analysis of Structures. Version 950, Livermore, CA, 1999.

Mackiewicz, J., W. Blethen, T. Carlson, J. J. Prifti, M. De Maio, S. Parks, P. Schilke, S. Campman, C. Meyers, J. Georgia, and D. Flemming. "Effects of Ballistically Induced Blunt Trauma and Correlations to Laboratory Measurement Techniques." ATC-8444, U.S. Army Aberdeen Test Center, Aberdeen Proving Ground, MD, 2002.

Marieb, E. N. *Human Anatomy and Physiology*. 5th Edition, San Francisco: Benjamin Cummings, 2001.

Masiello, P. J. "A Finite Element Model for Analysis of Thoracic Injury." Technical Report J97-2997-05/024R1, JAYCOR Corporation, San Diego, CA, August 1997.

McElhaney, J. H. "Dynamic Response of Bone and Muscle Tissue." *Journal of Applied Physiology*, vol. 21, pp. 1231-1236, 1966.

Moore, K. L., and A. F. Dalley. *Clinically Oriented Anatomy*. Fourth Edition, Baltimore, MD: Lippincott Williams & Wilkens, 1999.

Parks, CDR S. A. (USNMC). Personal communication. Armed Forces Institute of Pathology, Washington, DC, February 2001.

Pawsey, S. F., and R. W. Clough. "Improved Numerical Integration of Thick Shell Finite Elements." *International Journal for Numerical Methods in Engineering*, vol. 3, pp. 575-586, 1971.

Plank, G. R., and R. H. Eppinger. "An Improved Finite Element Model of the Human Thorax." *Proceedings of the 13th International Technical Conference on Experimental Safety Vehicles*, pp. 902-907, November 1991.

Raftenberg, M. N., and T. J. Mulkern. "Quasi-Static, Uniaxial Tension Characteristics of Plain-Woven Kevlar KM2." U.S. Army Research Laboratory, Aberdeen Proving Ground, MD, to be published.

Roberts, S. B., and P. H. Chen. "Elastostatic Analysis of the Human Thoracic Skeleton." *Journal of Biomechanics*, vol. 3, pp. 527–545, 1970.

Shah, C., K. H. Yang, W. N. Hardy, H. K. Wang, and A. I. King. "Development of a Computer Model to Predict Aortic Rupture Due to Impact Loading." *Stapp Car Crash Journal*, vol. 45, pp. 161–182, 2001.

Shim, V. P. W., C. T. Lim, and K. J. Foo. "Dynamic Mechanical Properties of Fabric Armour." *International Journal of Impact Engineering*, vol. 25, pp. 1–15, 2001.

Snell, R. S. *Clinical Anatomy for Medical Students*. 6th Edition, Philadelphia, PA: Lippincott Williams & Wilkins, 2000.

Spitzer, V. M., and D. G. Whitlock. *Atlas of the Visible Human Male*. Sudbury, MA: Jones and Bartlett, 1998.

Sundaram, S. H., and C. C. Feng. "Finite Element Analysis of the Human Thorax." *Journal of Biomechanics*, vol. 10, pp. 505–516, 1977.

Tortora, G. J., and S. R. Grabowski. *Principles of Anatomy and Physiology*. 9th Edition, New York: Wiley, 2000.

Vawter, D. L., Y. C. Fung, and J. B. West. "Constitutive Equation of Lung Tissue Elasticity." *Journal of Biomechanical Engineering*, vol. 101, no. 1, pp. 38–45, February 1979.

Wang, K. H.-C. "Development of a Side Impact Finite Element Human Thoracic Model." Ph.D. dissertation, Wayne State University, Detroit, MI, 1995.

Warner, S. B. *Fiber Science*. Englewood Cliffs, NJ: Prentice Hall, 1995.

Yamada, H. *Strength of Biological Materials*. Baltimore, MD: Williams & Wilkins Co., 1970.

Yang, K. H. Personal communication. Wayne State University, Detroit, MI, 2002.

INTENTIONALLY LEFT BLANK.

## List of Symbols

| | |
|---|---|
| $A$ | beam element cross-sectional area |
| $A_{shear}$ | beam element shear area |
| $c_L$ | speed of longitudinal or irrotational waves in an isotropic elastic medium |
| $c_T$ | speed of transverse or equivoluminal waves in an isotropic elastic medium |
| $E$ | Young's modulus of elasticity |
| $E_i$ | average Young's modulus based on the nonlinear "toe" region ($0 \leq \varepsilon < \varepsilon_i$) of a constant-strain-rate stress-strain curve in uniaxial tension |
| $E_f$ | Young's modulus based on the linear region of a constant-strain-rate stress-strain curve in uniaxial tension |
| $G$ | elastic shear modulus |
| $I_{rr}, I_{ss}, I_{tt}$ | beam element's moments of inertia |
| $h$ | shell element thickness |
| $t$ | time, with zero time corresponding to initial impact of the vest and bullet |
| $\varepsilon$ | strain |
| $\varepsilon_i$ | strain at the boundary between the initial "toe" region and the subsequent linear region on a constant-strain-rate stress-strain curve in uniaxial tension |
| $\varepsilon_u$ | strain at ultimate stress on a constant-strain-rate stress-strain curve in uniaxial tension |
| $\nu$ | Poisson's ratio |

$\rho$ current density

$\rho_0$ initial density

$\sigma_u$ ultimate stress on a constant-strain-rate stress-strain curve in uniaxial tension

# Report Documentation Page

*Form Approved*
*OMB No. 0704-0188*



| 1. REPORT DATE *(DD-MM-YYYY)* | 2. REPORT TYPE | 3. DATES COVERED (From - To) |
|---|---|---|
| January 2003 | Final | 1 October 2000–30 September 2001 |

**4. TITLE AND SUBTITLE**
Response of the Wayne State Thorax Model With Fabric Vest to a 9-mm Bullet

**5a. CONTRACT NUMBER**

**5b. GRANT NUMBER**

**5c. PROGRAM ELEMENT NUMBER**

**6. AUTHOR(S)**
Martin N. Raftenberg

**5d. PROJECT NUMBER**
1L162618AH80

**5e. TASK NUMBER**

**5f. WORK UNIT NUMBER**

**7. PERFORMING ORGANIZATION NAME(S) AND ADDRESS(ES)**
U.S. Army Research Laboratory
ATTN: AMSRL-WM-TD
Aberdeen Proving Ground, MD 21005-5066

**8. PERFORMING ORGANIZATION REPORT NUMBER**
ARL-TR-2897

**9. SPONSORING/MONITORING AGENCY NAME(S) AND ADDRESS(ES)**

**10. SPONSOR/MONITOR'S ACRONYM(S)**

**11. SPONSOR/MONITOR'S REPORT NUMBER(S)**

**12. DISTRIBUTION/AVAILABILITY STATEMENT**
Approved for public release; distribution is unlimited.

**13. SUPPLEMENTARY NOTES**

**14. ABSTRACT**

The 1999 version of the Wayne State Thorax Model, WSTM99, was applied to the finite element (FE) simulation of a 9-mm Remington bullet striking a multi-ply Kevlar (DuPont) vest worn by a human thorax. The bullet impact speed was 425.5 m/s, and the hit location was the vest material covering the center of the sternum. FE models for the vest and bullet were developed. The computations were performed with the LS-DYNA FE code. Computational results for axial (along the path of the bullet) acceleration were compared with accelerometer measurements from three tests performed at the Armed Forces Institute of Pathology on human thoracic tissue. At the posterior sternum, the computed peak axial acceleration was 5.6 times larger than the measured value in the direction of the bullet's lateral path and 11% smaller than the measured value in the opposite (recoil) direction. At the ligamentum arteriosum, the computed peak axial acceleration exceeded the measured value by factors of 7.9 and 18.1 in the directions along and opposite to the bullet's initial path, respectively. Possible explanations for the discrepancies are offered in terms of features of WSTM99 and of the gauges used in the tests.

**15. SUBJECT TERMS**
human thorax model, body armor, personal protection, Kevlar, KM2, vest, mechanical properties, constitutive properties

| 16. SECURITY CLASSIFICATION OF: | | | 17. LIMITATION OF ABSTRACT | 18. NUMBER OF PAGES | 19a. NAME OF RESPONSIBLE PERSON |
|---|---|---|---|---|---|
| a. REPORT | b. ABSTRACT | c. THIS PAGE | | | Martin N. Raftenberg |
| UNCLASSIFIED | UNCLASSIFIED | UNCLASSIFIED | UL | 89 | 19b. TELEPHONE NUMBER *(Include area code)* (410) 306-0949 |

**Standard Form 298 (Rev. 8/98)**
**Prescribed by ANSI Std. Z39.18**

INTENTIONALLY LEFT BLANK.